

MODELING AND EXPERIMENTAL IDENTIFICATION OF QUADROTOR
AERODYNAMICS

A THESIS SUBMITTED TO
THE GRADUATE SCHOOL OF NATURAL AND APPLIED SCIENCES
OF
MIDDLE EAST TECHNICAL UNIVERSITY

BY

D. DERYA KAYA

IN PARTIAL FULFILLMENT OF THE REQUIREMENTS
FOR
THE DEGREE MASTER OF SCIENCE
IN
AEROSPACE ENGINEERING

AUGUST 2014

Approval of the thesis:

**MODELING AND EXPERIMENTAL IDENTIFICATION OF QUADROTOR
AERODYNAMICS**

submitted by **D. DERYA KAYA** in partial fulfillment of the requirements for the degree of **Master of Science in Aerospace Engineering Department, Middle East Technical University** by,

Prof. Dr. Canan Özgen
Dean, Graduate School of **Natural and Applied Sciences**

Prof. Dr. Ozan Tekinalp
Head of Department, **Aerospace Engineering**

Asst. Dr. Ali Türker Kutay
Supervisor, **Aerospace Engineering Dept., METU**

Examining Committee Members:

Prof. Dr. Ozan Tekinalp
Aerospace Engineering Dept., METU

Asst. Prof. Dr. Ali Türker Kutay
Aerospace Engineering Dept., METU

Prof. Dr. Kemal Leblebicioğlu
Department of Electrical and Electronics Engineering

Assoc. Prof. Dr. İlkay Yavrucuk
Aerospace Engineering Dept., METU

Asst. Prof. Dr. Ercan Gürses
Aerospace Engineering Dept., METU

Date:

I hereby declare that all information in this document has been obtained and presented in accordance with academic rules and ethical conduct. I also declare that, as required by these rules and conduct, I have fully cited and referenced all material and results that are not original to this work.

Name, Last Name: D. Derya KAYA

Signature :

ABSTRACT

MODELING AND EXPERIMENTAL IDENTIFICATION OF QUADROTOR AERODYNAMICS

Kaya, D. Derya

M.Sc., Department of Aerospace Engineering

Supervisor: Asst. Prof. Dr. Ali Türker Kutay

August 2014, 127 pages

The aim of this study is to obtain mathematical models for aerodynamic forces and moments of rotors of a quadrotor helicopter, and estimate their parameters through wind tunnel tests for hover, vertical climb, and forward flight conditions. The main factors which determine the movement of a quadrotor UAV are the aerodynamic forces and moments in three axes created by four rotors of the vehicle. Hence, accurate calculation of rotor forces and moments in varying flight conditions are essential to establish a precise simulation of the vehicle. For this purpose, analytical models for aerodynamic forces and moments of a rotor are derived using blade element and momentum theories. These models predict the aerodynamic rotor forces and moments generated by air flows around the blades due to blade rotation and vehicle motion on all three axes. Parameters of the mathematical models are then identified through experimental force and moment measurements obtained in a wind tunnel at various rotor speed, free stream velocity, and vehicle angle of attack values. Since the analytical model cannot capture certain experimentally observed dependencies, an empirical rotor model has been developed by surface fitting a second order polynomial model to test data. The developed model allows us to

accurately predict aerodynamic loads on a quadrotor in various rotor speeds and flight conditions.

Keywords: Quadrotor UAV, Modeling, Parameter Estimation, System Identification, Rotor Aerodynamics

ÖZ

DÖRT ROTORLU ARACIN AERODİNAMİĞİNİN MODELLENMESİ VE DENEYSEL TANIMLANMASI

Kaya, D. Derya

Yüksek Lisans, Havacılık ve Uzay Mühendisliği Bölümü

Tez Yöneticisi: Yrd. Doç. Dr. Ali Türker Kutay

Ağustos 2014, 127 sayfa

Bu çalışmanın amacı dört rotorlu bir helikopterin pervanelerinde oluşan aerodinamik kuvvet ve momentleri veren matematiksel modeller elde etmek ve bu modellerin parametrelerini askıda kalma, tırmanış ve ileri uçuş koşulları için rüzgar tüneli testleri ile belirlemektir. Dört rotorlu insansız hava aracının hareketini belirleyen temel etkenler aracın pervaneleri tarafından oluşturulan, üç eksenlerdeki kuvvet ve momentlerdir. Dolayısıyla, pervane üzerindeki kuvvet ve momentlerin hassas olarak hesaplanması doğru bir benzetim modelinin oluşturulması için önemlidir. Bu amaçla, pervane kuvvet ve momentleri için pala elemanları ve momentum teorileri ile elde edilmiş analitik modeller kullanılmıştır. Bu modeller pala üzerinde pala dönüşü ve araç hareketi sebebiyle oluşan aerodinamik akış sonucu üç ekseninde oluşan kuvvet ve momentleri tahmin etmektedir. Bu modellerdeki parametreler daha sonra rüzgar tüneline farklı pervane hızı, araç hızı ve hücum açısı değerlerinde elde edilen kuvvet ve moment ölçümleri kullanılarak tanımlanmıştır. Analitik model, deneysel olarak gözlemlenmiş bazı bağımlılıkları yakalayamadığı için, ikinci derece bir polinom modeli olan yüzey fitting geliştirilmiştir. Geliştirilen model, farklı pervane hızı ve uçuş koşullarında dört rotorlu aracın üzerindeki aerodinamik kuvvetlerin hassas olarak tahmin edilebilmesini sağlamaktadır.

Anahtar Kelimeler: Dört Rotorlu İnsansız Hava Aracı, Modelleme, Parametre Tahmini, Sistem Tanımlaması, Pervane Aerodinamiği

ACKNOWLEDGMENTS

I would like to express my deepest gratitude to my thesis supervisor, Asst. Prof. Dr. Ali Türker Kutay for his encouragement, advice, criticism, and valuable discussion throughout my research. Without his guidance and support, I would not be able to complete this work. I am very grateful for his time and collaboration. It was a great honor to work with him.

My special thanks to my parents for their never ending love and support, and for all sacrifices they have made for me. I'd like to let my dearest brother Deniz know that I am aware of how lucky I am for having him and I am very grateful to each and every one of my family.

I would also like to thank my friends Merve and Ayşe for their endless friendship throughout my life.

I want to emphasize my special thanks to Harun for his designs of experimental setup and endless help, and I appreciate the never wavering support and guidance of Anas during the experiments.

I'd like to thank my colleague Emre for his support and collaboration since the moment I have shared the same supervisor with him.

I would also like to thank Melika for her guidance of using the wind tunnel.

I would also want to thank Assoc. Prof. Dr. Demirkan Çöker and Zeynep Çakır for their advices during my first semester at the department.

Special thanks to RÜZGEM for the contribution of experimental set-up.

TABLE OF CONTENTS

ABSTRACT	v
ÖZ	vii
ACKNOWLEDGMENTS	ix
TABLE OF CONTENTS	xi
LIST OF TABLES	xiii
LIST OF FIGURES	xv
LIST OF SYMBOLS	xxi
LIST OF ABBREVIATIONS	xxv
CHAPTER 1	1
INTRODUCTION	1
1.1. Motivation and Objective	1
1.2. Literature Review	2
1.3. History	4
1.3.1. Manned Quadrotor Studies	4
1.3.2. Unmanned Quadrotor Studies	7
1.4. Quadrotor Preliminaries	9
1.4.1. Working Principle	9
1.4.2. Advantages and Drawbacks	12
1.4.3. Applications	13
1.5. Contribution of the Thesis	13
1.6. Structure of the Thesis	14
CHAPTER 2	15
ROTOR AERODYNAMICS	15
2.1. Momentum Theory	15
2.1.1. Momentum Theory in Hovering Flight	15
2.1.2. Momentum Theory in Vertical Climb and Vertical Descent Flights	18

2.1.3. Momentum Theory in Forward Flight.....	19
2.2. Blade Element Theory	22
CHAPTER 3.....	41
PARAMETER ESTIMATION AND SYSTEM IDENTIFICATION.....	41
3.1. Experiments	41
3.2. Parameter Estimation Method Used in the Study	44
3.2.1. Simple Linear Regression.....	44
3.2.2. Multiple Linear Regression	46
3.2.3. The Coefficient of Determination.....	49
CHAPTER 4.....	53
RESULTS.....	53
4.1. Results by using Blade Element Theory and Method of Least Squares ..	53
4.2. Results by using Surface Fitting	76
4.3. Rotor Interactions and Body Effect	114
CHAPTER 5.....	119
CONCLUSION	119
5.1. Conclusion	119
5.2. Discussion	120
5.3. Future Works	121
CHAPTER 6.....	123
APPENDIX	123
A. Properties of the Quadrotor and rotor used in the Study	123
REFERENCES.....	125

LIST OF TABLES

Table 1.1: Unmanned Quadrotor Studies at the Universities.....	7
Table 1.2: Advantages and Drawbacks of the Quadrotor	12
Table 1.3: Applications	13
Table 2.1: Induced velocity in different flight conditions.....	22
Table 2.2: Integrals used in blade element theory.....	24
Table 2.3: Forces and moments expressions according to blade element theory	38
Table 4.1: Experimental data and calculated induced velocity in hovering flight.....	53
Table 4.2: Fitted values in hovering flight	53
Table 4.3: Parameter estimation results ignoring induced velocity	54
Table 4.4: Parameter estimation results including induced velocity using BET	56
Table 4.5: Coefficient of determination in hovering flight using BET	59
Table 4.6: Experimental data and fitted values at 90 degree A.o.A.....	59
Table 4.7: Parameter estimation results for vertical climb using BET	60
Table 4.8: Coefficient of determination in vertical climb using BET.....	62
Table 4.9: Coefficients found experimentally using BET	64
Table 4.10: Coefficients found numerically using BET	65
Table 4.11: Coefficient of determination in forward flight by using BET	65
Table 4.12: Coefficients of thrust force at different angles of attack.....	77
Table 4.13: Coefficients of hub force at different angles of attack.....	91
Table 4.14: Coefficients of rotor torque at different angles of attack	100
Table 4.15: Coefficients of rolling moment at different angles of attack	108
Table 4.16: Goodness of fit in surface fitting	114
Table 4.17: Thrust produced by each rotor of the quadrotor running separately.....	115
Table 4.18: Thrust while two rotors are running	115
Table 4.19: Thrust while all rotors are running.....	116
Table 6.1: Constants of the quadrotor [18]	123
Table A.6.2: Properties of the quadrotor used in the study [18]	123

Table A.6.3: Properties of the rotor used in the experiments.....	124
---	-----

LIST OF FIGURES

Figure 1.1: Breguet-Richet Gyroplane No.1 [13]	4
Figure 1.2: Oemichen No.2 [14]	5
Figure 1.3: De Bothezat [15].....	5
Figure 1.4: Convertawings Model A [16]	6
Figure 1.5: Curtiss-WrightVZ-7 [17]	6
Figure 1.6: Body coordinate system of the quadrotor [18]	10
Figure 1.7: Throttle Control	10
Figure 1.8: Yaw Control	11
Figure 1.9: Roll Control	11
Figure 1.10: Pitch Control.....	12
Figure 2.1: Momentum theory in hovering flight	16
Figure 2.2: Momentum theory in vertical climb [19, 20]	19
Figure 2.3: Disc incidence and component velocities in forward flight [19].....	19
Figure 2.4: Momentum theory in forward flight.....	20
Figure 2.5: Forces and moments on a rotor [18].....	23
Figure 2.6: Blade element theory [19]	24
Figure 2.7: Directions of the velocities for a rotor [4]	25
Figure 2.8: Rotor disc view from above [19].....	25
Figure 3.1: Quadrotor UAV	41
Figure 3.2: Wind tunnel	41
Figure 3.3: Test setup.....	42
Figure 3.4: Velocity sensor	42
Figure 3.5: Load cell	43
Figure 3.6: <i>RPM</i> sensor.....	43
Figure 3.7: Data acquisition device.....	43
Figure 3.8: Deviations of the data from the estimated regression model [22]	45

Figure 4.1: Thrust change w.r.t. the angular velocity of the rotor using BET in hovering flight	55
Figure 4.2: Rotor torque change w.r.t. the angular velocity of the rotor using BET in hovering flight	55
Figure 4.3: Induced velocity w.r.t. angular velocity of rotor in hovering flight [24].	57
Figure 4.4: Thrust change w.r.t. the angular velocity of the rotor using BET in hovering flight	58
Figure 4.5: Rotor torque change w.r.t the angular velocity of the rotor using BET in hovering flight	58
Figure 4.6: Thrust and fitted thrust w.r.t. the free stream velocity at 5820 <i>RPM</i> using BET	61
Figure 4.7: Rotor torque and fitted rotor torque in vertical climb flight at 5820 <i>RPM</i> using BET	61
Figure 4.8: Change of thrust w.r.t. free stream velocity in vertical flight at different angular velocity of the rotor (<i>RPM</i>)	62
Figure 4.9: Test data and fitted model in different angular velocity of the rotor in vertical climb flight at different angular velocity of the rotor (<i>RPM</i>)	63
Figure 4.10: Change of induced velocity at different angular velocity of rotor	64
Figure 4.11: Test data and fitted thrust model w.r.t. angular velocity of rotor for different wind speeds at 0 degree A.o.A.	66
Figure 4.12: Test data and fitted thrust model w.r.t. angular velocity of rotor for different wind speeds at 30 degree A.o.A.	67
Figure 4.13: Test data and fitted thrust model w.r.t. angular velocity of rotor for different wind speeds at 45 degree A.o.A.	68
Figure 4.14: Test data and fitted thrust model w.r.t. angular velocity of rotor for different wind speeds at 60 degree A.o.A.	69
Figure 4.15: Test data and fitted thrust model w.r.t. free stream velocity for different rotor speeds at 30 degree A.o.A.	70
Figure 4.16: Test data and fitted thrust model w.r.t. free stream velocity for different rotor speeds at 45 degree A.o.A.	72

Figure 4.17: Test data and fitted model w.r.t. free stream velocity for different rotor speeds at 60 degree A.o.A.....	73
Figure 4.18: Induced velocity at different angular velocity of the rotor in forward flight	74
Figure 4.19: Test data and fitted rotor torque model using BET at 0 degree A.o.A. for different wind speeds	75
Figure 4.20: Test data and fitted hub force model using BET at 30 degree A.o.A. for different wind speeds	76
Figure 4.21: Surface fitting at 90 degree A.o.A. for thrust force	78
Figure 4.22: Surface fitting at 60 degree A.o.A. for thrust force	78
Figure 4.23: Surface fitting at 45 degree A.o.A. for thrust force	79
Figure 4.24: Surface fitting at 30 degree A.o.A. for thrust force	79
Figure 4.25: Surface fitting at 0 degree A.o.A. for thrust force.....	80
Figure 4.26: Test data and fitted thrust model at 0 degree A.o.A. w.r.t. the angular velocity of the rotor for different wind speeds.....	81
Figure 4.27: Test data and fitted thrust model at 30 degree A.o.A. w.r.t. the angular velocity of the rotor for different wind speeds.....	82
Figure 4.28: Test data and fitted thrust model at 45 degree A.o.A. w.r.t. the angular velocity of the rotor for different wind speeds.....	83
Figure 4.29: Test data and fitted thrust model at 60 degree A.o.A. w.r.t. the angular velocity of the rotor for different wind speeds.....	84
Figure 4.30: Test data and fitted thrust model at 30 degree A.o.A. w.r.t. free stream velocity for different rotor speeds	85
Figure 4.31: Test data and fitted thrust model at 45 degree A.o.A. w.r.t. free stream velocity for different rotor speeds	87
Figure 4.32: Test data and fitted thrust model at 60 degree A.o.A. w.r.t. free stream velocity for different rotor speeds	88
Figure 4.33: Test data and thrust model at 0 degree A.o.A. for different wind speeds	89

Figure 4.34: Test data and thrust model at 30 degree A.o.A. for different wind speeds	89
Figure 4.35: Test data and thrust model at 45 degree A.o.A. for different wind speeds	90
Figure 4.36: Test data and thrust model at 60 degree A.o.A. for different wind speeds	90
Figure 4.37: Surface fitting at 60 degree A.o.A. for hub force	92
Figure 4.38: Surface fitting at 45 degree A.o.A. for hub force	92
Figure 4.39: Surface fitting at 30 degree A.o.A. for hub force	93
Figure 4.40: Surface fitting at 0 degree A.o.A. for hub force	93
Figure 4.41: Test data and fitted hub force model at 0 degree A.o.A. w.r.t. the angular velocity of the rotor for different wind speeds	94
Figure 4.42: Test data and fitted hub force model at 30 degree A.o.A. w.r.t. the angular velocity of the rotor for different wind speeds	95
Figure 4.43: Test data and fitted hub force model at 45 degree A.o.A. w.r.t. the angular velocity of the rotor for different wind speeds	96
Figure 4.44: Test data and fitted hub force model at 60 degree A.o.A. w.r.t. the angular velocity of the rotor for different wind speeds	97
Figure 4.45: Test data and fitted hub force model at 30 degree A.o.A. w.r.t. free stream velocity for different rotor speeds	99
Figure 4.46: Test data and fitted hub force model at 45 degree A.o.A. w.r.t. free stream velocity for different rotor speeds	100
Figure 4.47: Surface fitting at 90 degree A.o.A. for rotor torque	101
Figure 4.48: Surface fitting at 60 degree A.o.A. for rotor torque	102
Figure 4.49: Surface fitting at 45 degree A.o.A. for rotor torque	102
Figure 4.50: Surface fitting at 30 degree A.o.A. for rotor torque	103
Figure 4.51: Surface fitting at 0 degree A.o.A. for rotor torque	103
Figure 4.52: Test data and fitted rotor torque model at 0 degree A.o.A. w.r.t. the angular velocity of the rotor for different wind speeds	104

Figure 4.53: Test data and fitted rotor torque model at 30 degree A.o.A. w.r.t. the angular velocity of the rotor for different wind speeds.....	105
Figure 4.54: Test data and fitted rotor torque model at 45 degree A.o.A. w.r.t. the angular velocity of the rotor for different wind speeds.....	106
Figure 4.55: Test data and fitted rotor torque model at 60 degree A.o.A. w.r.t. the angular velocity of the rotor for different wind speeds.....	107
Figure 4.56: Surface fitting at 60 degree A.o.A. for rolling moment	108
Figure 4.57: Surface fitting at 45 degree A.o.A. for rolling moment	109
Figure 4.58: Surface fitting at 30 degree A.o.A. for rolling moment	109
Figure 4.59: Surface fitting at 0 degree A.o.A. for rolling moment	110
Figure 4.60: Test data and fitted rolling moment model at 0 degree A.o.A. w.r.t. the angular velocity of the rotor for different wind speeds.....	111
Figure 4.61: Test data and fitted rolling moment model at 30 degree A.o.A. w.r.t. the angular velocity of the rotor for different wind speeds.....	112
Figure 4.62: Test data and fitted rolling moment model at 45 degree A.o.A. w.r.t. the angular velocity of the rotor for different wind speeds.....	113
Figure 4.63: Test data and fitted rolling moment model at 45 degree A.o.A. w.r.t. the angular velocity of the rotor for different wind speeds.....	114
Figure 4.64: Rotor interactions for thrust force	116
Figure 4.65: Step Response of BLDC Motor.....	117
Figure 4.66: Body coefficient in x axis vs. A.o.A.....	118
Figure 4.67: Body coefficient in z axis vs. A.o.A.....	118

LIST OF SYMBOLS

ρ	Density of air
Ω	Angular speed of the rotor
λ	Inflow ratio
ϕ	Local inflow angle
μ	Rotor advance ratio
σ	Solidity ratio
θ	Pitch angle of the blade
$\overline{C_d}$	Average drag coefficient
\bar{y}	Average of observed values
\hat{y}	Fitted Value
v_i	Induced velocity
C_y	Side force coefficient
C_H	Hub force coefficient
C_P	Pitching moment coefficient
C_R	Rolling moment coefficient
C_T	Thrust force coefficient
C_X, C_Z	Aerodynamic body coefficients of the quadrotor in x and z axes, respectively, at zero sideslip angle
C_l	Lift coefficient
I_{xx}, I_{yy}, I_{zz}	Inertia moments
U_P	Vertical velocity of blade

U_T	Horizontal velocity of blade
V_c	Climb velocity
V_d	Velocity in descending flight
\bar{c}	Average chord
p_∞	Pressure in the atmospheric level
v_∞	Velocity at downstream infinity
$\dot{x}, \dot{y}, \dot{z}$	Velocity of the rotor in x , y , and z body axes, respectively
x_b, y_b, z_b	Linear speeds of the quadrotor in x , y , and z axes in body-fixed reference frame, respectively
α_r	Rotor A.o.A
θ_{tw}	Twist angle
ΔF_H	Total horizontal forces acting on the blade
ΔF_V	Total vertical forces acting on the blade
e	Error between the observed/experimental value and fitted value
ϵ	Random error of observations
h	Vertical distance between the rotor axis and C.o.G.
k	Number of independent variables
N	Number of blades
p	Number of coefficients
R	Rolling moment
V	Free stream velocity (Wind tunnel speed)
x	Explanatory/Independent variable

y	Observed/measured value
y	Side force
Ψ	Azimuth angle
A	Area captured by rotor
H	Hub force
P	Pitching moment
Q	Rotor torque (Drag moment)
R	Radius of the rotor
S	Area of the quadrotor's body
T	Thrust force
a	Lift curve slope
b	Thrust force coefficient in hovering flight
d	Drag moment coefficient in hovering flight
dD	Drag acting on the blade
dL	Lift acting on the blade
l	Horizontal distance between the rotor axis and C.o.G.
m	Mass of the quadrotor
t	Time
y	Radius of blade section
Δp	Pressure increase
β	Sideslip angle
F_1, F_2, F_3, F_4	Forces arising from the rotation of the rotors

q_1, q_2, q_3, q_4	Rotor torque equation coefficients
t_1, t_2, t_3	Thrust force equation coefficients
h_1, h_2	Hub force equation coefficients
r_1, r_2	Rolling moment equation coefficients
R^2	R Squared (The Coefficient of Determination)
R_{adj}^2	Adjusted R Squared
β_1	Slope
β_0	Intercept
θ_0	Zero pitch angle

LIST OF ABBREVIATIONS

A.o.A.	Angle of Attack
BET	Blade Element Theory
BLDC	Brush-Less Direct Current
C.o.G.	Center of Gravity
SS_E	Error Sums of Squares
IB	Integral Backstepping
SS_R	Regression Sum of Squares
<i>RPM</i>	Revolutions Per Minute
SS_T	Total Sum of Squares
UAV	Unmanned Aerial Vehicle
VTOL	Vertical Take-Off and Landing

w.r.t

with respect to

CHAPTER 1

INTRODUCTION

1.1. Motivation and Objective

Quadrotor is a rotorcraft that is lifted by four rotors usually in cross configuration. In recent years, due to their broad field of applications, such as near field surveillance, exploration and survey, quadrotor Unmanned Aerial Vehicles (UAVs), have been studied both in civil and military applications. Quadrotor UAVs are preferred because of their basic structure, ability to move omnidirectionally and hover, and reduced gyroscopic effect which is caused by the reverse turning of rotors. It is a different type of rotorcraft compared with a conventional helicopter. On a conventional helicopter, torque resulted in main rotor is balanced by a tail rotor. The balance of hovering is affected adversely when a helicopter tries to move sideways while hovering. Unlike helicopters, quadrotors perform better hovering. Besides, helicopters are able to change their blade's A.o.A. to control the vehicle. On the other hand, quadrotors cannot which makes them mechanically simple compared to helicopters. However, besides the advantages, quadrotors have some disadvantages like low useful-load capacity and high energy consumption. It is important that some improvements should be made so that quadrotors can be used widely in practical areas.

In this study, analytical equations that represent aerodynamic forces and moments acting on the rotors and body are added to standard rigid body dynamic equations. Parameters (unknown coefficients) in the aerodynamic rotor model are determined through experimental identification. Method of least squares and surface fitting method are used to identify the parameters, and the reliability of the unknowns is checked by R squared and adjusted R squared. The objective of the study is to develop a high fidelity simulation model for the quadrotor at hand to support future controller development studies. Such a tool will allow researchers to evaluate novel high performance autopilot designs better in virtual environment, and hence reduce

the need for flight testing. Also the test setup and methodology developed in this study can be used to test and compare new rotor and body designs that will be done at Middle East Technical University (METU).

1.2. Literature Review

Rotor aerodynamics is essential in quadrotor modeling in order to make the model as real as possible. Forces and moments act on a quadrotor in three axes, namely thrust force, hub force, and side force; rolling moment, pitching moment, and drag moment should be included to a simulation model of a quadrotor accurately.

Bouabdallah and Siegwart [1] state that to get an accurate model of quadrotor it is necessary to add forces and moments created by the rotors in other axes such as hub force, rolling moment, and drag moment. In this study, a quadrotor simulation model is presented having major aerodynamic effects modeled with blade element and momentum theory. Besides, Integral Backstepping (IB) controller is developed [1]. In his PhD study, Bouabdallah [2] proposed the translational and rotational equations of motion of a quadrotor named OS4 including aerodynamic effects such as hub force, rolling moment, and friction. Based on the study conducted by Fay [3], analytical expressions for thrust force, hub force, rotor torque, and rolling moment are found by using blade element and momentum theories. Induced velocity is studied in hovering and forward flights. Forces and torques depending on the induced velocity, rotor velocity in z axis, and the angular speed of the rotor are also modeled. In this study, while calculation of induced velocity, rotor angle of attack is assumed to be very small [3]. Powers et. al. [4] bring in that performance and dynamic response of a micro UAV is affected by the aerodynamic influences. The aerodynamics of the forward flight and vertical flight are also studied in this study. The change of the thrust force with the rotor angular speed in various A.o.A. is presented. Parameters are found by using linear least squares method [4].

In hovering flight, rotor is assumed to produce thrust force and rotor torque only. However, while it is in motion, it produces forces and moments on other axes

depending on free stream velocity, rotor speed, and angle of attack. Hoffman et. al. [5] present induced velocity in vertical ascent and rapid descent conditions, and study the parameter estimation for induced velocity. Impacts of aerodynamic effects on attitude and altitude control are explored. Thanks to the accurate aerodynamic modeling, a precise trajectory control is implemented [5]. Huang et. al [6] state that blade flapping and thrust variations are the major aerodynamic effects on quadrotor. Disturbances are compensated and a controller is designed through the study of the effects of aerodynamics [6]. In order to design a faithful controller, it is significant to take into account the aerodynamics of the quadrotor [5, 6]. Belatti et. al. [7] mention the importance of rotor aerodynamics for micro UAVs. The relation between thrust force and angular speed of rotor, free stream velocity, and induced velocity are presented. First, the coefficients between the mentioned factors are found experimentally by using linear least squares method. Then, the reliability of the parameters is checked by R squared method [7]. Thrust force, hub force, and moment coefficients are calculated by using blade element and momentum method by Orsag and Bogdan [8]. In this study, thrust force is assumed to be proportional to the square of angular speed of rotor. By means of measuring voltage, RPM , induced velocity and thrust force, twist angle of the rotor is found [8]. By assuming thrust force and rotor torque are proportional to the square of the angular velocity of rotor, a dynamically feasible trajectories and controllers are designed by Mellinger, Michael and Kumar [9] to keep the quadrotor in a desired state. According to the study conducted by Naidoo et. al. [11], there are mainly five influences acting on a rotor, namely thrust force, hub force, rolling moment, drag moment, and ground effect. They propose that the vehicle requires great deal of thrust in order to perform corrective maneuvers and keep stability. A fixed-pitch propeller made of polyethylene is analyzed, and thrust performance of it is found satisfactory [11]. In the study [12], it is concluded that the flexibility of the propeller is very important. In addition, it is stated that the location of the C.o.G. plays an important role in torque calculations, and using a model accounting for the aerodynamics of the propellers is important to design a reliable controller [12].

As a result of the literature, the aerodynamics of the quadrotor is decided to be studied experimentally to establish a high fidelity simulation.

1.3. History

1.3.1. Manned Quadrotor Studies

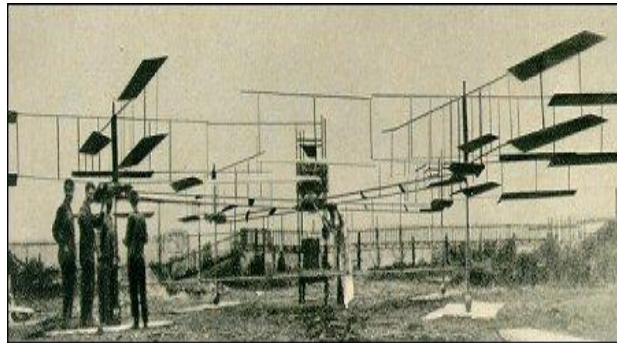


Figure 1.1: Breguet-Richet Gyroplane No.1 [13]

Breguet-Richet Gyroplane No.1 [Figure 1.1] was built by Louis and Jacques Breguet in association with Professor Charles Richet in 1907. Although it was not the first helicopter to fly freely, it was the first vehicle to rise with a pilot vertically off the ground by means of a rotating-wing system of lift. The pilot of the vehicle, M. Volumard, was 68 *kg* which is cited to be a reason of why he was chosen. The vehicle rose to about 0.60 *m*; but it was uncontrollable in horizontal flight. However, in 1907, Louis Breguet had managed to build a primitive helicopter which could lift a man into the air. The following year, Breguet produced another helicopter, named Gyroplane No.2, with 25-foot rotors which rose vertically to 4.5 *m*, and flew for a short period of time. Although it was controllable, the vehicle landed unsuccessfully. Gyroplane No.2 was produced with 55 *hp* Renault engine and two forward-tilting two-blade rotors. In the late summer of 1908, it was badly damaged, but it was rebuilt again next spring [13].

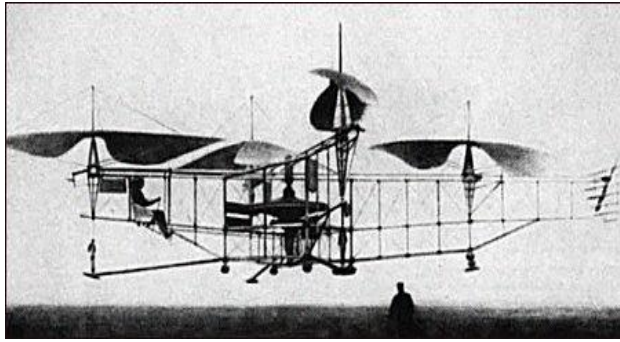


Figure 1.2: Oemichen No.2 [14]

Etienne Oemichen began to study rotating-wing designs in 1920s, and built six different vertical take-off machines. The first of these machines failed to produce enough lift, and so to ensure the aircraft would have stability and would be able to lift, Oemichen added a hydrogen filled balloon on top of it. The helicopter No.2 [Figure 1.2] flew in 11 November 1922 was the most noteworthy aircraft among his inventions. It has no less than 4 rotors and 8 propellers with a single 120 *hp* Le Rhone rotary engine which was later substituted with an 180hp Gnome engine. The Oemichen No.2 could be described as a steel-tube framework of cruciform layout, which had 2-blade paddle-shaped rotors at the extremities of its four arms. It showed a considerable degree of stability and controllability. His final design reverted back to his first aircraft which is a balloon-assisted aircraft. In the Oemichen No.2, eight small propellers were used to satisfy control and lateral movement. In 1924, it was established to be the first rotary wing distance record which is 360 *m*. Then it flew 1 km in 7 minutes 40 seconds. It had a maximum endurance of 14 minutes. Even though it was sufficiently controllable it was not a practical aircraft [14].

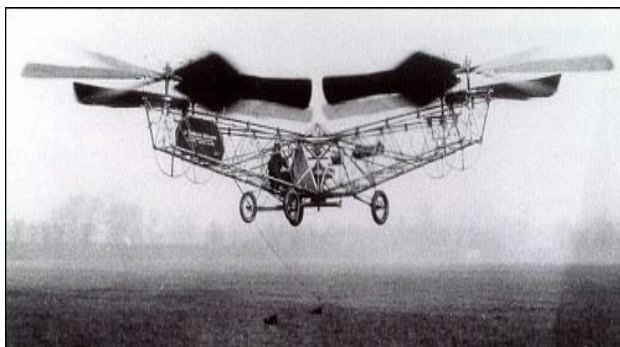


Figure 1.3: De Bothezat [15]

Dr. George de Bothezat and Ivan Jerome built an X-shaped structured aircraft which is 1678 kg supported by a six-blade rotor. Collective pitch control was used on the vehicle. It made its first flight in October 1922, and flew up to 5 m which was the maximum height it reached. De Bothezat [Figure 1.3] that carried 3 passengers was stable, and it proved that a practical helicopter was possible theoretically. However it had reliability problems due to its complex structure, and it required too much pilot work [15].

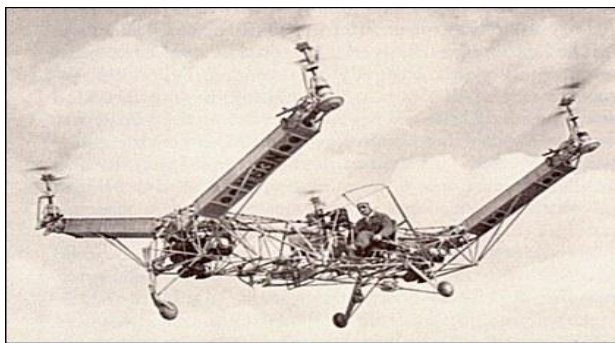


Figure 1.4: Convertawings Model A [16]

The Convertawings [Figure 1.4], whose four rotors were placed laterally on outriggers in two tandem pairs, was first flown in 1956. It was powered by two engines, and the control, which is not cyclic but collective, is assured by differential variation of thrust between the rotors. The prototype which successfully flew in 1955 had its fuselage out of tubular steel. Although it achieved a remarkable success, the support for the vehicle was ceased due to the cutbacks in spending of defence [16].

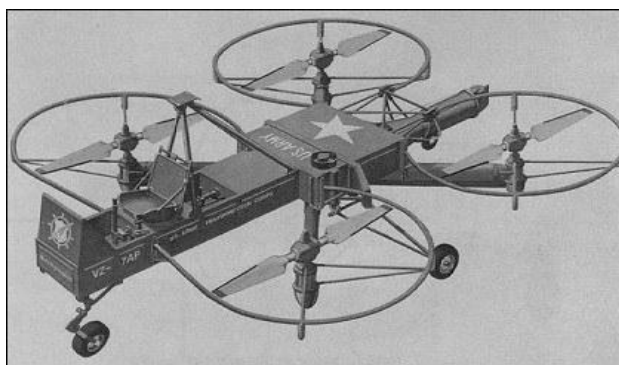


Figure 1.5: Curtiss-Wright VZ-7 [17]

Curtiss-Wright VZ-7 [Figure 1.5] was developed for and delivered to the US Army in 1958. The fuselage carried the pilot's seat, fuel tanks, and flight controls. The design of the aircraft, as well as the directional control, which was achieved by varying the thrust of one of the four propellers, was quite simple, and it had proved to be easy to operate. However, while it was successful in hovering and flying forward, it was withdrawn due to not meeting the requirements [17].


Although some manned designs of quadrotor achieved successful flight, they suffered from poor performance, control difficulties, stability problems, and excessive pilot work. With the advances in technology that made manufacturing of miniature low cost sensors and actuators possible, unmanned quadrotor applications have been widely popular all around the world. In recent years, quadrotors have been designed as UAVs, and they are produced for commercial or academic aims.

1.3.2. Unmanned Quadrotor Studies

Unmanned quadrotor studies are held in commercial, military, and academic environments. It is a useful tool for academics to apply new ideas in modeling and control which is the reason of the studying the vehicle in this thesis.

Some notable quadrotor research studies performed in universities are listed in Table 1.1.

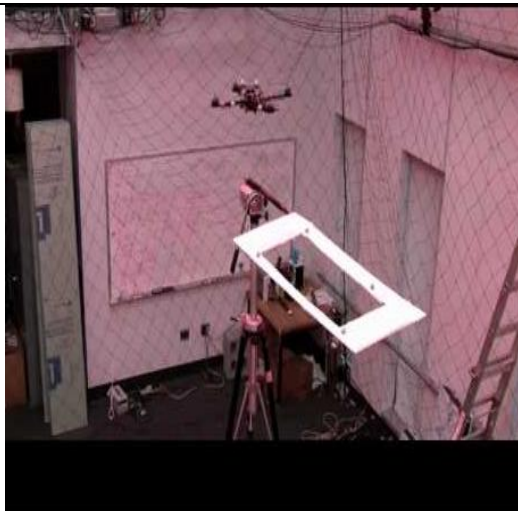
Table 1.1: Unmanned Quadrotor Studies at the Universities

	<p>OS4, Autonomous System Laboratory:</p> <p>A quadrotor UAV named OS4 is designed in the PhD study conducted by Bouabdallah. The importance of the aerodynamics of a quadrotor is mentioned. Besides, five different controllers were developed [2].</p>
---	--



Stanford Testbed of Autonomous Rotorcraft for Multi-Agent Control (STARMAC),

Stanford University: A precise trajectory control is implemented by taking into consideration of the rotor aerodynamics [5].



GRASP Lab. ,

University of Pennsylvania:

The design and control of a micro quadrotor is presented by Kushleyev et. al. [10]. Besides, the autonomous quadrotor is controlled to precisely fly along aggressive trajectories by Daniel Mellinger, Dr. Nathan Michael, and Professor Vijay Kumar [29].



Michael Achtelik's Thesis,

Technische Universität München:

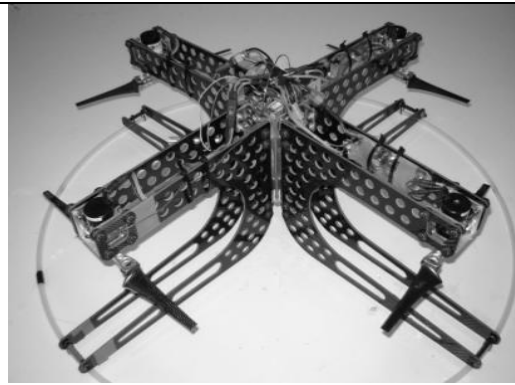
Parameter estimation is held for the aerodynamic coefficients of the rotor used in the study. In addition, control of the vehicle is studied [18].



Variable-Pitch Quadrotor Project

Mark Cutler,

MIT: A variable-pitch quadrotor capable of aggressive aerobatic maneuvers is developed and proposed for control among fixed-pitch quadrotors [21].



X-4 Flyer,

Australian National University: The attitude dynamics of the vehicle is analyzed in a larger platform. Disturbance rejection and control sensitivity are studied by Pounds et.al. [23]



Institute for Dynamic Systems and Control,

ETH Zurich:

The Flying Machine Arena is used in a range of projects performed at ETHZ, at the Institute for Dynamic Systems and Control and other research laboratories [30].

1.4. Quadrotor Preliminaries

1.4.1. Working Principle

Throttle, yaw, roll, and pitch controls are adjusted by changing the angular velocity of each rotor. In the quadrotor used in this study, front and rear rotors turn clockwise; left and right rotors turn counterclockwise direction. Front rotor (1), right rotor (2), rear rotor (3), and left rotor (4) of the quadrotor are seen in Figure 1.6.



Figure 1.6: Body coordinate system of the quadrotor [18]

Throttle control can be achieved by giving the same amount of *RPM* input (Ω) to every rotor as shown in Figure 1.7. Ω_h is the required angular velocity of the rotors to keep the vehicle in hovering flight. In hovering flight, total thrust force produced by the four rotors is equal to the weight of the quadrotor.

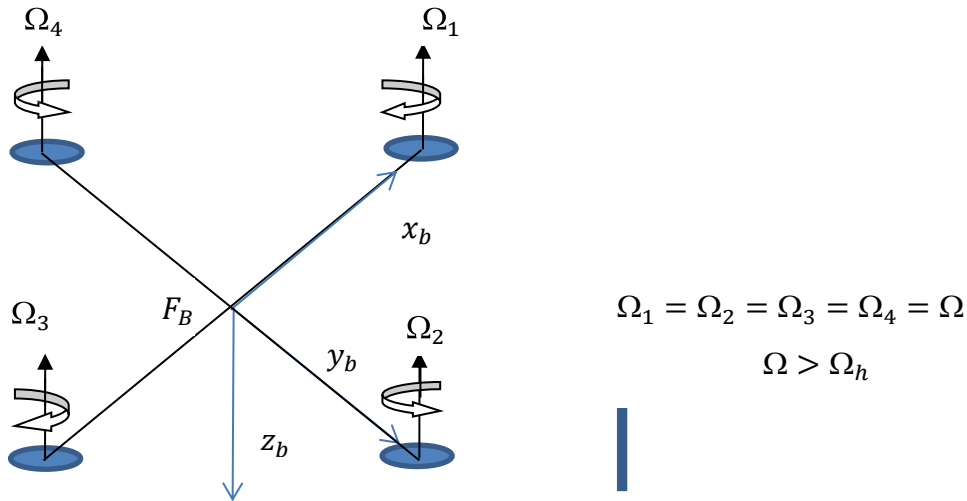


Figure 1.7: Throttle Control

Positive yawing movement can be achieved by increasing the angular velocity of the front and rear rotors as shown in Figure 1.8.

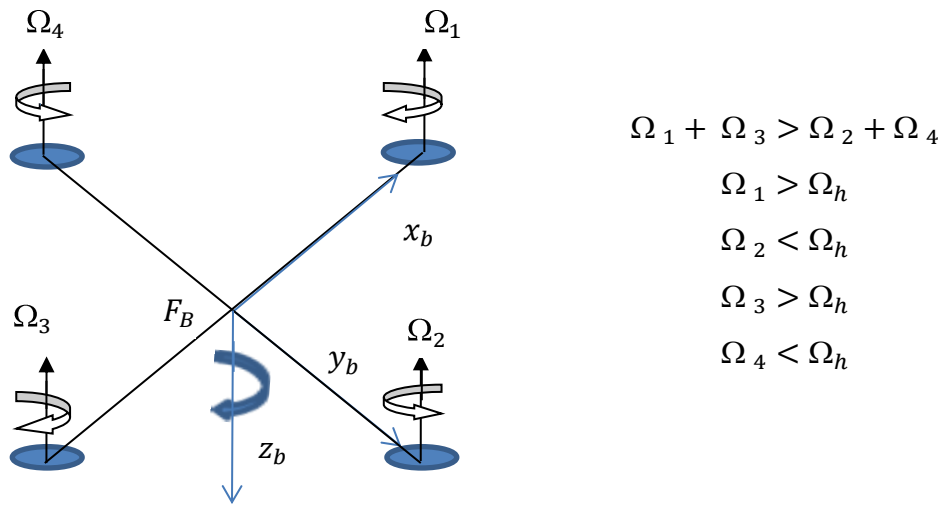


Figure 1.8: Yaw Control

Positive rolling movement can be achieved by increasing the angular velocity of the left rotor and decreasing the right rotor [Figure 1.9].

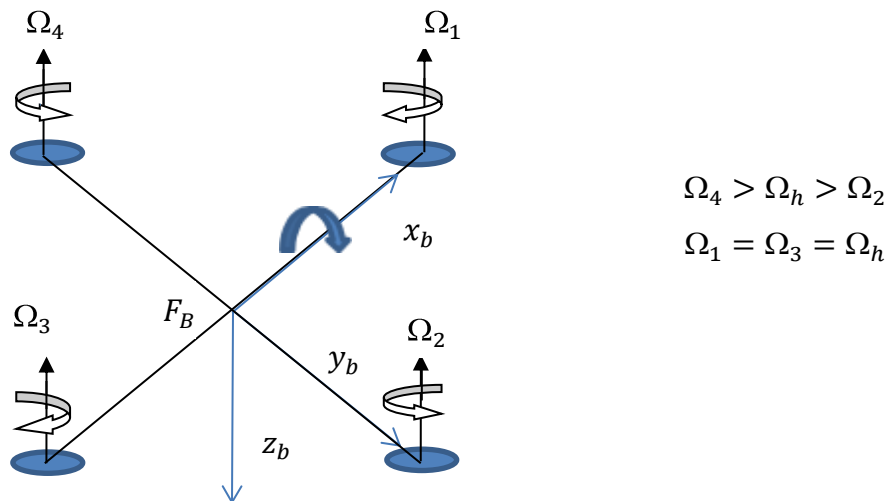


Figure 1.9: Roll Control

Positive pitching movement can be performed by increasing the angular velocity of the front rotor and decreasing the rear rotor [Figure 1.10].

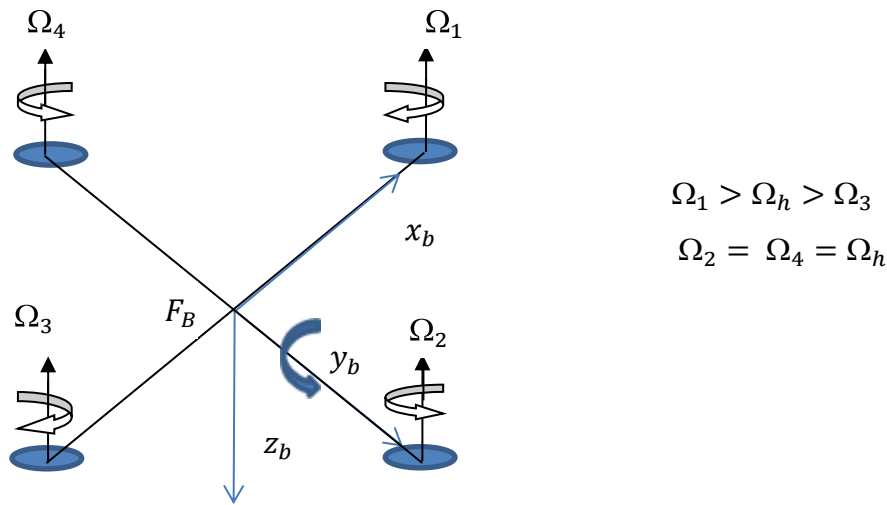


Figure 1.10: Pitch Control

1.4.2. Advantages and Drawbacks

Quadrotors have several advantages over fixed-wing UAVs and helicopters which make them more practical to use. Advantages and disadvantages of a quadrotor helicopter compared to other UAVs are presented in Table 1.2.

Table 1.2: Advantages and Drawbacks of the Quadrotor

Advantages	Drawbacks
VTOL and hover capabilities	High energy consumption
Better hovering w.r.t conventional helicopters due to the reduced gyroscopic effect	Unscalable <i>RPM</i> control
Simple mechanics and aerodynamics (They do not require mechanical linkages to change the rotor blade.)	Low useful load capacity
Moving omnidirectionally, maneuverable flight	
Safe and close flights by enclosing the rotors	
Indoor usage, low speed flights w.r.t. the fixed-wing aircrafts	

Lower cost and better robustness because of mechanical simplicity	
---	--

1.4.3. Applications

Some present and potential quadrotor applications are summarized in Table 1.3.

Table 1.3: Applications

Military	Civil
Surveillance	Plotting (imaging) and mapping
Exploration	Taking photographs and videos
Border patrolling	Collecting meteorological data
Mine detection	Aerial delivery, communication
Indoor navigation	Damage assessment and rescue (e.g. flood, earthquakes)
Aerial reconnaissance	Gaming
	Experimental studies (e.g. research in control engineering)

1.5. Contribution of the Thesis

In a vast majority of quadrotor control research in the literature, rotors are modeled to produce thrust force and rotor torque that depends on rotor speed only. Effects of vehicle motion on rotor loads, and forces and moments generated on secondary axes are usually ignored. In this thesis, parameters of an aerodynamic rotor model that gives rotor forces and moments on three axes are experimentally identified for a commercial off the shelf quadrotor widely used in controls research around the world.

The main objective of this thesis is to develop a high fidelity simulation model for the AscTec Hummingbird quadrotor used for controls research at the METU Aerospace Engineering Department. A rotor model based on blade element and

momentum theories is studied. However, an empirical model which determines the forces and moments on the rotor is integrated into the simulation model. Forces and moments acting on the quadrotor in a wide range of flight conditions are measured in wind tunnel tests, and the gathered data is used to estimate the parameters of the aerodynamic model. The model developed will serve as a high fidelity simulation tool to help controller development research by reducing the cost of flight tests required for controller tuning. The quadrotor test setup developed for this thesis can also potentially be used for testing of new quadrotor designs.

1.6. Structure of the Thesis

Chapter 1 provides information about quadrotor UAVs, motivation of the study, literature survey, history of the quadrotor, and contribution of the thesis. Chapter 2 focuses on the aerodynamics of a quadrotor based on the sources [3, 19, 20]. Chapter 3 deals with parameter estimation. It presents the test setup and gives information about the experiments. Based on the source conducted by Montgomery [22], parameter estimation method used in this study is also explained in this chapter. Chapter 4 shows parameter estimation results. Chapter 5 summarizes the results of the study and concludes the thesis. Some discussions and recommendations are also made for future works in this chapter. Chapter 6 presents the Appendix which includes the properties of the quadrotor and rotor used in this study.

CHAPTER 2

ROTOR AERODYNAMICS

The rotor generates an upward thrust by driving a column of air downwards through the rotor plane and the relation between the produced thrust and the velocity related to the air can be achieved by using a set of conservation rules, named energy, momentum, and mass conservation [19]. This concept is called the momentum theory which defines the mathematical model of an ideal actuator disc found by Galuert for aircraft propellers based on the study of W. J. M. Rankine and R. E. Froude [19]. Induced velocity, which can be described as the additional velocity imported by the rotor, has different formulations in different flight conditions, named hover, vertical climb, vertical descent, and forward flight conditions [Table 2.1]. The importance of the induced velocity increases with an expanding rotor. Hence, aerodynamics of rotor becomes important in rotorcraft modeling.

On the other hand, the blade element theory is used to derive the equations of forces and moments while the rotorcraft is in motion. In hovering and vertical flight, the rotor produces thrust force and rotor torque only. However, while it is in motion, hub force, side force, rolling moment, and pitching moment are expected to occur. The equations of thrust force, hub force, side force, pitching moment, and rolling moment are found through the blade element theory.

2.1. Momentum Theory

2.1.1. Momentum Theory in Hovering Flight

Based on the sources [3, 19, 20, 25, 26], the following assumptions have been made in order to derive the induced velocity:

1. Flow is incompressible.
2. There is no discontinuity in velocity, and it is uniform at all points on the disc.
3. Pressure is uniformly spread.

4. Induced velocity is assumed to be uniform at all points on the disc.
5. There is infinite number of blades so that the rotor can be thought as a circular disc.
6. Disc is infinitesimally thin.

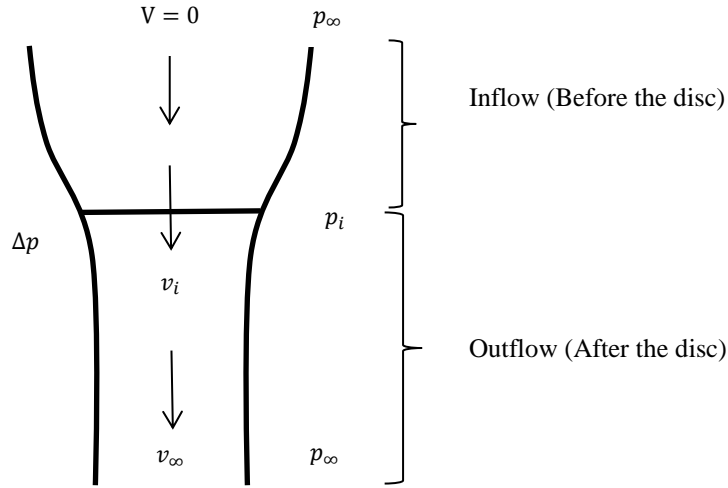


Figure 2.1: Momentum theory in hovering flight

The following relation can be generated in the inflow part by using the pressure relation mentioned above through the conservation of energy [Figure 2.1].

$$p_\infty = p_i + \frac{1}{2} \rho v_i^2 \quad (2.1)$$

In the outflow part, the conservation of energy can be written as follows:

$$\Delta p + p_i + \frac{1}{2} \rho v_i^2 = p_\infty + \frac{1}{2} \rho v_\infty^2 \quad (2.2)$$

When the pressure in the atmospheric level (Equation 2.1) is inserted into the Equation 2.2, the following relation is obtained:

$$\Delta p + p_\infty = p_\infty + \frac{1}{2} \rho v_\infty^2 \quad (2.3)$$

The increase of the pressure at the disc is found as follows:

$$\Delta p = \frac{1}{2} \rho v_{\infty}^2 \quad (2.4)$$

Pressure is the ratio of force to the area over which that force is distributed. Hence, the increase of pressure Δp is also formulated as follows:

$$\Delta p = \frac{T}{A} \quad (2.5)$$

According to the conservation of momentum, the thrust developed by a rotor moving along its axis at a speed V is equal to the rate of mass flow through the disc times velocity of the air after it passes through the rotor:

$$T = \dot{m} \Delta V \quad (2.6)$$

$$T = \rho A v_i (v_{\infty} - V) \quad (2.7)$$

where

$$\rho A v_i = \dot{m} \quad (2.8)$$

\dot{m} is known as mass flow rate. Since free stream velocity, V , equals to zero in hovering flight, Equation 2.7 is formed as follows:

$$T = \rho A v_i v_{\infty} \quad (2.9)$$

Thrust expression in Equation 2.9 is inserted into Equation 2.5 in order to find the relation between v_i and v_{∞} .

$$\Delta p = \frac{\rho A v_i v_{\infty}}{A}$$

$$\Delta p = \rho v_i v_{\infty} \quad (2.10)$$

$$\frac{1}{2} \rho v_{\infty}^2 = \rho v_{\infty} v_i \quad (2.11)$$

Then, the following relation is obtained:

$$v_{\infty} = 2v_i \quad (2.12)$$

Thrust force can be formulated as:

$$T = \rho A v_i v_{\infty} = 2 \rho A v_i^2 \quad (2.13)$$

$$v_i = \sqrt{\frac{T}{2 \rho A}} \quad (2.14)$$

Equation 2.14 is the induced velocity in hovering flight which is represented as follows:

$$v_h = \sqrt{\frac{T}{2\rho A}} \quad (2.15)$$

2.1.2. Momentum Theory in Vertical Climb and Vertical Descent Flights

Similar equations can be derived for vertical climb flight by using the conservation of energy [Figure 2.2]:

Pressure in the inflow part [Figure 2.2] in vertical climb flight is formulated as follows:

$$p_\infty + \frac{1}{2}\rho V_c^2 = p_i + \frac{1}{2}\rho(V_c + v_i)^2 \quad (2.16)$$

Pressure relation in the outflow part [Figure 2-2] in vertical climb flight is formulated as follows:

$$p_i + \frac{1}{2}\rho(V_c + v_i)^2 + \Delta p = p_\infty + \frac{1}{2}\rho(V_c + v_\infty)^2 \quad (2.17)$$

Thrust expression in vertical climb flight is expressed as follows:

$$T = \rho A v_\infty (V_c + v_i) = 2\rho A v_i (V_c + v_i) \quad (2.18)$$

Then, the above equation is formed as:

$$v_i^2 + v_i V_c - \frac{T}{2\rho A} = 0 \quad (2.19)$$

The roots of Equation 2.19 are found as:

$$v_{i1,2} = -\frac{V_c}{2} \pm \sqrt{\left(\frac{V_c}{2}\right)^2 + \left(\frac{T}{2\rho A}\right)} \quad (2.20)$$

The positive root of the above equation is valid for induced velocity expression:

$$v_i = -\frac{V_c}{2} + \sqrt{\left(\frac{V_c}{2}\right)^2 + \left(\frac{T}{2\rho A}\right)} \quad (2.21)$$

In the case of vertical descent, the free stream velocity V_c is negative which can be denoted as V_d , however the induced velocity remains positive because the rotor keeps generating lift. Then, the thrust equation for vertical climb flight is formed for vertical descent flight as follows:

$$T = -\rho A v_\infty (-V_d + v_i) \quad (2.22)$$

$$v_i^2 - v_i V_d + \frac{T}{2\rho A} = 0 \quad (2.23)$$

Induced velocity in vertical descent condition is formulated as follows:

$$v_i = \frac{V_d}{2} \pm \sqrt{\left(\frac{V_d}{2}\right)^2 - \left(\frac{T}{2\rho A}\right)} \quad (2.24)$$

$$V_d = -V_c \quad (2.25)$$

$$v_i = -\frac{V_c}{2} + \sqrt{\left(\frac{-V_c}{2}\right)^2 - \left(\frac{T}{2\rho A}\right)} \quad (2.26)$$

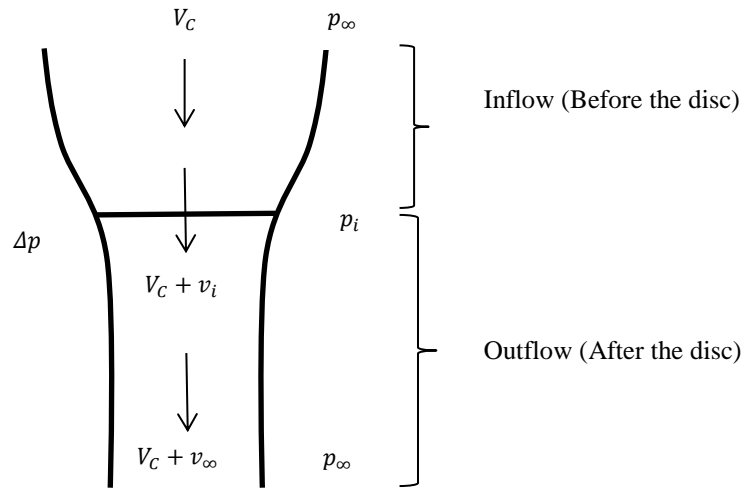


Figure 2.2: Momentum theory in vertical climb [19, 20]

2.1.3. Momentum Theory in Forward Flight

The aerodynamics of the rotor in forward flight is more complex than the hovering and vertical flights. In forward flight, free stream velocity comes to the rotor at an angle of attack. The directions of the velocities are shown in Figure 2.3.

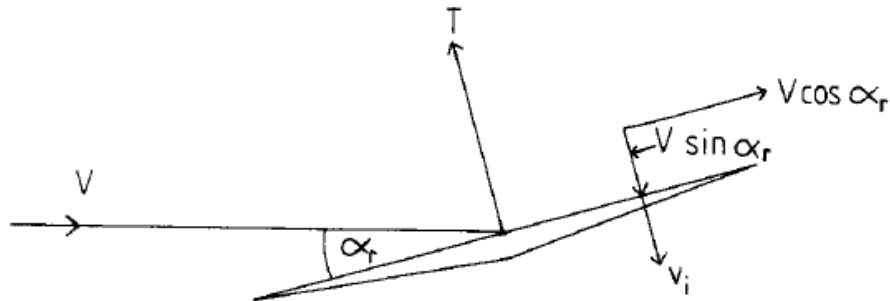


Figure 2.3: Disc incidence and component velocities in forward flight [19]

Based on the sources [3, 19, 26] Figure 2.4 is drawn for the flow over the disc in forward flight:

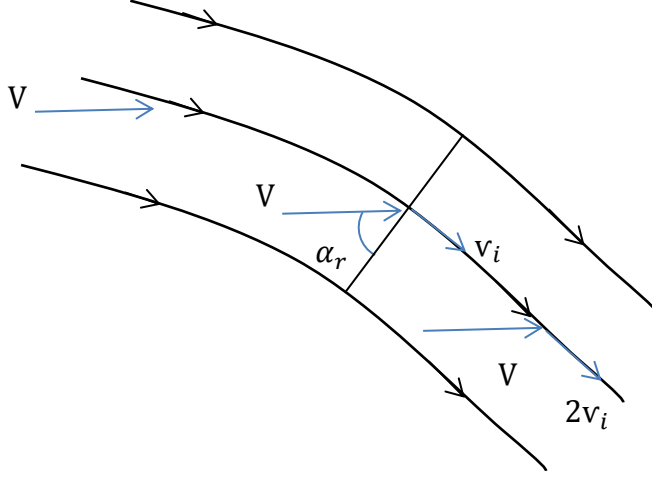


Figure 2.4: Momentum theory in forward flight

$$T = v_{\infty} \rho A \sqrt{(V \cos \alpha_r)^2 + (V \sin \alpha_r + v_i)^2}$$

$$T = 2v_i \rho A \sqrt{(V \cos \alpha_r)^2 + (V \sin \alpha_r + v_i)^2} \quad (2.27)$$

$$\left(\frac{T}{2\rho A} \right) = v_i \sqrt{(V \cos \alpha_r)^2 + (V \sin \alpha_r + v_i)^2} \quad (2.28)$$

$$\left(\frac{T}{2\rho A} \right)^2 = v_i^2 \{ (V \cos \alpha_r)^2 + (V \sin \alpha_r + v_i)^2 \} \quad (2.29)$$

$$v_i^2 \{ V^2 (\cos \alpha_r)^2 + V^2 (\sin \alpha_r)^2 + v_i^2 + 2v_i V \sin \alpha_r \} - \left(\frac{T}{2\rho A} \right)^2 = 0 \quad (2.30)$$

$$v_i^2 (V^2 + v_i^2 + 2v_i V \sin \alpha_r) - \left(\frac{T}{2\rho A} \right)^2 = 0 \quad (2.31)$$

$$v_i^4 + 2v_i^3 V \sin \alpha_r + v_i^2 V^2 - \left(\frac{T}{2\rho A} \right)^2 = 0 \quad (2.32)$$

In order to simplify Equation 2.32, α_r can be assumed to be very small, which means that the free stream velocity is horizontal to the rotor hub.

$$V = \sqrt{\dot{x}^2 + \dot{y}^2} \quad (2.33)$$

Equation 2.32 is formed as follows through the assumption in Equation 2.33 based on the source [3]:

$$v_i^4 + v_i^2 V^2 - \left(\frac{T}{2\rho A}\right)^2 = 0 \quad (2.34)$$

To solve Equation 2.34 the following relation is generated:

$$v_i^2 = x \quad (2.35)$$

Then, the equation 2.34, is formed as follows:

$$x^2 + xV^2 - \left(\frac{T}{2\rho A}\right)^2 = 0 \quad (2.36)$$

$$x_{1,2} = -\frac{V^2}{2} \pm \left(\frac{\sqrt{\left(V^4 + 4\left(\frac{T}{2\rho A}\right)^2\right)}}{2} \right) \quad (2.37)$$

Because x equals to v_i^2 , the induced velocity is found in forward flight as follows:

$$v_i = \sqrt{-\frac{V^2}{2} + \sqrt{\left(\frac{V^2}{2}\right)^2 + \left(\frac{T}{2\rho A}\right)^2}} \quad (2.38)$$

The induced velocity representations in different flight conditions are summarized in Table 2.1.

Table 2.1: Induced velocity in different flight conditions

Relation between induced velocity and thrust	Induced velocity formulization	Flight case
$T = 2\rho A v_i^2$	$v_i = \sqrt{\frac{T}{2\rho A}}$	Hover
$T = 2\rho A v_i (V_c + v_i)$	$v_i = -\frac{V_c}{2} + \sqrt{\left(\frac{V_c}{2}\right)^2 + \left(\frac{T}{2\rho A}\right)}$	Vertical climb
$T = -2\rho A v_i (-V_d + v_i)$ $V_d = -V_c$	$v_i = \frac{V_d}{2} + \sqrt{\left(\frac{V_d}{2}\right)^2 - \left(\frac{T}{2\rho A}\right)}$	Vertical descent
$T = 2\rho A v_i \sqrt{V^2 + v_i^2}$	$v_i = \sqrt{-\frac{V^2}{2} + \sqrt{\left(\frac{V^2}{2}\right)^2 + \left(\frac{T}{2\rho A}\right)^2}}$	Forward flight

2.2. Blade Element Theory

Forces and moments acting on front rotor are presented in Figure 2.5. According to the body-fixed reference frame, thrust force is in the $-z_b$ axis, hub force is in the direction of free stream velocity, and has components in $-x_b$ and $-y_b$ axes. As the rotor turns clockwise direction, there is a rolling moment in the same direction, and it has components in $-x_b$ and $-y_b$ axes like hub force. Rotor torque is in counter clockwise direction when a rotor turns in clockwise direction.

Based on the sources [3, 19, 20], blade element theory is expressed as follows:

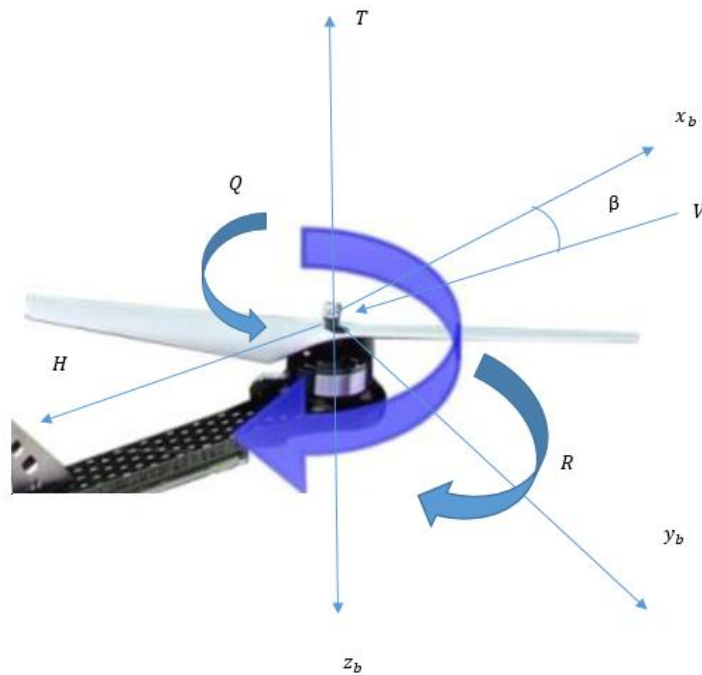


Figure 2.5: Forces and moments on a rotor [18]

In order to integrate forces and moments along the blade span, some simplifications are made.

Assumptions:

1. The blades of the rotors are assumed to be rigid and have a constant chord.
2. The lift coefficient of the blade airfoil varies linearly with angle of attack.
3. The pitch angle of the blade changes linearly with radial position.
4. Lift acting on a blade has a greater magnitude than drag.
5. The local inflow angle (ϕ) is assumed to be very small.
6. Only lift and drag forces are assumed to act on blade a section.

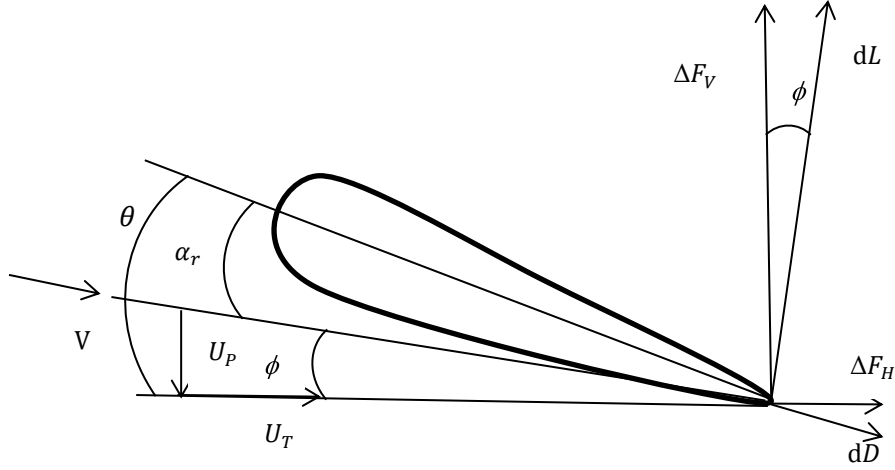


Figure 2.6: Blade element theory [19]

Some useful integrals used in blade element theory are written in Table 2.2.

Table 2.2: Integrals used in blade element theory

$\int_0^{2\pi} \sin \Psi \, d\Psi$	0
$\int_0^{2\pi} \cos \Psi \, d\Psi$	0
$\int_0^{2\pi} \sin \Psi \cos \Psi \, d\Psi$	0
$\int_0^{2\pi} \sin^2 \Psi \, d\Psi$	π
$\int_0^{2\pi} \cos^2 \Psi \, d\Psi$	π
$\int_0^{2\pi} \sin^2 \Psi \cos \Psi \, d\Psi$	0
$\int_0^{2\pi} \sin^3 \Psi \, d\Psi$	0

Total vertical and horizontal forces on the blade in Figure 2.6 are written respectively as follows [3, 19]:

$$\Delta F_v = dL \cos \phi - dD \sin \phi \quad (2.39)$$

$$\Delta F_H = dL \sin \phi + dD \cos \phi \quad (2.40)$$

From the geometry in Figure 2.7, we can write the translational speeds of the rotor in the x and z directions as:

$$\dot{x} = -V \cos \alpha_r, \quad \dot{z} = -V \sin \alpha_r$$

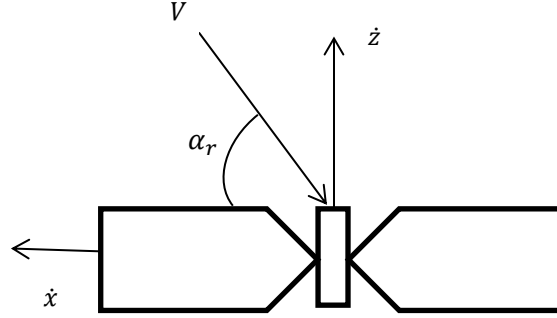


Figure 2.7: Directions of the velocities for a rotor [4]

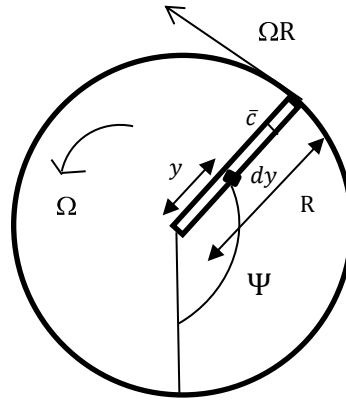


Figure 2.8: Rotor disc view from above [19]

$$\text{Where } r = \frac{y}{R} \text{ and } dy = R dr$$

Using above relations, the advance ratio and the inflow ratio can be written as follows [19]:

$$\mu = \frac{V \cos \alpha_r}{\Omega R} = \frac{-\dot{x}}{\Omega R} \quad (2.41)$$

$$\lambda = \frac{(v_i + V \sin \alpha_r)}{\Omega R} = \frac{(v_i - \dot{z})}{\Omega R} \quad (2.42)$$

Local lift and local drag are formulated as in the following equations, respectively:

$$dL = \frac{1}{2}\rho \left(\sqrt{U_T^2 + U_P^2} \right)^2 C_l \bar{c} dy \quad (2.43)$$

$$dD = \frac{1}{2}\rho \left(\sqrt{U_T^2 + U_P^2} \right)^2 \bar{C}_d \bar{c} dy \quad (2.44)$$

The components of the free stream velocity are defined as U_T and U_P . The inflow angle, ϕ , can be formulated by using the components of the free stream velocity:

$$\sin \phi = \frac{U_P}{\left(\sqrt{U_T^2 + U_P^2} \right)} \quad (2.45)$$

$$\cos \phi = \frac{U_T}{\left(\sqrt{U_T^2 + U_P^2} \right)} \quad (2.46)$$

The vertical and horizontal components of free stream velocity are expressed as follows thanks to Figure 2.8:

$$U_P = v_i - \dot{z} = \Omega R \lambda \quad (2.47)$$

$$U_T = \Omega y + V \sin \Psi = \Omega R \left(\frac{y}{R} + \mu \sin \Psi \right) \quad (2.48)$$

Thus, total vertical forces acting on a blade without using any of the assumptions mentioned above is formulated as:

$$\begin{aligned} \Delta F_V = & \frac{1}{2}\rho \left(\sqrt{U_T^2 + U_P^2} \right)^2 C_l \bar{c} dy \frac{U_T}{\left(\sqrt{U_T^2 + U_P^2} \right)} \\ & - \frac{1}{2}\rho \left(\sqrt{U_T^2 + U_P^2} \right)^2 \bar{C}_d \bar{c} dy \frac{U_P}{\left(\sqrt{U_T^2 + U_P^2} \right)} \end{aligned} \quad (2.49)$$

$$\Delta F_V = \frac{1}{2}\rho \left(\sqrt{U_T^2 + U_P^2} \right) \bar{c} dy (C_l U_T - \bar{C}_d U_P) \quad (2.50)$$

$$\begin{aligned} \Delta F_V = & \frac{1}{2}\rho \left(\sqrt{\left(\Omega R \left(\frac{y}{R} + \mu \sin \Psi \right) \right)^2 + (\Omega R \lambda)^2} \right) \bar{c} dy \left(C_l \Omega R \left(\frac{y}{R} \right. \right. \\ & \left. \left. + \mu \sin \Psi \right) - \bar{C}_d \Omega R \lambda \right) \end{aligned} \quad (2.51)$$

By using the following assumptions, thrust coefficient for one blade is formulated.

- $\Delta F_V = dL = dT$ (see assumption 5)
- $dL = \frac{1}{2}\rho U_T^2 C_l \bar{c} dy$ (see assumption 5)

- $\phi = \frac{U_P}{U_T}$ (see assumption 5)
- $\theta = \theta_0 + r\theta_{tw}$ (see assumption 3)
- $C_l = a\alpha$ (see assumption 2)

$$dC_T = \frac{dT}{\rho A (\Omega R)^2} = \frac{\frac{1}{2} \rho U_T^2 C_l \bar{c} dy}{\rho \pi R^2 (\Omega R)^2} \quad (2.52)$$

$$C_l = a(\theta - \phi) = a \left(\theta_0 + r\theta_{tw} - \frac{\Omega R \lambda}{\Omega R \left(\frac{y}{R} + \mu \sin \Psi \right)} \right) \quad (2.53)$$

$$= \frac{\frac{1}{2} \rho (\Omega R (r + \mu \sin \Psi))^2 a \left(\theta_0 + r\theta_{tw} - \frac{\Omega R \lambda}{\Omega R (r + \mu \sin \Psi)} \right) \bar{c}}{\rho \pi R^2 (\Omega R)^2} R dr \quad (2.54)$$

For N blades, the above expression is multiplied by N:

$$\begin{aligned} dC_T &= N \times \frac{\bar{c}}{2\pi R} (r + \mu \sin \Psi)^2 a \left(\theta_0 + r\theta_{tw} - \frac{\Omega R \lambda}{\Omega R (r + \mu \sin \Psi)} \right) dr \\ &= \frac{1}{2} \sigma (r + \mu \sin \Psi)^2 a \left(\theta_0 + r\theta_{tw} - \frac{\lambda}{(r + \mu \sin \Psi)} \right) dr \\ C_T &= \frac{1}{2} \sigma a \int_0^1 \frac{1}{2\pi} \int_0^{2\pi} (r + \mu \sin \Psi)^2 \left(\theta_0 + r\theta_{tw} \right. \\ &\quad \left. - \frac{\lambda}{(r + \mu \sin \Psi)} \right) d\Psi dr \end{aligned} \quad (2.55)$$

The ratio of blade area and the disc area is known as solidity ratio, and formulated as:

$$\sigma = \frac{N\bar{c}}{\pi R} \quad (2.56)$$

Equation 2.55 is divided into two groups to take the integral. The first part of the integral is w.r.t. azimuth angle:

$$\begin{aligned} &\frac{1}{2\pi} \int_0^{2\pi} ((r + \mu \sin \Psi)^2 (\theta_0 + r\theta_{tw}) - \lambda (r + \mu \sin \Psi)) d\Psi \\ &= \frac{1}{2\pi} (2\pi r^2 + \pi \mu^2) (\theta_0 + r\theta_{tw}) - \frac{1}{2\pi} (2\pi \lambda r) \\ &= \left(r^2 + \frac{\mu^2}{2} \right) (\theta_0 + r\theta_{tw}) - \lambda r \end{aligned} \quad (2.57)$$

When the above result is put into the second part of integration, which is w.r.t. r , the following expression is formed:

$$C_T = \frac{1}{2} \sigma a \int_0^1 \left(\left(r^2 + \frac{\mu^2}{2} \right) (\theta_0 + r \theta_{tw}) - \lambda r \right) dr$$

$$C_T = \frac{1}{2} \sigma a \left(\theta_0 \frac{r^3}{3} + \theta_{tw} \frac{r^4}{4} + \theta_0 \frac{\mu^2}{2} r + \theta_{tw} \frac{\mu^2}{2} \frac{r^2}{2} - \lambda \frac{r^2}{2} \right)$$

Where r is from zero to 1. When r is written in the above equation, the following relation is obtained:

$$C_T = \frac{1}{2} \sigma a \left(\theta_0 \frac{1}{3} + \theta_{tw} \frac{1}{4} + \theta_0 \frac{\mu^2}{2} + \theta_{tw} \frac{\mu^2}{2} \frac{1}{2} - \lambda \frac{1}{2} \right) \quad (2.58)$$

Thrust coefficient is found as follows:

$$C_T = \sigma a \left(\theta_0 \frac{1}{6} + \theta_{tw} \frac{1}{8} + \theta_0 \frac{\mu^2}{4} + \theta_{tw} \frac{\mu^2}{8} - \frac{\lambda}{4} \right)$$

$$C_T = \sigma a \left(\left(\frac{1}{6} + \frac{1}{4} \mu^2 \right) \theta_0 + (1 + \mu^2) \frac{\theta_{tw}}{8} - \frac{1}{4} \lambda \right) \quad (2.59)$$

Thrust force is calculated by using the thrust force coefficient found above.

$$T = C_T \rho A (\Omega R)^2 \quad (2.60)$$

In forward flight, the following expression is obtained for the thrust force:

$$T = \sigma a \left\{ \left(\frac{1}{6} + \frac{1}{4} \mu^2 \right) \theta_0 + (1 + \mu^2) \frac{\theta_{tw}}{8} - \frac{1}{4} \lambda \right\} \rho A (\Omega R)^2 \quad (2.61)$$

When Equation 2.41 and 2.42 are inserted into the thrust expression (Equation 2.61), the following formulation is formed:

$$T = \sigma a \left\{ \left(\frac{1}{6} + \frac{1}{4} \left(\frac{V \cos \alpha}{\Omega R} \right)^2 \right) \theta_0 + \left(1 + \left(\frac{V \cos \alpha}{\Omega R} \right)^2 \right) \frac{\theta_{tw}}{8} - \frac{1}{4} \left(\frac{(v_i - \dot{z})}{\Omega R} \right) \right\} \rho A (\Omega R)^2 \quad (2.62)$$

Arranging the terms in the above equation allows us to write it as follows:

$$T = \Omega^2 \left(\frac{1}{6} \rho A \sigma a \theta_0 R^2 + \frac{1}{8} \sigma a \rho A \theta_{tw} R^2 \right) + (V \cos \alpha)^2 \left(\frac{1}{4} \rho A \sigma a \theta_0 + \frac{1}{8} \sigma a \rho A \theta_{tw} \right) + (\Omega v_i) \left(-\frac{1}{4} \sigma a \rho A R \right) + (\Omega \dot{z}) \left(\frac{1}{4} \rho A \sigma a R \right) \quad (2.63)$$

$$T = t_1 \Omega^2 + t_2 (V \cos \alpha)^2 + t_3 \Omega (v_i + V \sin \alpha) \quad (2.64)$$

In the equation 2.64 t_1, t_2 , and t_3 are constants which depend on rotor geometry and density of air.

Hub force is the resultant in-plane force acting on the blade element [Figure 2.6]. It is an integral of the rotor force through one rotation, which happens to be in the direction of free stream velocity [Figure 2.5].

Total horizontal forces acting on the blade section is expressed as follows [3, 19]:

$$\Delta F_H = dL \sin \phi + dD \cos \phi \quad (2.65)$$

Hub force is the sinus azimuth angle component of the resultant horizontal forces:

$$dH = \Delta F_H \sin \Psi \quad (2.66)$$

When ΔF_H is written by using the local lift and drag expressions, the following equation is formed:

$$\Delta F_H = \left(\frac{1}{2} \rho \left(\sqrt{U_T^2 + U_P^2} \right)^2 C_l \bar{c} dy \frac{U_P}{\left(\sqrt{U_T^2 + U_P^2} \right)} + \frac{1}{2} \rho \left(\sqrt{U_T^2 + U_P^2} \right)^2 \bar{C}_d \bar{c} dy \frac{U_T}{\left(\sqrt{U_T^2 + U_P^2} \right)} \right) \quad (2.67)$$

$$dH = \frac{1}{2} \rho \left(\sqrt{U_T^2 + U_P^2} \right) \bar{c} dy (C_l U_P + \bar{C}_d U_T) \sin \Psi \quad (2.68)$$

$$= \frac{1}{2} \rho \left(\sqrt{\left(\Omega R \left(\frac{y}{R} + \mu \sin \Psi \right) \right)^2 + (\Omega R \lambda)^2} \right) \bar{c} dy \left(C_l \Omega R \lambda + \bar{C}_d \Omega R \left(\frac{y}{R} + \mu \sin \Psi \right) \right) \sin \Psi \quad (2.69)$$

Hub force coefficient dC_H for one blade is formulated as:

$$\begin{aligned}
& \frac{\frac{1}{2}\rho \left(\sqrt{\left(\Omega R \left(\frac{y}{R} + \mu \sin \Psi \right) \right)^2 + (\Omega R \lambda)^2} \right) \bar{c} dy \left(C_l \Omega R \lambda + \bar{C}_d \Omega R \left(\frac{y}{R} + \mu \sin \Psi \right) \right) \sin \Psi}{\rho A (\Omega R)^2} \\
& = \frac{\frac{1}{2}\rho \left(\sqrt{\left(\Omega R \left(\frac{y}{R} + \mu \sin \Psi \right) \right)^2 + (\Omega R \lambda)^2} \right) \bar{c} dy \left(C_l \Omega R \lambda + \bar{C}_d \Omega R \left(\frac{y}{R} + \mu \sin \Psi \right) \right) \sin \Psi}{\rho \pi R^2 (\Omega R)^2} \quad (2.70)
\end{aligned}$$

For N blades, the above equation is multiplied by N as follows:

$$\frac{\frac{N}{2}\rho \left(\sqrt{\left(\Omega R \left(\frac{y}{R} + \mu \sin \Psi \right) \right)^2 + (\Omega R \lambda)^2} \right) \bar{c} dy \left(C_l \Omega R \lambda + \bar{C}_d \Omega R \left(\frac{y}{R} + \mu \sin \Psi \right) \right) \sin \Psi}{\rho \pi R^2 (\Omega R)^2} \quad (2.71)$$

$$dC_H = \frac{1}{2} \frac{N \bar{c}}{\pi R} (r + \mu \sin \Psi)^2 \left(C_l \frac{\Omega R \lambda}{\Omega R (r + \mu \sin \Psi)} + \bar{C}_d \right) \sin \Psi dr \quad (2.72)$$

$$\begin{aligned}
dC_H = \frac{1}{2} \sigma (r + \mu \sin \Psi)^2 & \left(a \left(\theta_0 + r \theta_{tw} - \frac{\lambda}{(r + \mu \sin \Psi)} \right) \frac{\lambda}{(r + \mu \sin \Psi)} \right. \\
& \left. + \bar{C}_d \right) \sin \Psi dr \quad (2.73)
\end{aligned}$$

$$\begin{aligned}
C_H = \frac{1}{2} \sigma \int_0^1 & \left(\frac{1}{2\pi} \int_0^{2\pi} (r + \mu \sin \Psi)^2 \left(a \left(\theta_0 + r \theta_{tw} \right. \right. \right. \\
& \left. \left. - \frac{\lambda}{(r + \mu \sin \Psi)} \right) \frac{\lambda}{(r + \mu \sin \Psi)} + \bar{C}_d \right) \sin \Psi d\Psi \Big) dr \quad (2.74)
\end{aligned}$$

The integral w.r.t. azimuth angle is as:

$$\begin{aligned}
\frac{1}{2\pi} \int_0^{2\pi} & (r + \mu \sin \Psi)^2 \left(a \left(\theta_0 + r \theta_{tw} - \frac{\lambda}{(r + \mu \sin \Psi)} \right) \frac{\lambda}{(r + \mu \sin \Psi)} \right. \\
& \left. + \bar{C}_d \right) \sin \Psi d\Psi \quad (2.75)
\end{aligned}$$

$$\begin{aligned}
& \frac{1}{2\pi} \int_0^{2\pi} (r^2 \sin \Psi + \mu^2 \sin^3 \Psi + 2r\mu \sin^2 \Psi) \overline{C_d} d\Psi \\
& + \frac{1}{4\pi} \sigma \int_0^{2\pi} (r\lambda a \sin \Psi \theta_0 + \mu\lambda a \theta_0 \sin^2 \Psi) d\Psi \\
& + \frac{1}{2\pi} \int_0^{2\pi} (r\lambda a r \sin \Psi \theta_{tw} + \mu\lambda a r \theta_{tw} \sin^2 \Psi) d\Psi \\
& - \frac{1}{4\pi} \sigma \int_0^{2\pi} (\lambda^2 a \sin \Psi) d\Psi
\end{aligned} \tag{2.76}$$

$$= \frac{1}{2\pi} 2\pi \overline{C_d} \mu + \frac{1}{4\pi} \sigma \pi \mu \lambda a \theta_0 + \frac{1}{4\pi} \sigma \pi \mu \lambda a r \theta_{tw} \tag{2.77}$$

$$= \frac{1}{2} (2r \overline{C_d} \mu + \mu \lambda a \theta_0 + \mu \lambda r \theta_{tw}) \tag{2.78}$$

When the result of the first part is inserted into the second part which is the integral w.r.t. r , the following integral is formed:

$$C_H = \frac{1}{2} \sigma \int_0^1 \frac{1}{2} (2r \overline{C_d} \mu + \mu \lambda a \theta_0 + \mu \lambda r \theta_{tw}) dr \tag{2.79}$$

where r varies from zero to one.

$$C_H = \frac{\sigma}{4} \left(\overline{C_d} \mu + \mu \lambda a \theta_0 + \frac{\mu \lambda a \theta_{tw}}{2} \right) \tag{2.80}$$

$$C_H = \sigma a \left(\overline{C_d} \mu \frac{1}{4a} + \frac{1}{4} \mu \lambda \theta_0 + \frac{1}{8} \mu \lambda \theta_{tw} \right) \tag{2.81}$$

The blade element theory provides the following expression for hub force coefficient.

$$\frac{C_H}{\sigma a} = \frac{1}{4a} \mu \overline{C_d} + \frac{1}{4} \lambda \mu \left(\theta_0 + \frac{\theta_{tw}}{2} \right) \tag{2.82}$$

Equations for hub force are summarized below.

$$H = C_H \rho A (\Omega R)^2 \quad (2.83)$$

$$H = \sigma a \left\{ \frac{1}{4a} \mu \overline{C_d} + \frac{1}{4} \lambda \mu \left(\theta_0 + \frac{\theta_{tw}}{2} \right) \right\} \rho A (\Omega R)^2 \quad (2.84)$$

$$H = \sigma a \left\{ \frac{1}{4a} \left(\frac{V \cos \alpha}{\Omega R} \right) \overline{C_d} + \frac{1}{4} \left(\frac{(v_i - \dot{z})}{\Omega R} \right) \frac{V \cos \alpha}{\Omega R} \left(\theta_0 + \frac{\theta_{tw}}{2} \right) \right\} \rho A (\Omega R)^2 \quad (2.85)$$

$$H = (\Omega V \cos \alpha) \left(\frac{1}{4} \rho A \sigma \overline{C_d} R \right) + (V \cos \alpha v_i) \left(\frac{1}{4} \rho A \sigma a \left(\theta_0 + \frac{\theta_{tw}}{2} \right) \right) + (V \sin \alpha V \cos \alpha) \left(\frac{1}{4} \sigma a \rho A \left(\theta_0 + \frac{\theta_{tw}}{2} \right) \right) \quad (2.86)$$

$$H = (\Omega V \cos \alpha) \left(\frac{1}{4} \rho A \sigma \overline{C_d} R \right) + V \cos \alpha (v_i + V \sin \alpha) \left(\frac{1}{4} \rho A \sigma a \left(\theta_0 + \frac{\theta_{tw}}{2} \right) \right) \quad (2.87)$$

$$H = h_1 (\Omega V \cos \alpha) + h_2 V \cos \alpha (V \sin \alpha + v_i) \quad (2.88)$$

In equation (2.88), h_1 and h_2 are constants which depend on rotor geometry and density of air.

Side force is the cosine azimuth angle component of resultant horizontal forces [3, 19]:

$$dy = \Delta F_H \cos \Psi \quad (2.89)$$

$$dy = (dL \sin \phi + dD \cos \phi) \cos \Psi \quad (2.90)$$

By using the small angle approximation for ϕ , the following relation is obtained:

$$dy = \left(dL \frac{U_P}{U_T} + dD \right) \cos \Psi \quad (2.91)$$

$$dC_y = \frac{dy}{\rho A (\Omega R)^2} = \frac{\left(\frac{1}{2} \rho U_T^2 C_l \bar{c} dy \frac{U_P}{U_T} + \frac{1}{2} \rho U_T^2 \overline{C_d} \bar{c} dy \right) \cos \Psi}{\rho \pi R^2 (\Omega R)^2} \quad (2.92)$$

For N blades, the above equation is multiplied by N as follows:

$$dC_y = N \times \frac{\left(\frac{1}{2} \rho U_T^2 C_l \bar{c} dy \frac{U_P}{U_T} + \frac{1}{2} \rho U_T^2 \overline{C_d} \bar{c} dy \right) \cos \Psi}{\rho \pi R^2 (\Omega R)^2} \quad (2.93)$$

$$\begin{aligned}
dC_y &= N \times \frac{\frac{1}{2} \rho U_T^2 \bar{c} R dr \left(C_l \frac{U_p}{U_T} + \bar{C}_d \right) \cos \Psi}{\rho \pi R^2 (\Omega R)^2} \\
dC_y &= \frac{1}{2} \frac{N \bar{c}}{\pi R} (r + \mu \sin \Psi)^2 \left(C_l \frac{\Omega R \lambda}{\Omega R (r + \mu \sin \Psi)} + \bar{C}_d \right) dr \cos \Psi \\
dC_y &= \frac{1}{2} \sigma (r + \mu \sin \Psi)^2 \left(a \left(\theta_0 + r \theta_{tw} \right. \right. \\
&\quad \left. \left. - \frac{\lambda}{(r + \mu \sin \Psi)} \right) \frac{\lambda}{(r + \mu \sin \Psi)} + \bar{C}_d \right) \cos \Psi dr \quad (2.94) \\
C_y &= \int_0^1 \left(\frac{1}{2\pi} \int_0^{2\pi} \frac{1}{2} \sigma (r + \mu \sin \Psi)^2 \left(a \left(\theta_0 + r \theta_{tw} \right. \right. \right. \\
&\quad \left. \left. - \frac{\lambda}{(r + \mu \sin \Psi)} \right) \frac{\lambda}{(r + \mu \sin \Psi)} + \bar{C}_d \right) \cos \Psi d\Psi \Big) dr \quad (2.95)
\end{aligned}$$

The first part of the integral in Equation 2.95, which is w.r.t. the azimuth angle, is as follows:

$$\begin{aligned}
&\frac{1}{2\pi} \int_0^{2\pi} \frac{1}{2} \sigma (r + \mu \sin \Psi)^2 \left(a \left(\theta_0 + r \theta_{tw} \right. \right. \\
&\quad \left. \left. - \frac{\lambda}{(r + \mu \sin \Psi)} \right) \frac{\lambda}{(r + \mu \sin \Psi)} + \bar{C}_d \right) \cos \Psi d\Psi \\
&= \frac{1}{4\pi} \sigma \bar{C}_d \int_0^{2\pi} \{ r^2 \cos \Psi + \mu^2 \sin^2 \Psi \cos \Psi + 2r\mu \sin \Psi \cos \Psi \} d\Psi \\
&+ \frac{1}{4\pi} \sigma \int_0^{2\pi} \{ r\lambda a \theta_0 \cos \Psi + \mu a \lambda \theta_0 \cos \Psi \sin \Psi + r^2 a \lambda \theta_{tw} \cos \Psi \\
&\quad + a\mu\lambda r \theta_{tw} \sin \Psi \cos \Psi - \lambda^2 a \cos \Psi \} d\Psi = 0 \quad (2.96)
\end{aligned}$$

$$\int_0^1 0 dr = 0 \quad (2.97)$$

$$C_y = 0 \quad (2.98)$$

$$y = 0 \quad (2.99)$$

Rotor torque, which can be called as drag moment, is the torque in the rotor shaft. It is found by integrating the horizontal aerodynamic forces on each rotor section multiplied with a moment arm equal to the radius of that section. Rotor torque by using the assumptions is written as follows [3, 19]:

$$dQ = \Delta F_H y$$

$$dQ = (dL \sin \phi + dD \cos \phi) y = (\phi dL + dD) y \quad (2.100)$$

$$dC_Q = \frac{dQ}{\rho A (\Omega R)^2 R} = \frac{\left(\frac{1}{2} \rho U_T^2 C_l \bar{c} \Delta y \frac{U_p}{U_T} + \frac{1}{2} \rho U_T^2 \bar{C}_d \bar{c} dy \right) y}{\rho \pi R^2 (\Omega R)^2 R}$$

$$dC_Q = N \times \frac{\frac{1}{2} \rho (\Omega R)^2 (r + \mu \sin \Psi)^2 \bar{c} R dr \left(C_l \frac{U_p}{U_T} + \bar{C}_d \right) y}{\rho \pi R^2 (\Omega R)^2} \quad (2.101)$$

For N blades, the following relation is obtained:

$$dC_Q = \frac{1}{2} \frac{N \bar{c}}{\pi R} (r + \mu \sin \Psi)^2 \left(C_l \frac{\Omega R \lambda}{\Omega R (r + \mu \sin \Psi)} + \bar{C}_d \right) r dr$$

$$dC_Q = \frac{1}{2} \sigma (r + \mu \sin \Psi)^2 \left(a \left(\theta_0 + r \theta_{tw} - \frac{\lambda}{(r + \mu \sin \Psi)} \right) \frac{\lambda}{(r + \mu \sin \Psi)} + \bar{C}_d \right) r dr \quad (2.102)$$

$$C_Q = \int_0^1 \left(\frac{1}{2\pi} \int_0^{2\pi} \frac{1}{2} \sigma (r + \mu \sin \Psi)^2 \left(a \left(\theta_0 + r \theta_{tw} - \frac{\lambda}{(r + \mu \sin \Psi)} \right) \frac{\lambda}{(r + \mu \sin \Psi)} + \bar{C}_d \right) r d\Psi \right) dr \quad (2.103)$$

The first part of the integral of Equation 2.103 is w.r.t. the azimuth angle, and it is as follows:

$$\frac{1}{2\pi} \int_0^{2\pi} \frac{1}{2} \sigma (r + \mu \sin \Psi)^2 \left(a \left(\theta_0 + r \theta_{tw} - \frac{\lambda}{(r + \mu \sin \Psi)} \right) \frac{\lambda}{(r + \mu \sin \Psi)} + \bar{C}_d \right) r d\Psi \quad (2.104)$$

$$= \frac{1}{4\pi} \sigma \int_0^{2\pi} (r^2 + \mu^2 \sin^2 \Psi + 2r\mu \sin \Psi) \bar{C}_d d\Psi + \frac{1}{4\pi} \sigma \int_0^{2\pi} (r + \mu \sin \Psi) \lambda a \theta_0 d\Psi + \frac{1}{4\pi} \sigma \int_0^{2\pi} (r + \mu \sin \Psi) \lambda a r \theta_{tw} d\Psi -$$

$$\frac{1}{4\pi} \sigma \int_0^{2\pi} a \lambda^2 d\Psi$$

$$= \frac{1}{4\pi} \sigma 2\pi \bar{C}_d r^2 + \frac{1}{4\pi} \sigma \pi \mu^2 \bar{C}_d + \frac{1}{4\pi} \sigma 2\pi a \theta_0 + \frac{1}{4\pi} \sigma^3 2\pi \lambda a \theta_{tw} -$$

$$\frac{1}{4\pi} \sigma 2\pi a \lambda^2$$

$$= \frac{1}{4} \sigma r (2r^2 \overline{C_d} + \mu^2 \overline{C_d} + 2\lambda a \theta_0 + r^2 2\lambda a \theta_{tw} - 2a\lambda^2) \quad (2.105)$$

The result of the first part of the integral is inserted into Equation 2.103:

$$C_Q = \int_0^1 \frac{\sigma}{4} (2r^3 \overline{C_d} + r\mu^2 \overline{C_d} + 2r\lambda a \theta_0 + r^3 2\lambda a \theta_{tw} - 2ra\lambda^2) dr \quad (2.106)$$

$$C_Q = \sigma a \left(\frac{1}{8a} \overline{C_d} + \frac{1}{8a} \overline{C_d} \mu^2 + \frac{1}{4} \lambda \theta_0 + \frac{1}{8} \lambda \theta_{tw} - \frac{1}{4} \lambda^2 \right) \quad (2.107)$$

Rotor torque is found by using rotor torque coefficient (Equation 2.107):

$$Q = C_Q \rho A (\Omega R)^2 R \quad (2.108)$$

$$\frac{C_Q}{\sigma a} = \frac{1}{8a} (1 + \mu^2) \overline{C_d} + \lambda \left(\frac{1}{4} \theta_0 + \frac{1}{8} \theta_{tw} - \frac{1}{4} \lambda \right) \quad (2.109)$$

$$Q = \sigma a \left\{ \frac{1}{8a} (1 + \mu^2) \overline{C_d} + \lambda \left(\frac{1}{4} \theta_0 + \frac{1}{8} \theta_{tw} - \frac{1}{4} \lambda \right) \right\} \rho A (\Omega R)^2 R \quad (2.110)$$

$$Q = \sigma a \left\{ \frac{1}{8a} \left(1 + \left(\frac{V \cos \alpha}{\Omega R} \right)^2 \right) \overline{C_d} + \frac{(v_i - \dot{z})}{\Omega R} \left(\frac{1}{4} \theta_0 + \frac{1}{8} \theta_{tw} - \frac{1}{4} \frac{(v_i - \dot{z})}{\Omega R} \right) \right\} \rho A (\Omega R)^2 R \quad (2.111)$$

$$\begin{aligned} Q = \Omega^2 \left(\frac{1}{8} \rho A \sigma \overline{C_d} R^3 \right) + (V \cos \alpha)^2 \left(\frac{1}{8} \rho A \sigma \overline{C_d} R \right) \\ + (\Omega v_i) \left(\frac{1}{4} \sigma a \rho A \theta_0 R^2 + \frac{1}{8} \rho A \sigma a \theta_{tw} R^2 \right) \\ + (\Omega V \sin \alpha) \left(\frac{1}{4} \sigma a \rho A \theta_0 R^2 + \frac{1}{8} \rho A \sigma a \theta_{tw} R^2 \right) \\ + (v_i + V \sin \alpha)^2 \left(-\frac{1}{4} \sigma a \rho A R \right) \end{aligned} \quad (2.112)$$

$$Q = q_1 \Omega^2 + q_2 (V \cos \alpha)^2 + q_3 \Omega (v_i + V \sin \alpha) + q_4 (v_i + V \sin \alpha)^2 \quad (2.113)$$

In the equation 2.113, q_1 , q_2 , q_3 , and q_4 are constants which depend on rotor geometry and density of air.

As the blade moves horizontally through the air, the advancing blade section has a larger velocity than the retreating one. This causes more lift in the former than the

latter. Rolling moment, which is caused by the lift difference mentioned previously, is an integral over the entire rotor over one complete rotation [3, 19].

$$dR = -\Delta F_v y \sin \Psi \quad (2.114)$$

$$\begin{aligned} dC_R &= -\frac{dR}{\rho A (\Omega R)^2 R} = \frac{\left(\frac{1}{2} \rho U_T^2 C_l \bar{c} dy \sin \Psi\right) y}{\rho \pi R^2 (\Omega R)^2 R} \times N \\ dC_R &= -\frac{N (\Omega R)^2 (r + \mu \sin \Psi)^2 \bar{c} R dr C_l r R \sin \Psi}{2 \pi R^2 (\Omega R)^2 R} \\ dC_R &= -\frac{1}{2} \frac{N \bar{c}}{\pi R} (r + \mu \sin \Psi)^2 C_l \sin \Psi r dr \\ dC_R &= -\int_0^1 \left(\frac{1}{2\pi} \int_0^{2\pi} \frac{1}{2} \sigma (r + \mu \sin \Psi)^2 a \left(\theta_0 + r \theta_{tw} \right. \right. \\ &\quad \left. \left. - \frac{\lambda}{(r + \mu \sin \Psi)} \right) r \sin \Psi d\Psi \right) dr \end{aligned} \quad (2.115)$$

The first part of the integral of Equation 2.115 is w.r.t. azimuth angle:

$$\begin{aligned} &\frac{1}{2\pi} \int_0^{2\pi} \frac{1}{2} \sigma (r + \mu \sin \Psi)^2 a \left(\theta_0 + r \theta_{tw} \right. \\ &\quad \left. - \frac{\lambda}{(r + \mu \sin \Psi)} \right) \sin \Psi r d\Psi \\ &= \frac{1}{4\pi} \sigma r a \left(\int_0^{2\pi} (r^2 \sin \Psi + \mu^2 \sin^3 \Psi + 2r\mu \sin^2 \Psi) (\theta_0 + \right. \\ &\quad \left. r \theta_{tw}) d\Psi - \int_0^{2\pi} \lambda r \sin \Psi d\Psi - \int_0^{2\pi} \lambda \mu \sin^2 \Psi d\Psi \right) \\ &= \frac{1}{4} \sigma r a (2r\mu \theta_0 + 2r^2 \mu \theta_{tw} - \mu \lambda) \end{aligned} \quad (2.116)$$

When the first part of the integral is inserted into Equation 2.115, the following relation is obtained:

$$C_R = -\frac{1}{4} \sigma a \int_0^1 (2r^2 \mu \theta_0 + 2r^3 \mu \theta_{tw} - r \mu \lambda) dr \quad (2.117)$$

$$C_R = -\sigma a \left(\frac{1}{6} \mu \theta_0 + \frac{1}{8} \mu \theta_{tw} - \frac{1}{8} \mu \lambda \right) \quad (2.118)$$

Rolling moment is as follows:

$$R = C_R \rho A (\Omega R)^2 R \quad (2.119)$$

$$R = \sigma a \left\{ -\mu \left(\frac{1}{6} \theta_0 + \frac{1}{8} \theta_{tw} - \frac{1}{8} \lambda \right) \right\} \rho A (\Omega R)^2 R \quad (2.120)$$

$$R = \sigma a \left\{ - \left(\frac{V \cos \alpha}{\Omega R} \right) \left(\frac{1}{6} \theta_0 + \frac{1}{8} \theta_{tw} - \frac{1}{8} \frac{(v_i - \dot{z})}{\Omega R} \right) \right\} \rho A (\Omega R)^2 R \quad (2.121)$$

$$\begin{aligned} R = (\Omega V \cos \alpha) & \left(- \frac{1}{6} \sigma a \rho A \theta_0 R^2 - \frac{1}{8} \rho A \sigma a \theta_{tw} R^2 \right) \\ & + (V \cos \alpha v_i) \left(\frac{1}{8} \sigma a \rho A R \right) \\ & + (V \cos \alpha V \sin \alpha) \left(\frac{1}{8} \sigma a \rho A R \right) \end{aligned} \quad (2.122)$$

$$R = r_1 (\Omega V \cos \alpha) + r_2 (V \cos \alpha) (v_i + V \sin \alpha) \quad (2.123)$$

In equation 2.123, r_1 and r_2 are constants which depend on rotor geometry and density of air.

Pitching moment is formulated as [3, 19]:

$$dP = -\Delta F_V y \cos \Psi \quad (2.124)$$

$$\begin{aligned} dC_P &= \frac{dP}{\rho A (\Omega R)^2 R} = - \frac{\left(\frac{1}{2} \rho U_T^2 C_l \bar{c} dy \cos \Psi \right) y}{\rho \pi R^2 (\Omega R)^2 R} \times N \\ &= - \frac{N (\Omega R)^2 (r + \mu \sin \Psi)^2 \bar{c} R dr C_l r R \cos \Psi}{2 \pi R^2 (\Omega R)^2 R} \end{aligned}$$

$$dC_P = - \frac{1}{2} \frac{N \bar{c}}{\pi R} (r + \mu \sin \Psi)^2 C_l \cos \Psi r dr \quad (2.125)$$

$$dC_P = - \int_0^1 \left(\frac{1}{2\pi} \int_0^{2\pi} \frac{1}{2} \sigma (r + \mu \sin \Psi)^2 C_l \cos \Psi r d\Psi \right) dr \quad (2.126)$$

The first part of the integral w.r.t. azimuth angle is:

$$\begin{aligned} & \frac{1}{2\pi} \int_0^{2\pi} \frac{1}{2} \sigma (r + \mu \sin \Psi)^2 a \left(\theta_0 + r \theta_{tw} \right. \\ & \quad \left. - \frac{\lambda}{(r + \mu \sin \Psi)} \right) \cos \Psi r d\Psi \\ &= \frac{1}{4\pi} \sigma r a \left(\int_0^{2\pi} (r^2 \cos \Psi + \mu^2 \sin^2 \Psi \cos \Psi \right. \\ & \quad \left. + 2r\mu \sin \Psi \cos \Psi) (\theta_0 + r \theta_{tw}) d\Psi \right. \\ & \quad \left. - \int_0^{2\pi} \lambda r \cos \Psi d\Psi - \int_0^{2\pi} \lambda \mu \sin \Psi \cos \Psi d\Psi \right) \end{aligned} \quad (2.127)$$

$$= 0$$

The second part of the integral is:

$$\int_0^1 0 dr = 0 \quad (2.128)$$

Pitching moment coefficient is found as zero as a result of integrations.

$$C_p = 0 \quad (2.129)$$

Table 2.3: Forces and moments expressions according to blade element theory

Thrust force	$T = \Omega^2 \left(\frac{1}{6} \rho A \sigma a \theta_0 R^2 + \frac{1}{8} \sigma a \rho A \theta_{tw} R^2 \right) +$ $(V \cos \alpha)^2 \left(\frac{1}{4} \rho A \sigma a \theta_0 + \frac{1}{8} \sigma a \rho A \theta_{tw} \right) +$ $\Omega (V \sin \alpha + v_i) \left(-\frac{1}{4} \sigma a \rho A R \right)$	$T = t_1 \Omega^2 +$ $t_2 (V \cos \alpha)^2 +$ $t_3 \Omega (v_i + V \sin \alpha)$
Hub force	$H = (\Omega V \cos \alpha) \left(\frac{1}{4} \rho A \sigma \overline{C_d} R \right) + V \cos \alpha (v_i +$ $V \sin \alpha) \left(\frac{1}{4} \rho A \sigma a \left(\theta_0 + \frac{\theta_{tw}}{2} \right) \right)$	H $= h_1 (\Omega V \cos \alpha)$ $+ h_2 V \cos \alpha (v_i$ $+ V \sin \alpha)$
Side force	0	0
Rotor torque	$Q =$ $\Omega^2 \left(\frac{1}{8} \rho A \sigma \overline{C_d} R^3 \right) + (V \cos \alpha)^2 \left(\frac{1}{8} \rho A \sigma R \overline{C_d} \right) +$ $(\Omega v_i) \left(\frac{1}{4} \sigma a \rho A \theta_0 R^2 + \frac{1}{8} \rho A \sigma a \theta_{tw} R^2 \right) +$ $(\Omega V \sin \alpha) \left(\frac{1}{4} \sigma a \rho A \theta_0 R^2 + \frac{1}{8} \rho A \sigma a \theta_{tw} R^2 \right) +$ $(v_i + V \sin \alpha)^2 \left(-\frac{1}{4} \sigma a \rho A R \right)$	$Q = q_1 \Omega^2 +$ $q_2 (V \cos \alpha)^2 +$ $q_3 \Omega (v_i + V \sin \alpha) +$ $q_4 (v_i + V \sin \alpha)^2$
Rolling moment	$R = (\Omega V \cos \alpha) \left(-\frac{1}{6} \sigma a \rho A \theta_0 R^2 -$ $\frac{1}{8} \rho A \sigma a \theta_{tw} R^2 \right) + (V \cos \alpha v_i) \left(\frac{1}{8} \sigma a \rho A R \right) +$ $(V \cos \alpha V \sin \alpha) \left(\frac{1}{8} \sigma a \rho A R \right)$	$R = r_1 (\Omega V \cos \alpha) +$ $r_2 V \cos \alpha (v_i +$ $V \sin \alpha)$
Pitching moment	0	0

Constants in Table 2.3 that depend on rotor geometry and the density of air are denoted as $t_1, t_2, t_3, h_1, h_2, r_1, r_2, q_1, q_2, q_3$, and q_4 in order to be experimentally predicted by method of least squares.

The parameters of the equations in Table 2.3 depend on geometric properties of the blade and the density of air, and hence can be calculated if the necessary information is available. However, although all the necessary information is available, it is still not a reliable approach because there are many assumptions in blade element theory. In this study, not all the rotor geometry parameters are available for the quadrotor used, and because of the assumptions of blade element theory, the aerodynamic model parameters are identified experimentally. Rotor forces and moments (left hand sides of the equations in Table 2.3) are measured in a wind tunnel at various V , α , and Ω values that appear on the right hand sides. Then the unknown t_i, h_i, q_i , and r_i coefficients are found to match the two sides of the equations as closely as possible.

CHAPTER 3

PARAMETER ESTIMATION AND SYSTEM IDENTIFICATION

The difficult part of simulating an air vehicle is finding external forces and moments acting on the vehicle. In this study, rotor forces and moments which are function of rotor speed and flight condition are determined through the parameter estimation.

3.1. Experiments

In order to experimentally identify model parameters, the quadrotor UAV shown in Figure 3.1, is mounted on a balance system that can measure forces and moments in all three axes. The tests are performed in METU Aerospace Engineering wind tunnel shown in Figure 3.2. It is a low speed suction type wind tunnel, which includes a 2D contraction section with an area ratio of 1:5, and it is powered by a 45 kW speed-controlled electrical motor.



Figure 3.1: Quadrotor UAV



Figure 3.2: Wind tunnel

The test setup used in the experiments is presented in Figure 3.3. It consists of a velocity sensor [Figure 3.4] which has a 0-30 m/s range to measure free stream velocity.



Figure 3.3: Test setup

The setup includes a load cell [Figure 3.5] to measure forces and moments on the quadrotor. The mechanical structure seen in Figure 3.3 to mount the load cell and quadrotor in the test section at a desired position and orientation was designed and manufactured for this study. The vehicle and the load cell were installed on this mechanical part. Then the whole system was mounted into the wind tunnel in order to measure free stream velocity, and forces and moments simultaneously.



Figure 3.4: Velocity sensor



Figure 3.5: Load cell

The set-up also contains an optical *RPM* sensor [Figure 3.6] to measure angular velocity of the rotor. The electronic part is connected to the data acquisition device [Figure 3.7] which sends the experimental information from the load cell and velocity sensor to the computer. Single rotor and single motor were run during the experiments. Experiments are performed with the front rotor of the quadrotor. Steady state values at various conditions were used for parameter identification. Data was collected at a rate of 5000 samples per second and averaged for processing.



Figure 3.6: *RPM* sensor



Figure 3.7: Data acquisition device

In the test setup, the load cell is installed between the quadrotor and the mounting structure. Hence, the aerodynamic loads acting on the mount are not measured by the load cell. Forces and moments are measured for a large number of test cases that are combinations of various rotor speeds, free stream velocities, and angles of attack. Six different free stream velocities between 0 and 11.07 *m/s* are scanned at eight

different rotor speeds between 2000 *RPM* and 7000 *RPM*, and five different angles of attack between 0° and 90°, yielding a total of 500 test cases. Each test is repeated twice, once with the rotor rotating at a certain speed, and one without the rotor installed. Forces and moments measured without the rotor gives the loads acting on the body. These values are subtracted from the values measured with the rotor to obtain the net rotor forces and moments. Because the load cell is mounted on the C.o.G. of the quadrotor, the measured moments are not the moments on the rotor. The net moments is calculated by subtracting cross product of length l and measured forces from the measured moments.

3.2. Parameter Estimation Method Used in the Study

In this study, there are more equations than the unknowns. For this reason, the method of least squares is chosen for parameter estimation part. Since the parameters appear linear in the equations [Table 2.3], method of least squares is used to predict the unknowns. To understand the concept of the method of least squares, simple and multiple linear regressions are mentioned based on the study of Montgomery [22].

3.2.1. Simple Linear Regression

In the case of simple linear regression, there is one dependent and one explanatory variable. The following equation describes the simple linear regression model:

$$y = \beta_0 + \beta_1 x + \epsilon \quad (3.1)$$

where y is the dependent variable, x is the independent/explanatory variable, β_0 is intercept, β_1 is slope, and ϵ is the random error term with mean zero and variance σ^2 . Karl Gauss put forward that the sum of the squares of the vertical deviations presented in Figure 3-8 is minimized to predict the parameters β_0 and β_1 in Equation 3.1 [22]. This criterion is called the method of least squares which estimates the regression coefficients.

If there are n observations, then Equation 3.1 is formed as follows:

$$y_i = \beta_0 + \beta_1 x_i + \epsilon_i \quad (3.2)$$

where $i = 1, 2, \dots, n$.

$$L = \sum_{i=1}^n \epsilon_i^2 = \sum_{i=1}^n (y_i - \beta_0 - \beta_1 x_i)^2 \quad (3.3)$$

The vertical deviations of the observations from the estimated regression line are shown in Figure 3.8:

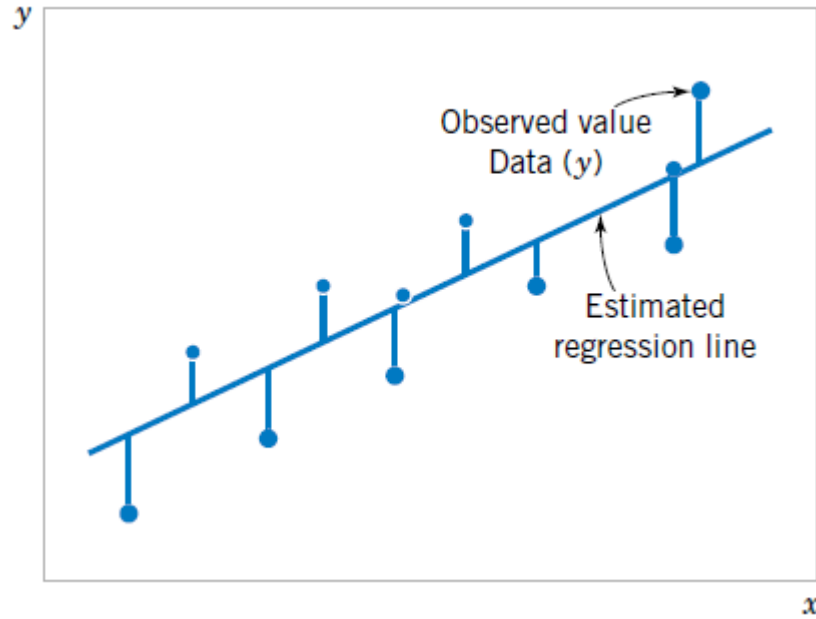


Figure 3.8: Deviations of the data from the estimated regression model [22]

According to the method of least squares, the least squares estimators of β_0 and β_1 denoted as $\widehat{\beta}_0$ and $\widehat{\beta}_1$ must satisfy the following relations:

$$\frac{\partial L}{\partial \beta_0}(\widehat{\beta}_0, \widehat{\beta}_1) = -2 \sum_{i=1}^n (y_i - \beta_0 - \beta_1 x_i) = 0 \quad (3.4)$$

$$\frac{\partial L}{\partial \beta_1}(\widehat{\beta}_0, \widehat{\beta}_1) = -2 \sum_{i=1}^n (y_i - \beta_0 - \beta_1 x_i) x_i = 0 \quad (3.5)$$

The circumflex (^) indicates estimated values. Estimated regression model is shown as following equation:

$$\widehat{y} = \widehat{\beta}_0 + \widehat{\beta}_1 x \quad (3.6)$$

Each pair of observations should satisfy the following relation:

$$y_i = \widehat{\beta}_0 + \widehat{\beta}_1 x_i + e_i \quad (3.7)$$

3.2.2. Multiple Linear Regression

If there are two or more independent variables in the model, the regression is called a multiple regression model. Any regression model which is linear in parameters is a linear regression model. Hence, the following equation is called a multiple linear regression model with k independent variables [22].

$$y_i = \beta_0 + \beta_1 x_{i1} + \beta_2 x_{i2} + \dots + \beta_k x_{ik} + \epsilon_i \quad (3.8)$$

The method of least squares can be used to estimate the regression coefficients in the multiple regression model. In this study, the model is multiple linear regression because there are more than one independent variable to predict, and the coefficients appear linear [Table 2.3]. In order to determine the unknowns in the equations presented in Table 2.3 first, they are written as matrices. Then, the MATLAB backslash operator (\) is used to find the unknowns t_i , h_i , q_i , and r_i . It is a matrix approach to multiple linear regression, and computes a least square solution for such overdetermined systems.

The geometry behind the operator is explained as follows [22, 27, 28]:

Let

$$y = X\beta + \epsilon \quad (3.9)$$

$$\text{where } y = \begin{bmatrix} y_1 \\ y_2 \\ y_3 \\ \vdots \\ y_n \end{bmatrix}, \beta = \begin{bmatrix} \beta_0 \\ \beta_1 \\ \beta_2 \\ \vdots \\ \beta_k \end{bmatrix}, \text{ and } X = \begin{bmatrix} 1 & x_{11} & x_{12} & \dots & x_{1k} \\ 1 & x_{21} & x_{22} & \dots & x_{2k} \\ 1 & x_{31} & x_{32} & \dots & x_{3k} \\ \vdots & \vdots & \vdots & \ddots & \vdots \\ 1 & x_{n1} & x_{n2} & \dots & x_{nk} \end{bmatrix}$$

k is the number of independent variables, and n is the number of test cases. It is assumed that error term ϵ follows normal (Gaussian) distribution meaning that $E(\epsilon) = 0$ so leading to following relationship at means:

$$\bar{X}\hat{\beta} = \bar{y} \quad (3.10)$$

$$\bar{X}\hat{\beta} - \bar{y} = 0 \quad (3.11)$$

In order to get the solution of $\hat{\beta}$, sum of squared of the error term should be minimized as below:

$$\operatorname{argmin} \|L\| = \operatorname{argmin} \|(X\hat{\beta} - y)^2\| \quad (3.12)$$

$$f(\hat{\beta}) = (X\hat{\beta} - y)^2 = \frac{1}{2} (X\hat{\beta} - y)^T (X\hat{\beta} - y) \quad (3.13)$$

$$f(\hat{\beta}) = \frac{1}{2} (\hat{\beta}^T X^T X \hat{\beta} - \hat{\beta}^T X^T y - y^T X \hat{\beta} + y^T y) \quad (3.14)$$

$$\nabla f(\hat{\beta}) = (X^T X) \hat{\beta} - X^T y = 0 \quad (3.15)$$

$$\hat{\beta} = (X^T X)^{-1} X^T y \quad (3.16)$$

Equation 3.16 is valid for a full rank $(X^T X)$.

In matrix notation, the fitted model is expressed as follows:

$$\hat{y} = X\hat{\beta} \quad (3.17)$$

In this study, while estimating the parameters, the following matrices are generated by using the matrix approach of the method of least squares [22].

$$\begin{bmatrix} T_1 \\ T_2 \\ T_3 \\ \vdots \\ T_n \end{bmatrix} = \begin{bmatrix} \Omega_1^2 & (V_1 \cos \alpha_1)^2 & \Omega_1 (V_1 \sin \alpha_1 + v_{i_1}) \\ \vdots & \vdots & \vdots \\ \Omega_n^2 & (V_n \cos \alpha_n)^2 & \Omega_n (V_n \sin \alpha_n + v_{i_n}) \end{bmatrix} \begin{bmatrix} t_1 \\ t_2 \\ t_3 \end{bmatrix} \quad (3.18)$$

$$T = K_T t \quad (3.19)$$

$$\text{where } K_T = \begin{bmatrix} \Omega_1^2 & (V_1 \cos \alpha_1)^2 & \Omega_1 (V_1 \sin \alpha_1 + v_{i_1}) \\ \vdots & \vdots & \vdots \\ \Omega_n^2 & (V_n \cos \alpha_n)^2 & \Omega_n (V_n \sin \alpha_n + v_{i_n}) \end{bmatrix}, T = \begin{bmatrix} T_1 \\ T_2 \\ T_3 \\ \vdots \\ T_n \end{bmatrix}, t = \begin{bmatrix} t_1 \\ t_2 \\ t_3 \end{bmatrix}$$

That is, the unknowns are calculated by using the following relation which is the underlying geometric explanation of MATLAB backslash operator (\backslash):

$$t = (K_T^T K_T)^{-1} K_T^T T \quad (3.20)$$

Various matrices are created to determine the unknown parameters for hub force, rolling moment, and rotor torque as can be seen below representations:

$$\left[\begin{pmatrix} H_1 \\ H_2 \\ H_3 \\ \vdots \\ H_n \end{pmatrix} \right] = \begin{bmatrix} \Omega_1(V_1 \cos \alpha_1) & V_1 \cos \alpha_1 (V_1 \sin \alpha_1 + v_{i_1}) \\ \vdots & \vdots \\ \Omega_n(V_n \cos \alpha_n) & V_n \cos \alpha_n (V_n \sin \alpha_n + v_{i_n}) \end{bmatrix} \begin{bmatrix} h_1 \\ h_2 \end{bmatrix} \quad (3.21)$$

$$H = K_H h \quad (3.22)$$

where

$$H = \left[\begin{pmatrix} H_1 \\ H_2 \\ H_3 \\ \vdots \\ H_n \end{pmatrix} \right], K_H = \begin{bmatrix} \Omega_1(V_1 \cos \alpha_1) & V_1 \cos \alpha_1 (V_1 \sin \alpha_1 + v_{i_1}) \\ \vdots & \vdots \\ \Omega_n(V_n \cos \alpha_n) & V_n \cos \alpha_n (V_n \sin \alpha_n + v_{i_n}) \end{bmatrix}, h = \begin{bmatrix} h_1 \\ h_2 \end{bmatrix}$$

After generating the matrices for hub force, the parameters (unknowns) are found by using the relation below:

$$h = K_H \backslash H \quad (3.23)$$

$$h = (K_H^T K_H)^{-1} K_H^T H \quad (3.24)$$

Same procedure is followed for rotor torque and rolling moment.

$$\left[\begin{pmatrix} Q_1 \\ Q_2 \\ Q_3 \\ \vdots \\ Q_n \end{pmatrix} \right] = \quad (3.25)$$

$$\begin{bmatrix} \Omega_1^2 & (V_1 \cos \alpha_1)^2 & \Omega_1(V_1 \sin \alpha_1 + v_{i_1}) & (V_1 \sin \alpha_1 + v_{i_1})^2 \\ \vdots & \vdots & \vdots & \vdots \\ \Omega_n^2 & (V_n \cos \alpha_n)^2 & \Omega_n(V_n \sin \alpha_n + v_{i_n}) & (V_n \sin \alpha_n + v_{i_n})^2 \end{bmatrix} \begin{bmatrix} q_1 \\ q_2 \\ q_3 \\ q_3 \end{bmatrix}$$

$$Q = K_Q q \quad (3.26)$$

$$\text{where } Q = \left[\begin{pmatrix} Q_1 \\ Q_2 \\ Q_3 \\ \vdots \\ Q_n \end{pmatrix} \right], q = \begin{bmatrix} q_1 \\ q_2 \\ q_3 \\ q_3 \end{bmatrix}, \text{ and}$$

$$K_Q = \begin{bmatrix} \Omega_1^2 & (V_1 \cos \alpha_1)^2 & \Omega_1(V_1 \sin \alpha_n + v_{i_1}) & (V_1 \sin \alpha_1 + v_{i_1})^2 \\ \vdots & \vdots & \vdots & \vdots \\ \Omega_n^2 & (V_n \cos \alpha_n)^2 & \Omega_n(V_n \sin \alpha_n + v_{i_n}) & (V_n \sin \alpha_n + v_{i_n})^2 \end{bmatrix}$$

$$q = K_Q \backslash Q \quad (3.27)$$

$$q = (K_Q^T K_Q)^{-1} K_Q^T Q \quad (3.28)$$

$$\begin{bmatrix} R_1 \\ R_2 \\ R_3 \\ \vdots \\ R_n \end{bmatrix} = \begin{bmatrix} \Omega_1(V_1 \cos \alpha_1) & V_1 \cos \alpha_1 (V_1 \sin \alpha_1 + v_{i_1}) \\ \vdots & \vdots \\ \Omega_n(V_n \cos \alpha_n) & V_n \cos \alpha_n (V_n \sin \alpha_n + v_{i_n}) \end{bmatrix} \begin{bmatrix} r_1 \\ r_2 \end{bmatrix} \quad (3.29)$$

$$R = K_R r \quad (3.30)$$

$$\text{where } R = \begin{bmatrix} R_1 \\ R_2 \\ R_3 \\ \vdots \\ R_n \end{bmatrix}, K_R = \begin{bmatrix} \Omega_1(V_1 \cos \alpha_1) & V_1 \cos \alpha_n (V_1 \sin \alpha_1 + v_{i_1}) \\ \vdots & \vdots \\ \Omega_n(V_n \cos \alpha_n) & V_n \cos \alpha_n (V_n \sin \alpha_n + v_{i_n}) \end{bmatrix}, r = \begin{bmatrix} r_1 \\ r_2 \end{bmatrix}$$

$$r = K_R \backslash R \quad (3.31)$$

$$r = (K_R^T K_R)^{-1} K_R^T R \quad (3.32)$$

$n = 8, 11, 192$ for hovering, vertical climb, and forward flight, respectively.

3.2.3. The Coefficient of Determination

There are several methods to assess the reliability of the regression. In this study, R^2 and adjusted R^2 are used to identify the reliability of the model. The methods are explained as follows according to the study conducted by Montgomery [22]:

$e_i = y_i - \hat{y}_i$ is called as residuals or offsets. Each residual describes the error between the fit of the model and observation. Therefore, Error Sum of Squares gives information about the unexplained variations in the model, and it is defined as following equation:

$$SS_E = \sum_{i=1}^n (y_i - \hat{y}_i)^2 = \sum_{i=1}^n e_i^2 \quad (3.33)$$

Sum of Squares of Total explains the variation of dependent variable in the model, and it is formulated as follows:

$$SS_T = \sum_{i=0}^n (y_i - \bar{y})^2 \quad (3.34)$$

where \bar{y} is the average value of the observed values and formulated as:

$$\bar{y} = \frac{1}{n} \sum_{i=0}^n y_i \quad (3.35)$$

Regression Sum of Squares is as follows:

$$SS_R = \sum_{i=0}^n (\hat{y}_i - \bar{y})^2 \quad (3.36)$$

SS_T equals to the sum of SS_E and SS_R .

$$SS_T = SS_E + SS_R \quad (3.37)$$

$$\frac{SS_R}{SS_T} = 1 - \frac{SS_E}{SS_T} \quad (3.38)$$

Equation 3.38 is called as R squared (R^2) which is used to identify the reliability of the data. The value of R^2 is between 0 and 1, and as it closes to 1 it means that data fits well. In other words, R squared is a measure that showcases how much the explanatory variable (x) is able to explain the dependent variable (y). If R squared equals to 0.99, it means that the x is able to explain 99% of the changes in y ; and cannot explain the 1% which falls into the error term. The higher the R squared the better x explains the changes in y and then stronger the regression. However, a large value of R^2 does not necessarily imply that the fitted model is a good one. Experimental and model graphs should be scanned to decide whether the estimation is reliable or not. Besides, there is a significant restriction of R^2 . It always increases when a new variable is added. Therefore, it can be difficult to deduce whether the increase of the value of R^2 means a useful thing or not [22]. For this reason, adjusted R^2 can be used to evaluate the reliability of the regression.

Adjusted R^2 is expressed as follows:

$$R_{adj}^2 = 1 - \frac{\left(\frac{SS_E}{n - p}\right)}{\left(\frac{SS_T}{n - 1}\right)} \quad (3.39)$$

where n is the number of observations, and p is the number of coefficients. In the simple linear regression case, p equals to 2 (Equation 3.1).

The analytical equations presented in Chapter 2 are fit to data collected in the tunnel using the least squares fitting algorithm presented in this chapter. Validity of the fits is demonstrated through plots, R^2 , and adjusted R^2 .

CHAPTER 4

RESULTS

4.1. Results by using Blade Element Theory and Method of Least Squares

Test data and induced velocities in hovering flight are shown in Table 4.1:

Table 4.1: Experimental data and calculated induced velocity in hovering flight

Angular velocity of the rotor (<i>RPM</i>)	Thrust (<i>N</i>)	Rotor torque (<i>Nm</i>)	Calculated induced velocity using Eqn. 2.15 (<i>m/s</i>)	Calculated induced velocity using Eqn. 2.15 (<i>m/s</i>) and assumption (Thrust=Weight)
3100	0.7037	0.02256	3.0525	3.9481
3570	0.9504	0.029663	3.5475	3.9481
3900	1.1382	0.039271	3.8822	3.9481
4290	1.3318	0.049785	4.1994	3.9481
4600	1.578	0.055077	4.5711	3.9481
5050	1.9243	0.067832	5.0478	3.9481
5510	2.2352	0.078425	5.4403	3.9481
5820	2.5296	0.091957	5.7875	3.9481
6270	2.9553	0.103921	6.2556	3.9481
6600	3.37	0.117354	6.6801	3.9481
7030	3.9016	0.137868	7.1876	3.9481

Fitted values of thrust force and rotor torque in hovering flight are presented in Table 4.2.

Table 4.2: Fitted values in hovering flight

Angular velocity of the	Thrust fitted with	Rotor torque Fitted with	Thrust fitted ignoring	Rotor torque Fitted ignoring
-------------------------	--------------------	--------------------------	------------------------	------------------------------

rotor (<i>RPM</i>)	induced velocity effect (<i>N</i>)	induced velocity effect (<i>Nm</i>)	induced velocity effect (<i>N</i>)	induced velocity effect (<i>Nm</i>)
3100	0.7035	0.0252	07321	0.0258
3570	0.9504	0.0335	0.9710	0.0342
3900	1.1383	0.0400	1.1588	0.0408
4290	1.3311	0.0484	1.4021	0.0494
4600	1.5781	0.0556	1.6121	0.0568
5050	1.9246	0.0674	1.9429	0.0684
5510	2.2349	0.0796	2.3130	0.0815
5820	2.5298	0.0890	2.5805	0.0909
6270	2.9557	0.1036	2.9950	0.1055
6600	3.3704	0.1178	3.3186	0.1169
7030	3.9011	0.1378	3.7651	0.1326

Relations relevant to hovering flight ignoring the induced velocity and results are given in Table 4.3.

Table 4.3: Parameter estimation results ignoring induced velocity

Relation between thrust force and angular velocity of the rotor	$T = b\Omega^2$
Relation between rotor torque and angular velocity of the rotor	$Q = d\Omega^2$
Thrust coefficient (N/RPM^2)	$b = 7.6184 \times 10^{-8}$
Rotor torque coefficient (Nm/RPM^2)	$d = 2.6839 \times 10^{-9}$

Parameters are found by using the method of least squares. As it can be seen in the Figure 4.1 and 4.2, the experimental and predicted graphs fit well for thrust force and rotor torque in hovering flight. According to the coefficient of determination, the reliability of the predicted coefficients b and d are 99.64% and 99.45%, respectively.

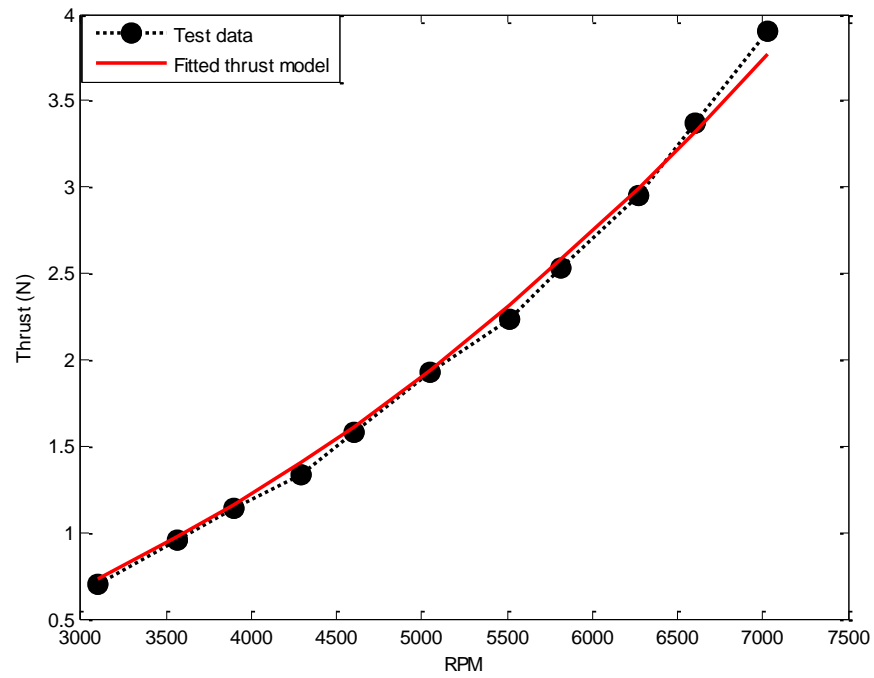


Figure 4.1: Thrust change w.r.t. the angular velocity of the rotor using BET in hovering flight

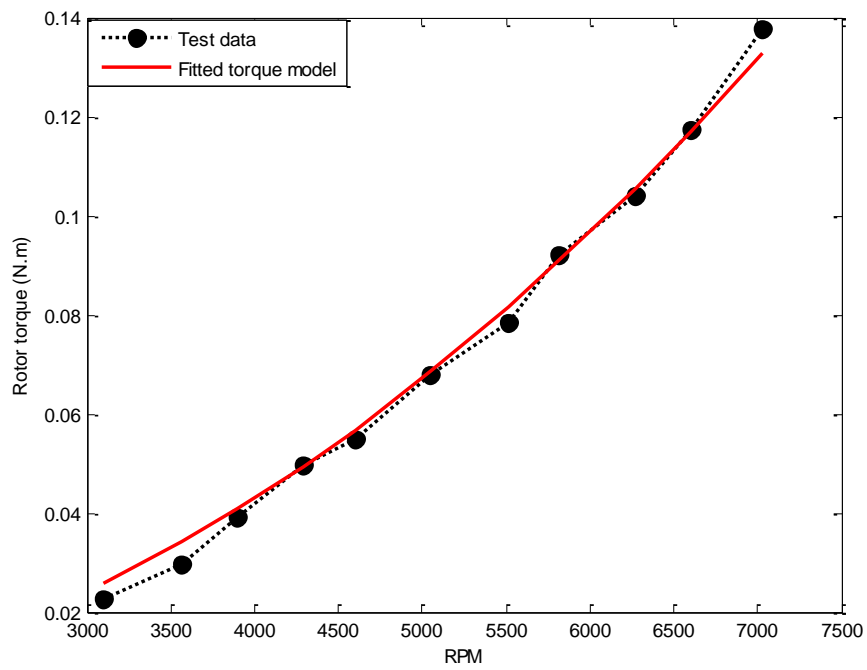


Figure 4.2: Rotor torque change w.r.t. the angular velocity of the rotor using BET in hovering flight

Note that hovering flight in this case refers to the case where the quadrotor is not moving. In an actual hovering flight, rotor thrust forces should balance the weight of the vehicle, which can only be achieved at a particular rotor speed. In this section we do not enforce the force balance equation. In wind tunnel tests weight of the vehicle is carried by the balance system, and hence rotor forces and moments while the vehicle is stationary can be measured at any rotor speed.

Thrust force and rotor torque equation parameters with induced velocity effect using BET, and the results using method of least squares are given in Table 4.4.

Table 4.4: Parameter estimation results including induced velocity using BET

Relation between thrust force and the angular velocity of the rotor	$T = t_1 \Omega^2 + t_3 \Omega v_i$
Relation between rotor torque and the angular velocity of the rotor	$Q = q_1 \Omega^2 + q_3 \Omega v_i + q_4 v_i^2$
Thrust Coefficient	$t_1 = -7.6256 \times 10^{-8} \text{ (N/RPM}^2\text{)}$ $t_3 = 1.5179 \times 10^{-4} \left(\frac{\text{N}}{\text{RPM(m/s)}} \right)$
Rotor torque coefficient	$q_1 = 1.3101 \times 10^{-7} \text{ (Nm/RPM}^2\text{)}$ $q_3 = -2.6020 \times 10^{-4} \left(\frac{\text{Nm}}{\text{RPM(m/s)}} \right)$ $q_4 = 0.131 \text{ (Nm/(m/s)}^2\text{)}$

Induce velocity is calculated by using Equation 2.15, and the relation between induced velocity and angular speed of the rotor is illustrated in Figure 4.3:

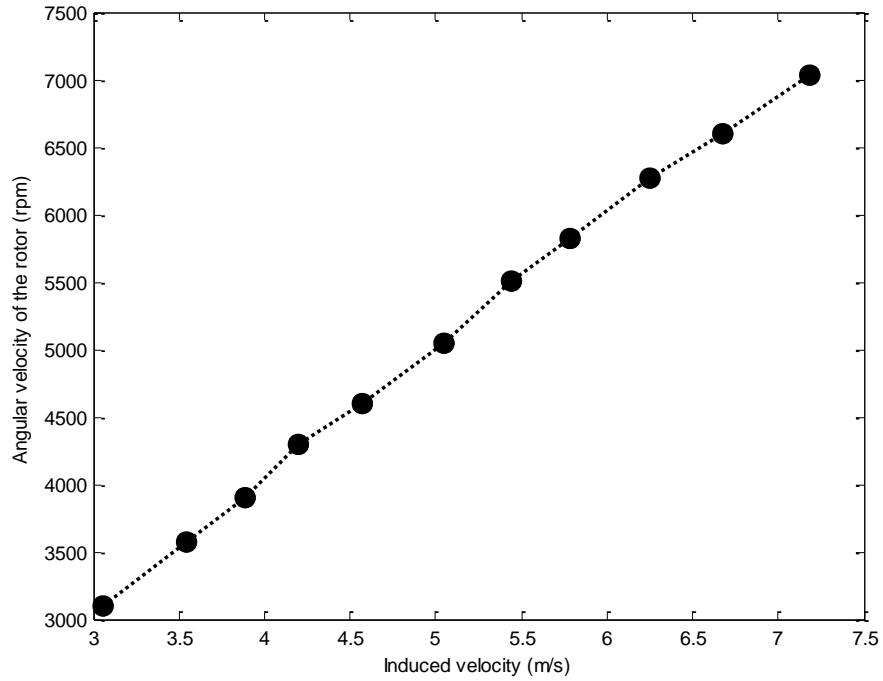


Figure 4.3: Induced velocity w.r.t. angular velocity of rotor in hovering flight [24]

Measured and model predicted thrust and rotor torque values without ignoring the induced velocity are shown in Figure 4.4 and Figure 4.5, respectively.

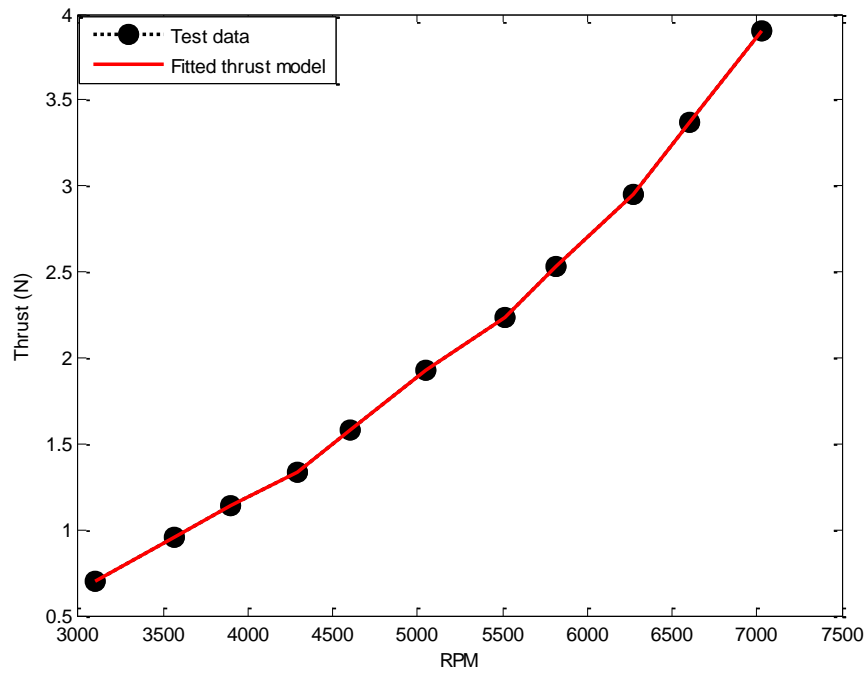


Figure 4.4: Thrust change w.r.t. the angular velocity of the rotor using BET in hovering flight

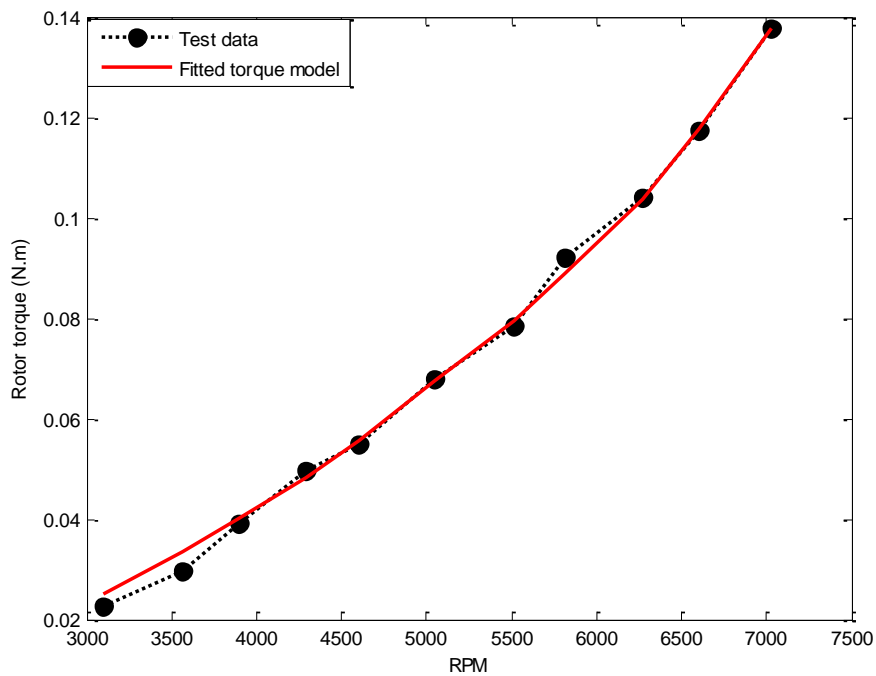


Figure 4.5: Rotor torque change w.r.t. the angular velocity of the rotor using BET in hovering flight

The coefficient of determination is presented in the following table:

Table 4.5: Coefficient of determination in hovering flight using BET

R^2 without induced velocity effect	R^2 with induced velocity effect	Adjusted R^2 with induced velocity effect	Forces/Moments
0.9964	1	0.9959	Thrust Force
0.9945	0.9975	0.9999	Rotor Torque

As it can be seen in Figure 4.4, Figure 4.5, and R^2 results [Table 4.5], adding the induced velocity to the equations, the predicted model in hovering flight fits the experimental values better than ignoring it.

Experimental and fitted results in vertical climb case at 5820 *RPM* are shown in Table 4.6:

Table 4.6: Experimental data and fitted values at 90 degree A.o.A.

Wind Tunnel Speed (<i>m/s</i>)	Thrust (<i>N</i>)	Rotor torque (<i>Nm</i>)	Fitted thrust (<i>N</i>)	Fitted rotor torque (<i>Nm</i>)
23.31	-1.4048	0.0129	-1.3965	0.0101
21.56	-1.0922	0.0155	-0.9937	0.0162
19.81	-0.7327	0.0196	-0.6049	0.0215
18.06	-0.2646	0.0233	-0.2451	0.0259
16.31	0.1276	0.0287	0.1166	0.0298
14.57	0.5379	0.0329	0.4604	0.0331
12.82	0.8901	0.0373	0.7999	0.0359
11.07	1.2569	0.0396	1.1166	0.0381
9.32	1.5607	0.0413	1.4259	0.0400
7.57	1.8332	0.0428	1.7181	0.0414
4.08	2.249	0.0425	2.2515	0.0431
2.33	2.4053	0.0429	2.4854	0.0435
0	2.536	0.0428	2.7682	0.0437

Parameters for vertical climb are presented in the Table 4.7. Because the angle of attack is $\frac{\pi}{2}$ in vertical flight case the second parameter drops. Hence there are two unknown coefficients to predict.

Table 4.7: Parameter estimation results for vertical climb using BET

Relation between thrust force and the angular velocity of the rotor, induced velocity, and climb velocity ($\alpha = \frac{\pi}{2}$)	$T = t_1 \Omega^2 + t_3 \Omega (v_i + V \sin \alpha) =$ $t_1 \Omega^2 + t_3 \Omega (v_i + V_c)$
Thrust Coefficients (@ 5820 RPM)	$t_1 = 1.2443 \times 10^{-7} \left(\frac{N}{RPM^2} \right)$ $t_3 = -4.2892 \times 10^{-5} \left(\frac{N}{RPM(m/s)} \right)$
Relation between rotor torque and the angular velocity of the rotor, induced velocity, and climb velocity	$Q = q_1 \Omega^2 + q_3 \Omega (v_i + V \sin \alpha) +$ $q_4 (v_i + V \sin \alpha)^2$
Thrust Coefficients (@ 5820 RPM)	$q_1 = 1.1874 \times 10^{-9} \left(\frac{Nm}{RPM^2} \right)$ $q_3 = 2.2004 \times 10^{-7} \left(\frac{Nm}{RPM(m/s)} \right)$ $q_4 = -1.1667 \times 10^{-4} \left(\frac{Nm}{(m/s)^2} \right)$

Test data and fitted thrust and rotor torque graphs w.r.t. the angular velocity of the rotor in vertical climb flight, at 5820 RPM are shown in Figure 4.6 and 4.7, respectively. Hub force and rolling moment are zero in vertical climb flight because angle of attack equals to zero.

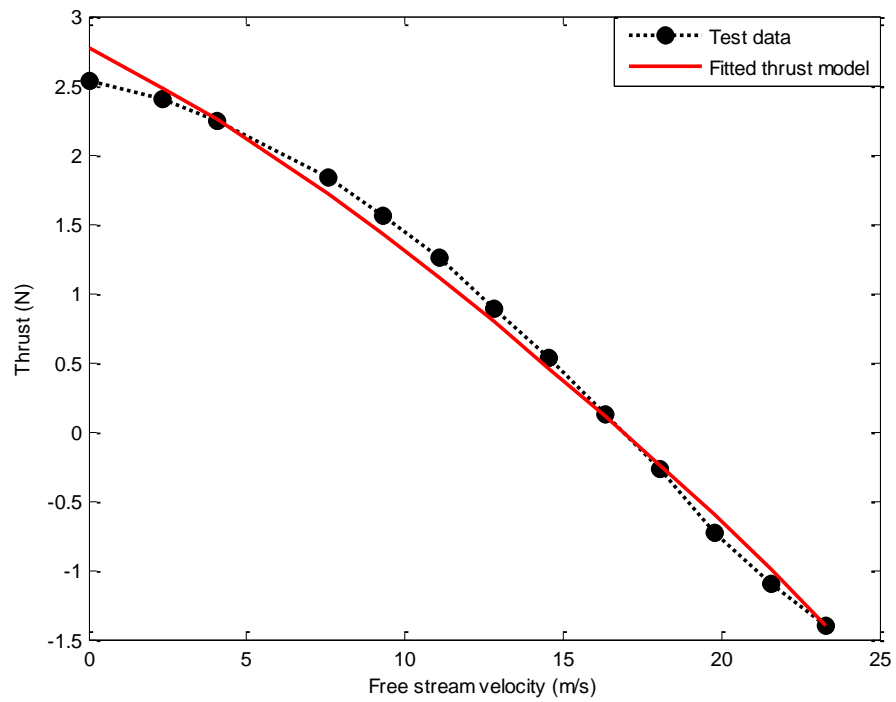


Figure 4.6: Thrust and fitted thrust w.r.t. the free stream velocity at 5820 *RPM* using BET

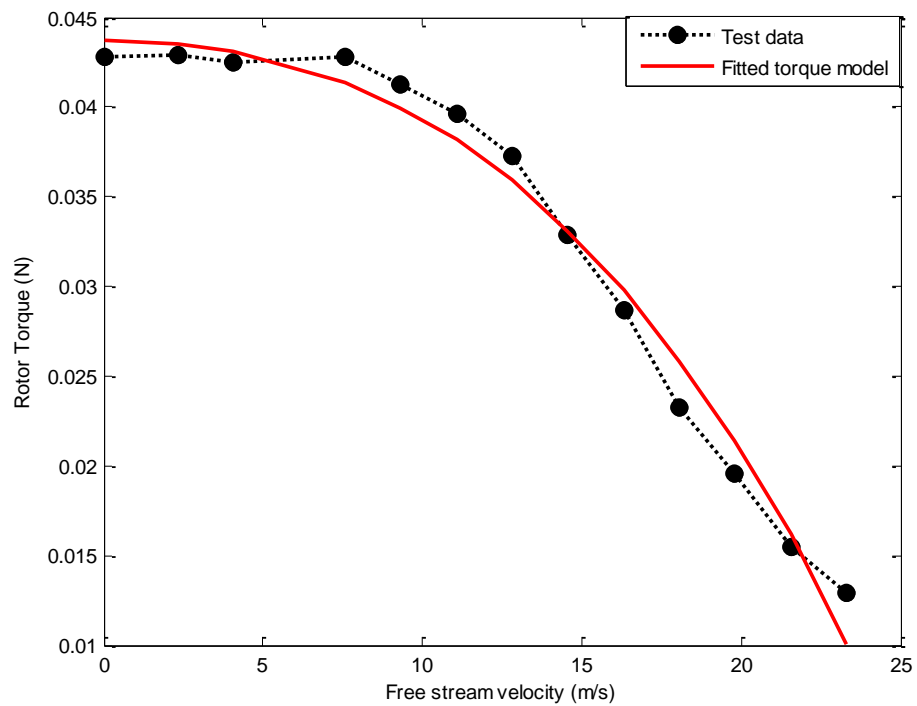


Figure 4.7: Rotor torque and fitted rotor torque in vertical climb flight at 5820 *RPM* using BET

The coefficient of determination is presented in the following table:

Table 4.8: Coefficient of determination in vertical climb using BET

Thrust	Rotor torque
$R^2=0.9931$	$R^2=0.9807$
$R^2_{adj}=0.9999$	$R^2_{adj}=0.9998$

As the wind tunnel speed (free stream velocity) increases, thrust force decreases [Figure 4.8]:

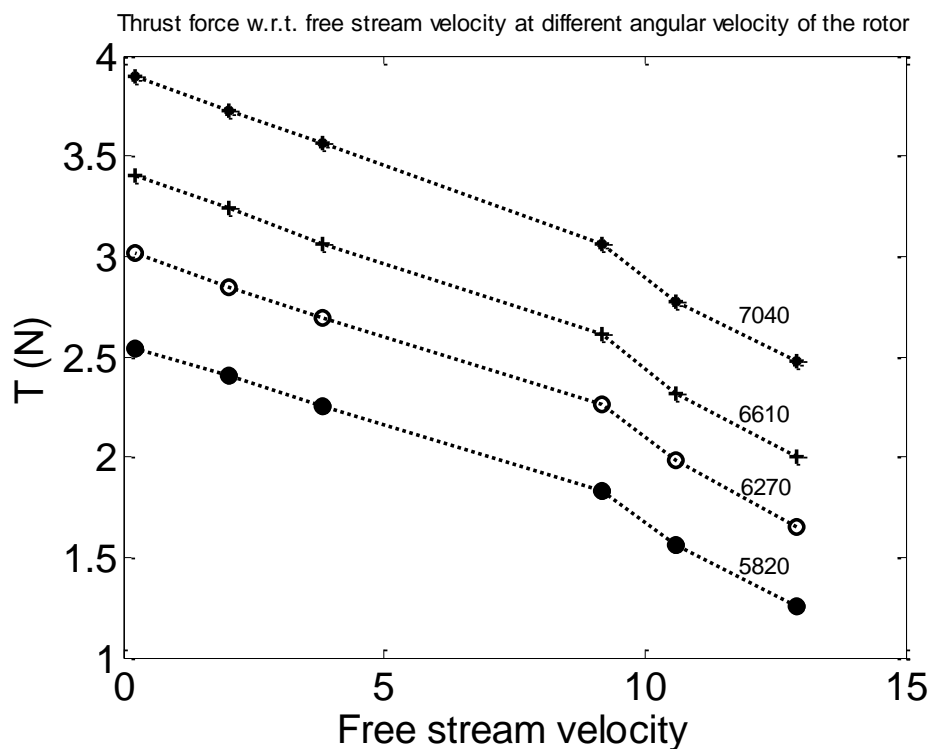


Figure 4.8: Change of thrust w.r.t. free stream velocity in vertical flight at different angular velocity of the rotor (RPM)

In Figure 4.6, the model using blade element theory gives a linear relation between thrust force and free stream velocity. However, experimental data shows that, there is a quadratic relation between them. This approach does not satisfy the expected trend. Therefore, an empirical model is generated instead of using blade element theory:

$$T = -0.3655 - 2.2895 \times 10^{-5}\Omega + 8.9193 \times 10^{-8}\Omega^2 - 0.2153V_c + 6.8858 \times 10^{-8}\Omega V_c - 6.8192 \times 10^{-9}\Omega^2 V_c + 0.0224V_c^2 - 8.8711 \times 10^{-6}\Omega V_c^2 + 7.4421 \times 10^{-10}\Omega^2 V_c^2$$

The results of the empirical relation mentioned above are presented in Figure 4.9:

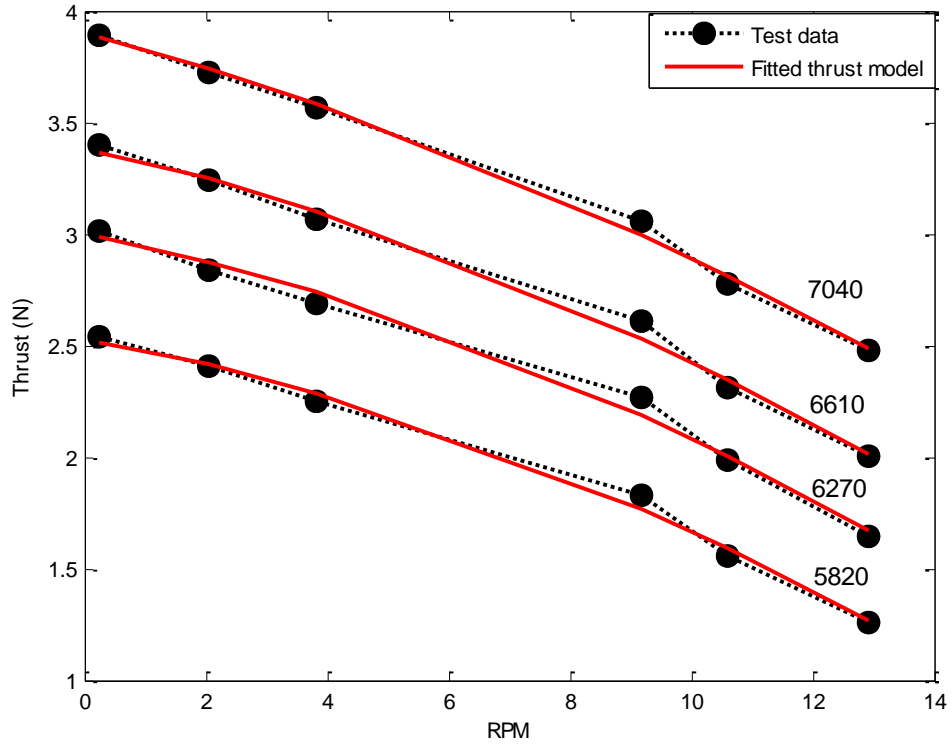


Figure 4.9: Test data and fitted model in different angular velocity of the rotor in vertical climb flight at different angular velocity of the rotor (RPM)

According to test data and fitted thrust model in Figure 4.9, the empirical model fits better than the model using blade element theory.

Induced velocity is calculated using Equation 2.21. Then, the change of induced velocity w.r.t. the free stream velocity at different angular velocities of the rotor is presented in Figure 4.10:

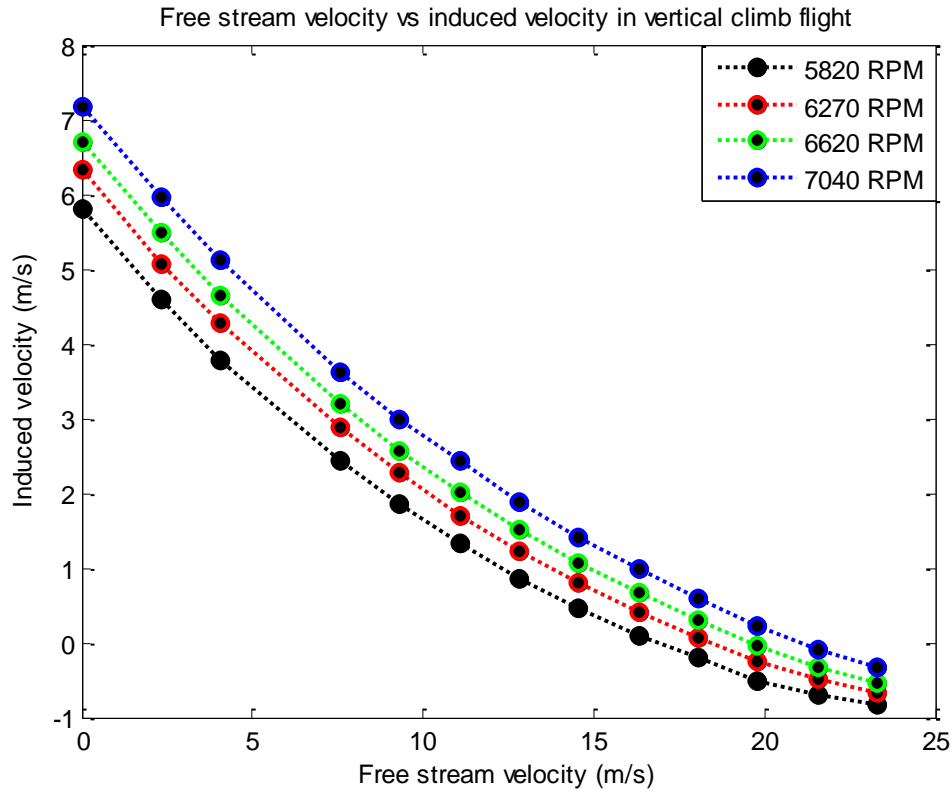


Figure 4.10: Change of induced velocity at different angular velocity of rotor

Parameters predicted by method of least squares and numerically calculated can be seen in the table 4.9 and 4.10, respectively.

Table 4.9: Coefficients found experimentally using BET

Thrust	Hub Force	Rolling Moment	Rotor Torque
$t_1=8.8550e-08(N/RPM^2)$	$h_1 = 9.4959e-06$ ($N/(RPM(m/s))$)	$r_1=1.7516e-05$ ($Nm/(RPM(m/s))$)	$q_1=2.7046e-09$ (Nm/RPM^2)
$t_2=0.0020$ ($N/(m/s)^2$)	$h_2=-6.1622e-04$ ($N/(m/s)^2$)	$r_2=-1.0106e-04$ ($Nm/(RPM(m/s))$)	$q_2=-3.3064e-05$ ($Nm/(m/s)^2$)
$t_3=-1.4155e-05$ ($N/(rpm(m/s))$)			$q_3=-1.9208e-07$ ($Nm/(RPM(m/s))$)
			$q_4=5.7485e-05$ ($Nm/(m/s)^2$)

Table 4.10: Coefficients found numerically using BET

Thrust	Hub Force	Rolling Moment	Rotor Torque
$t_{1n}=4.6285\text{e-}06$ (N/RPM^2)	$h_{1n}=3.1651\text{e-}05$ ($N/(RPM(m/s))$)	$r_{1n}= -4.6285\text{e-}06$ ($Nm/(RPM(m/s))$)	$q_{1n}=1.6336\text{e-}07$ (Nm/RPM^2)
$t_{2n}=7.0460\text{e-}04$ ($N/(m/s)^2$)	$h_{2n}=7.0460\text{e-}04$ ($N/(m/s)^2$)	$r_{2n}=8.2862\text{e-}05$ ($Nm/(RPM(m/s))$)	$q_{2n}=1.5825\text{e-}05$ ($Nm/(m/s)^2$)
$t_{3n}= -1.6572\text{e-}04$ ($N/(RPM(m/s))$)			$q_{3n}=4.6285\text{e-}06$ ($Nm/(RPM(m/s))$)
			$q_{4n}= -1.6572\text{e-}04$ ($Nm/(m/s)^2$)

By using the coefficient of determination, the reliability of the unknowns is obtained [Table 4.11]:

Table 4.11: Coefficient of determination in forward flight by using BET

	Thrust	Hub Force	Rolling Moment	Rotor Torque
R^2	0.9947	0.6734	0.497	0.9616
R_{adj}^2	0.9947	0.6718	0.453	0.9612

Test data and fitted thrust models using BET and method of least squares are shown in Figure 4.11, 4.12, 4.13, 4.14. Experimental results and fitted thrust forces w.r.t. angular velocity of the rotor, at 6 different wind tunnel speeds, and at zero degree A.o.A. are presented in Figure 4.11:

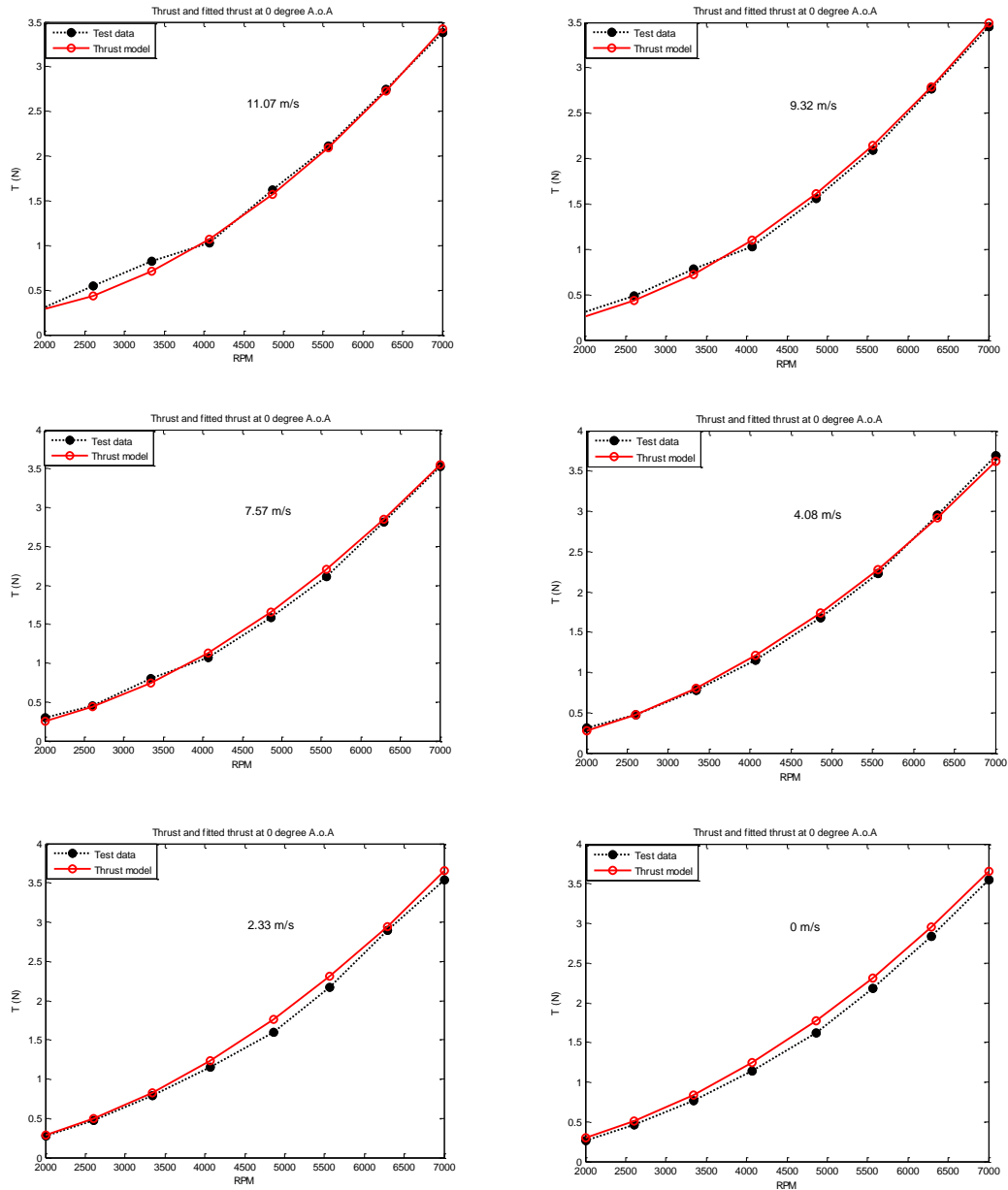


Figure 4.11: Test data and fitted thrust model w.r.t. angular velocity of rotor for different wind speeds at 0 degree A.o.A.

Test data and fitted models for thrust force w.r.t. angular velocity of the rotor, at 6 different wind tunnel speeds, and at 30 degree A.o.A. are presented in Figure 4.12:

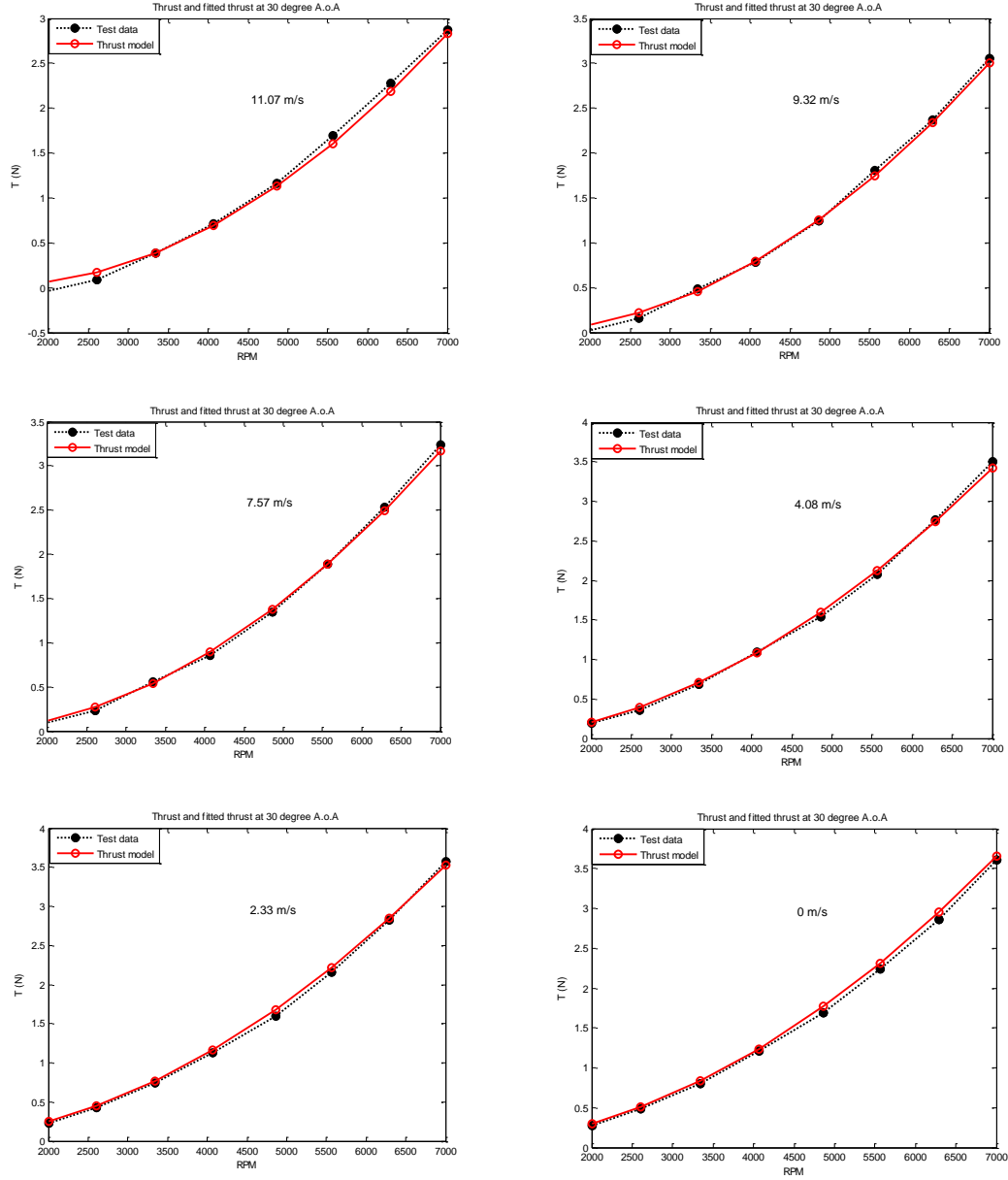


Figure 4.12: Test data and fitted thrust model w.r.t. angular velocity of rotor for different wind speeds at 30 degree A.o.A.

Test data and fitted models for thrust force w.r.t. angular velocity of the rotor, at 6 different wind tunnel speeds, and at 45 degree A.o.A. are presented in Figure 4.13:

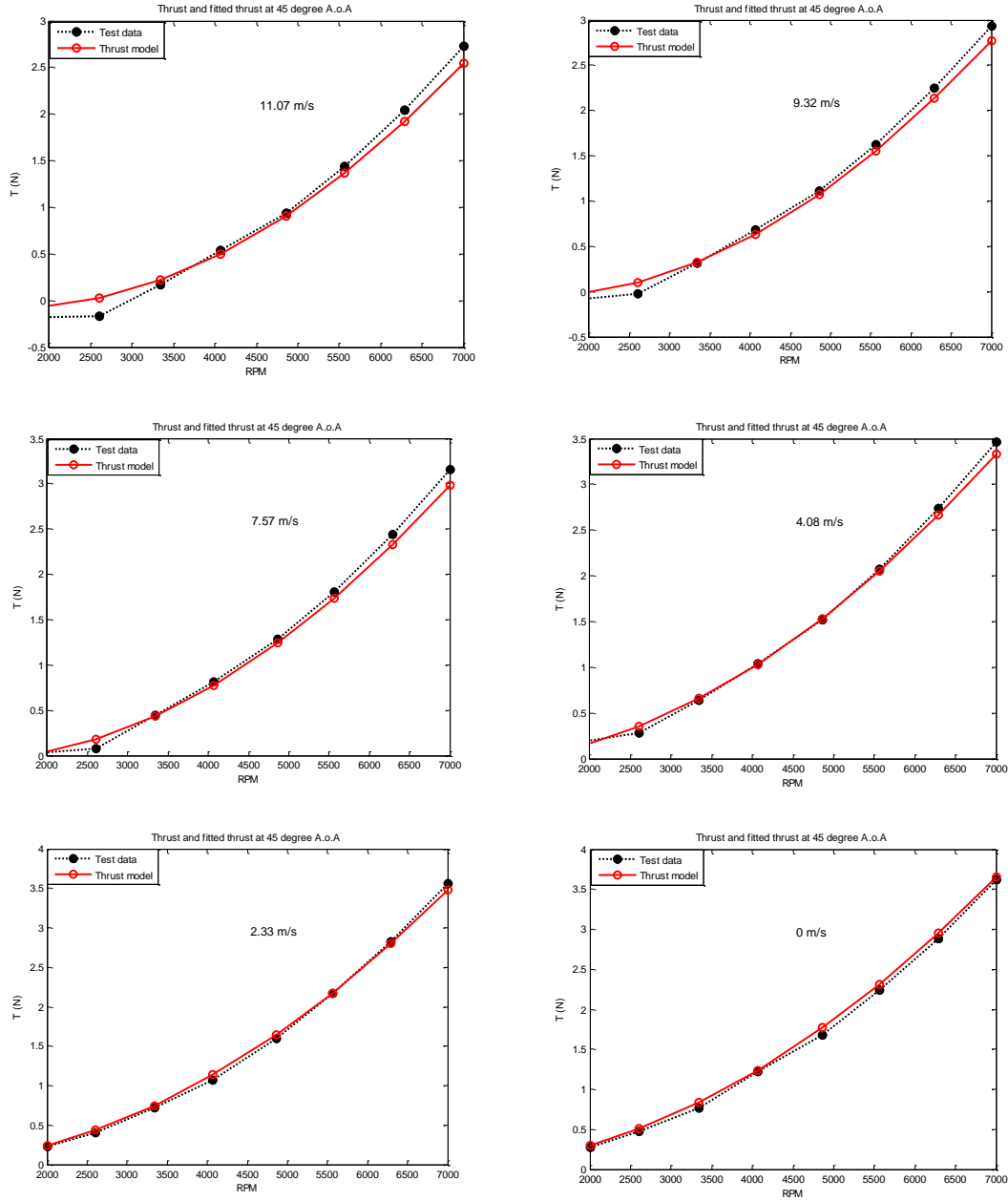


Figure 4.13: Test data and fitted thrust model w.r.t. angular velocity of rotor for different wind speeds at 45 degree A.o.A.

Test data and fitted models for thrust force w.r.t. angular velocity of the rotor, at 6 different wind tunnel speeds, and at 60 degree A.o.A. are presented in Figure 4.14:

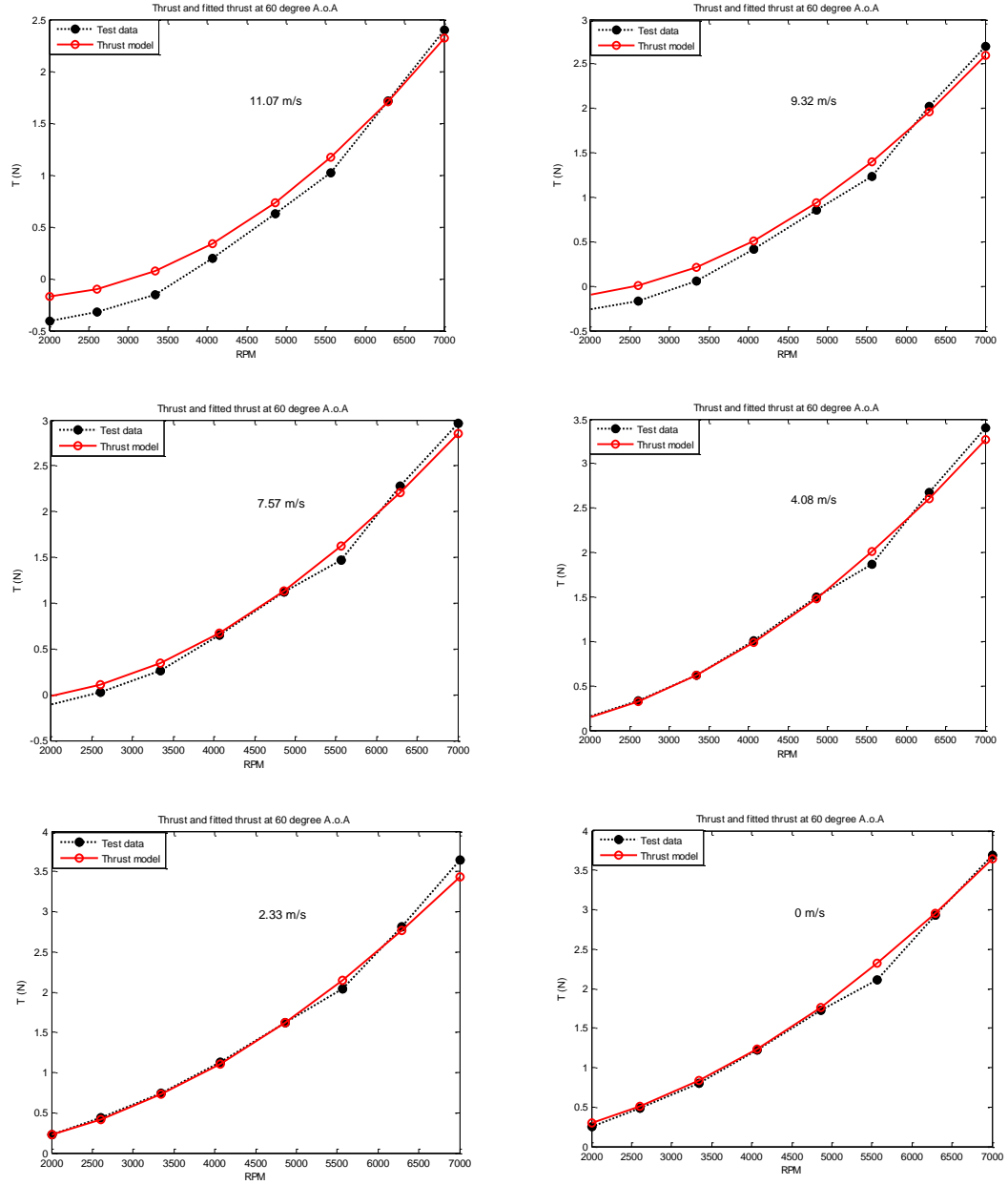


Figure 4.14: Test data and fitted thrust model w.r.t. angular velocity of rotor for different wind speeds at 60 degree A.o.A.

Although thrust and fitted model is reliable w.r.t. angular velocity of rotor, it is not a good prediction w.r.t. free stream velocity as it can be seen clearly in Figure 4.15, 4.16, 4.17:

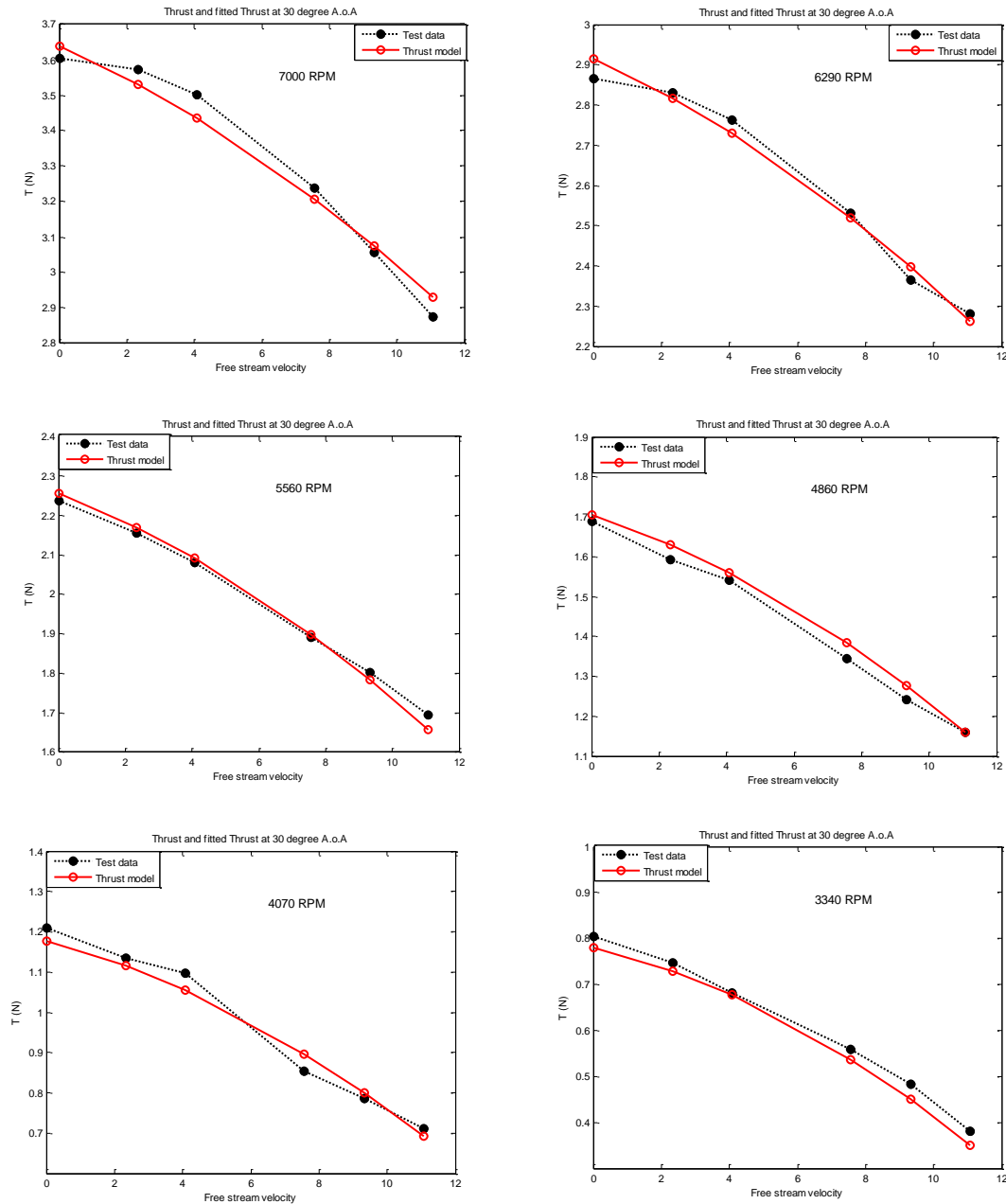
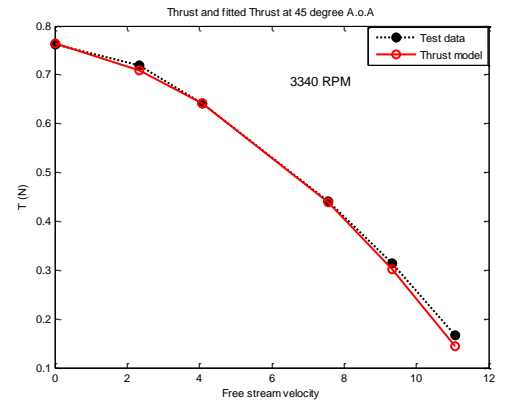
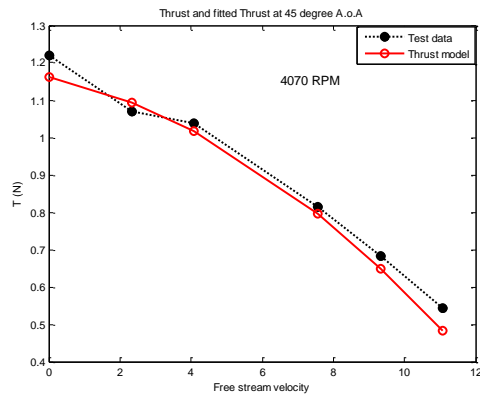
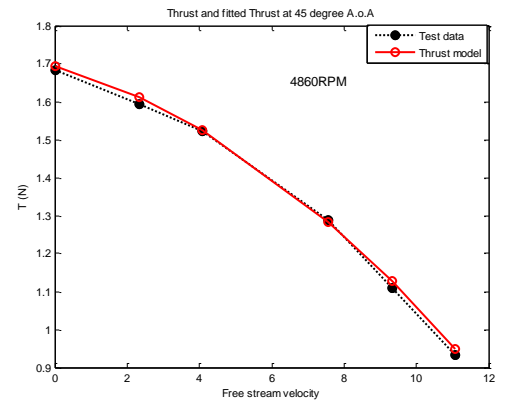
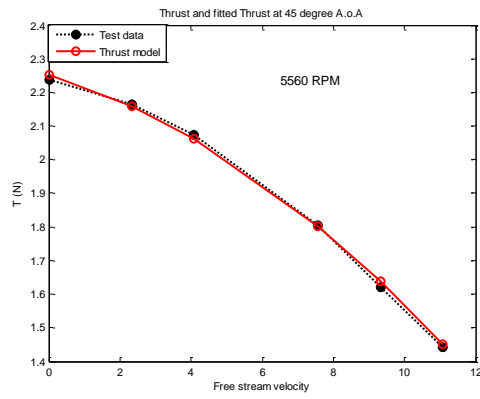
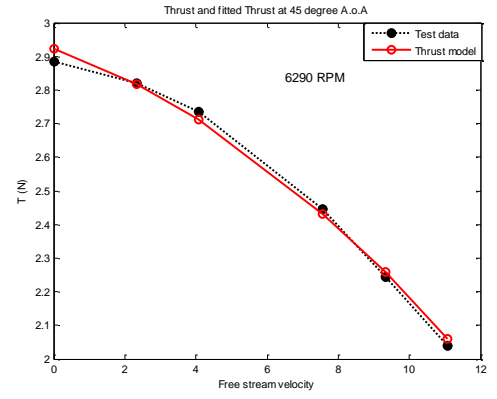
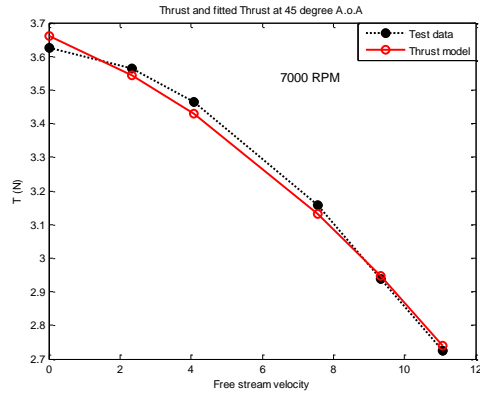


Figure 4.15: Test data and fitted thrust model w.r.t. free stream velocity for different rotor speeds at 30 degree A.o.A.



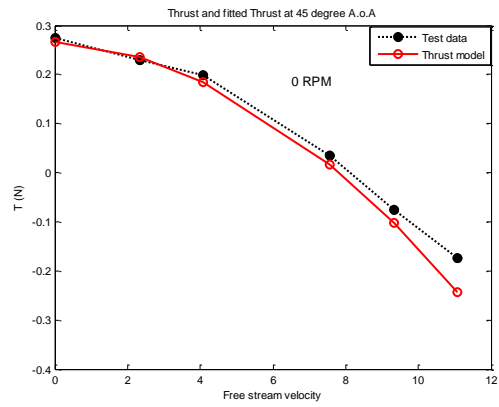
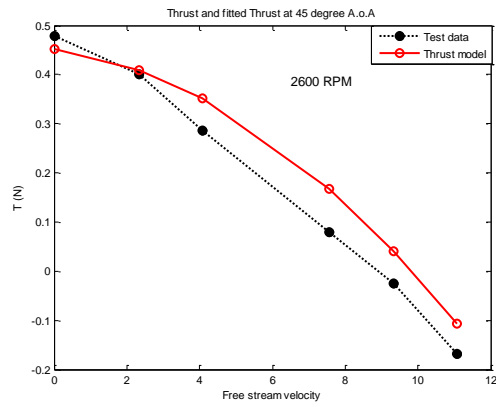
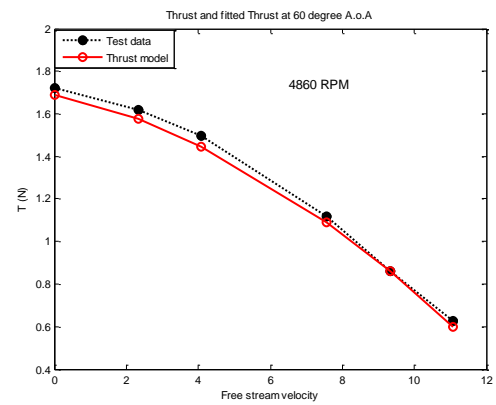
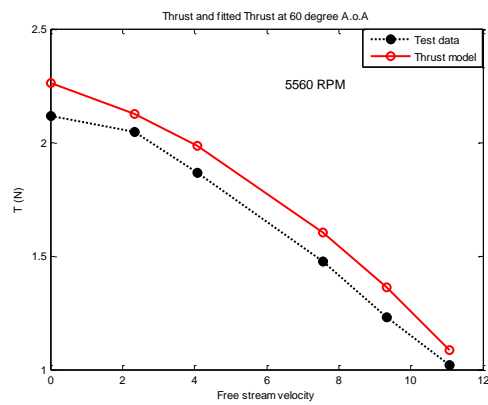
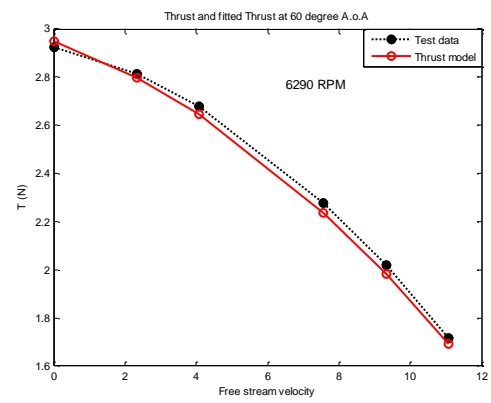
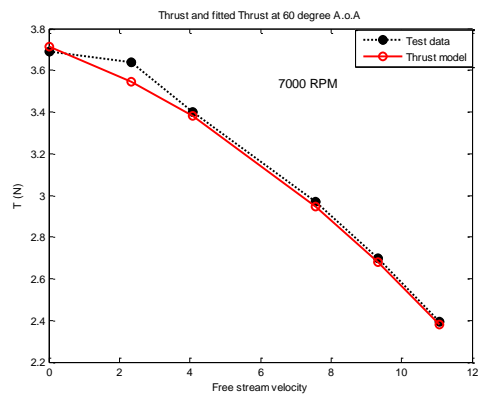


Figure 4.16: Test data and fitted thrust model w.r.t. free stream velocity for different rotor speeds at 45 degree A.o.A.



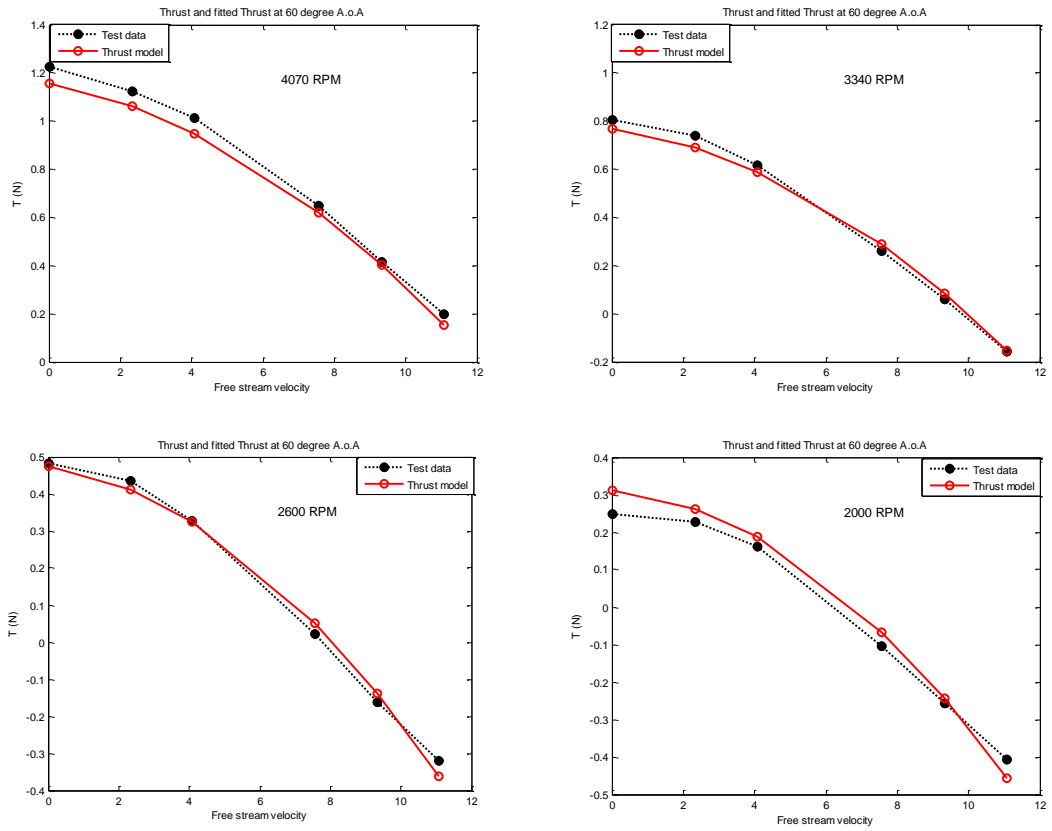


Figure 4.17: Test data and fitted model w.r.t. free stream velocity for different rotor speeds at 60 degree A.o.A.

Induced velocity is calculated using Equation 2.38, and plotted w.r.t. free stream velocity [Figure 4.18].

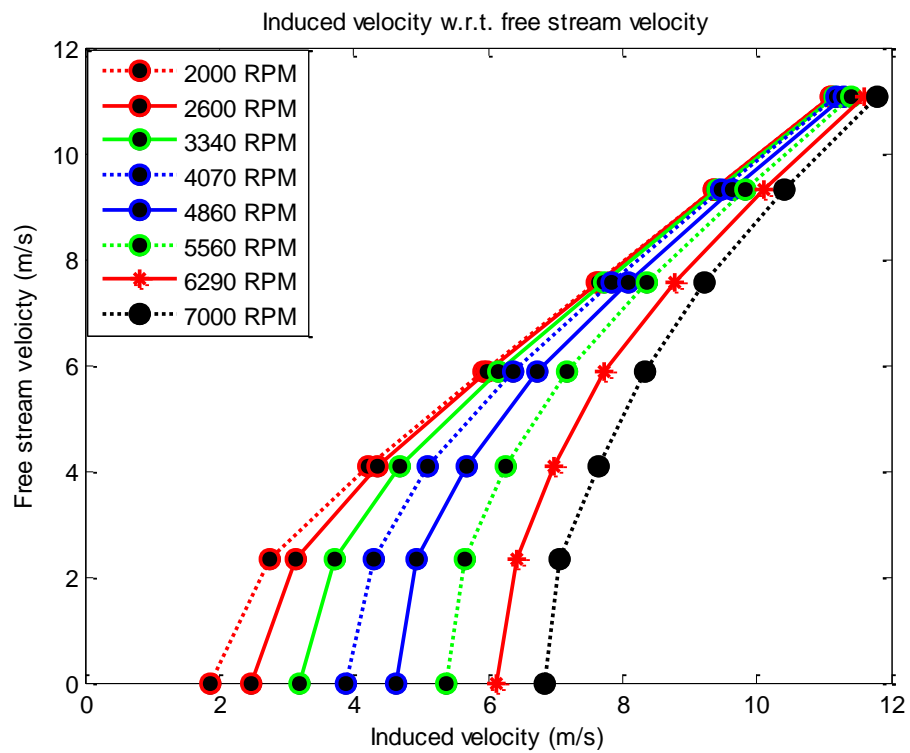


Figure 4.18: Induced velocity at different angular velocity of the rotor in forward flight

Test data and fitted rotor torque model using BET and least squares method are presented in Figure 4.19:

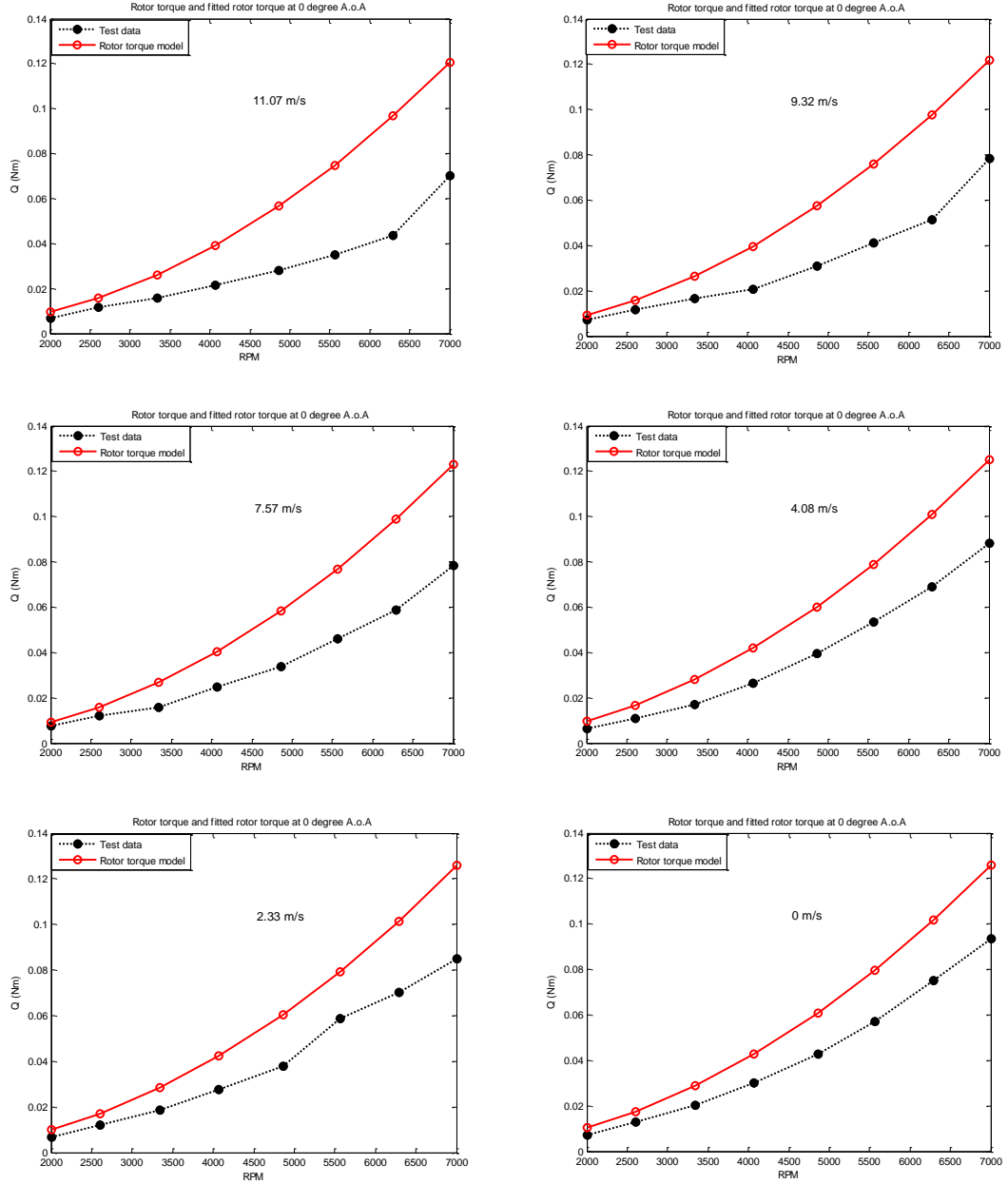


Figure 4.19: Test data and fitted rotor torque model using BET at 0 degree A.o.A. for different wind speeds

Test data and fitted hub force model using blade element theory and least squares method are presented in Figure 4.20:

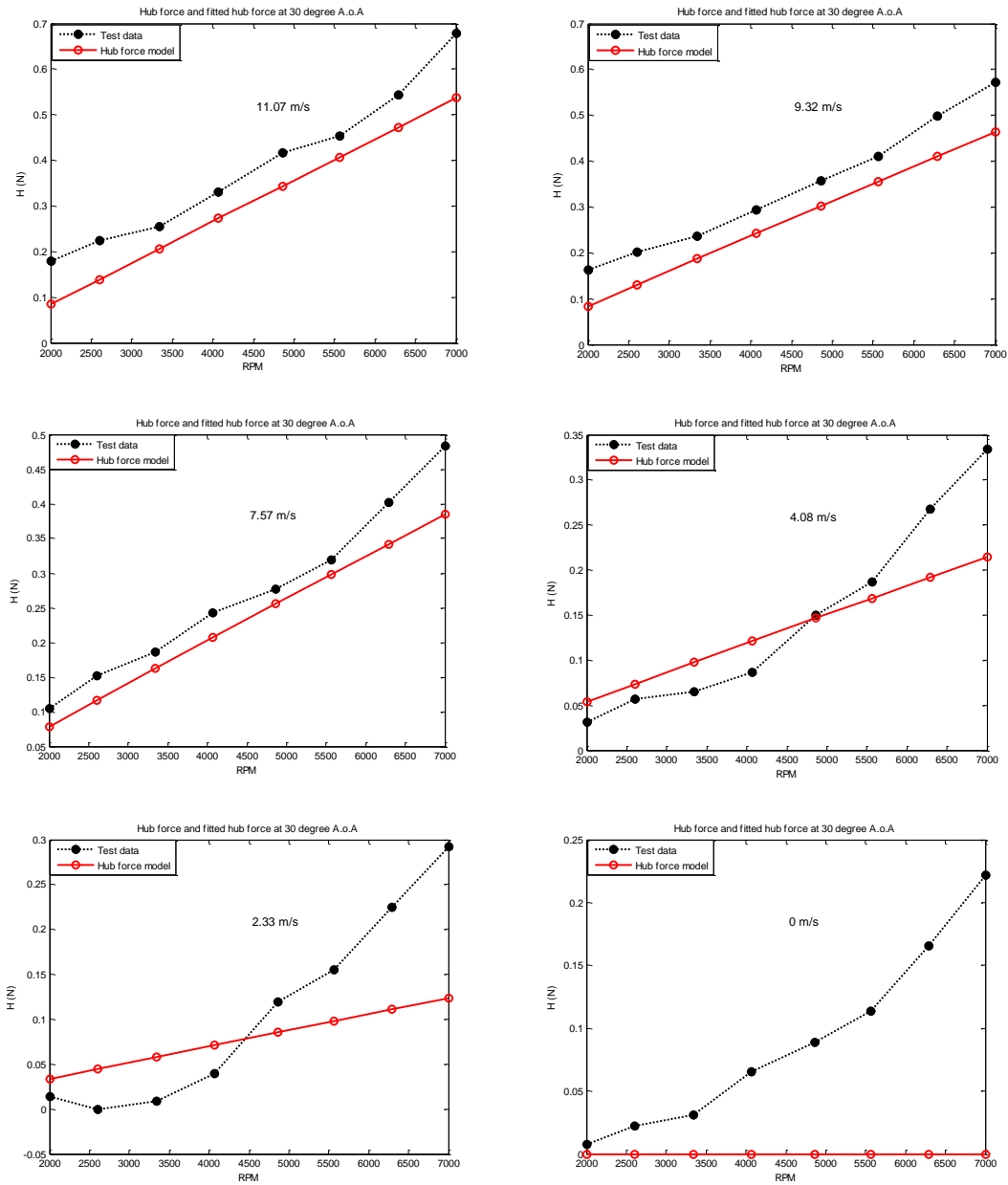


Figure 4.20: Test data and fitted hub force model using BET at 30 degree A.o.A. for different wind speeds

4.2. Results by using Surface Fitting

Results presented in the previous section show that an empirical model can fit the test data better than the model based on the blade element theory. In particular blade element theory fails to predict changes in thrust force with respect to free stream

velocity accurately. Therefore a second order multivariable polynomial model is used to fit the test data.

Thanks to the MATLAB surface fitting tool-box, the following relation is generated between thrust force, free stream velocity, and angular velocity of the rotor at different angles of attack:

$$T(\alpha, V, \Omega) = p_{00}(\alpha) + p_{10}(\alpha)V + p_{01}(\alpha)\Omega + p_{20}(\alpha)V^2 + p_{11}(\alpha)\Omega V + p_{02}(\alpha)\Omega^2$$

Table 4.12: Coefficients of thrust force at different angles of attack

	0°	30°	45°	60°	90°
p_{00}	0.1402	0.05801	0.08652	0.245	-0.1448
p_{10}	0.02587	0.005815	0.01003	0.01297	0.02041
p_{01}	-0.000108	-5.375e-05	-7.827e-05	-0.0001523	-7.633e-05
p_{20}	-0.001166	-0.001962	-0.003733	-0.005578	-0.006282
p_{11}	-4.088e-06	-6.859e-06	-7.399e-06	-1.027e-05	-1.157e-05
p_{02}	8.606e-08	8.076e-08	8.412e-08	9.255e-08	9.249e-08

Test data and fitted thrust model graphs in 3D using surface fitting at 90, 60, 45, 30, and 0 degrees are as follows:

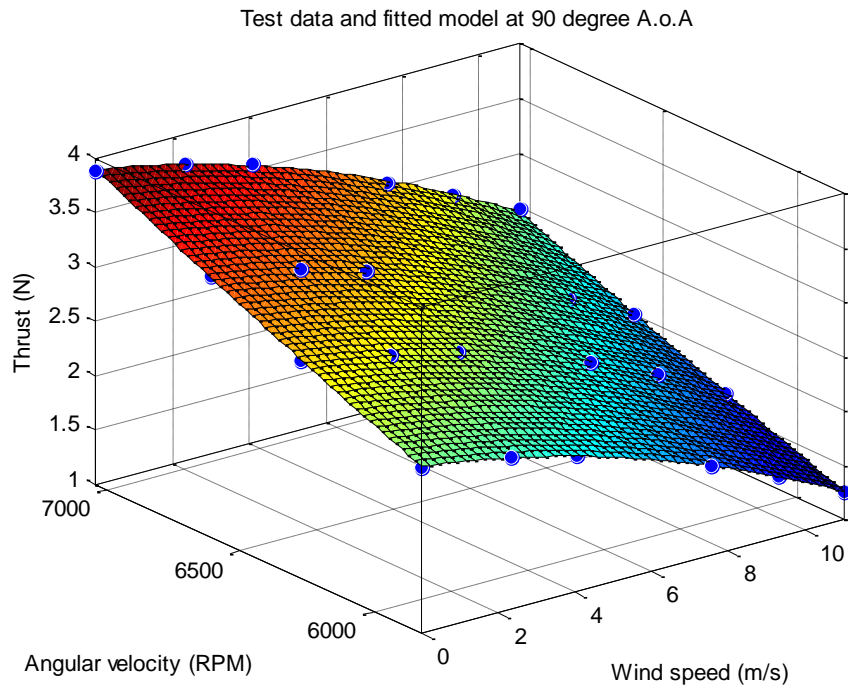


Figure 4.21: Surface fitting at 90 degree A.o.A. for thrust force

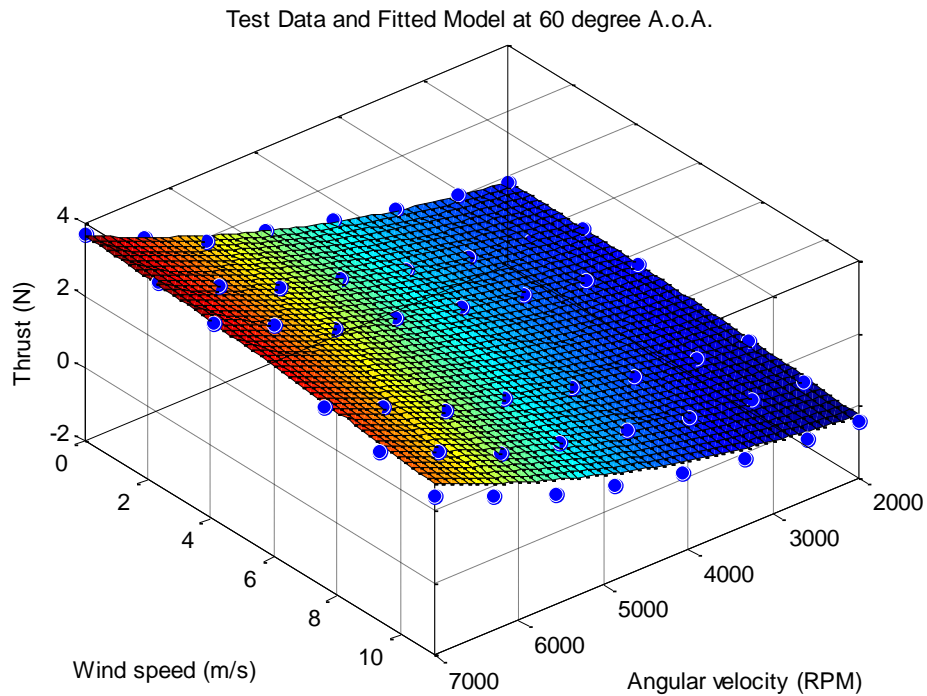


Figure 4.22: Surface fitting at 60 degree A.o.A. for thrust force

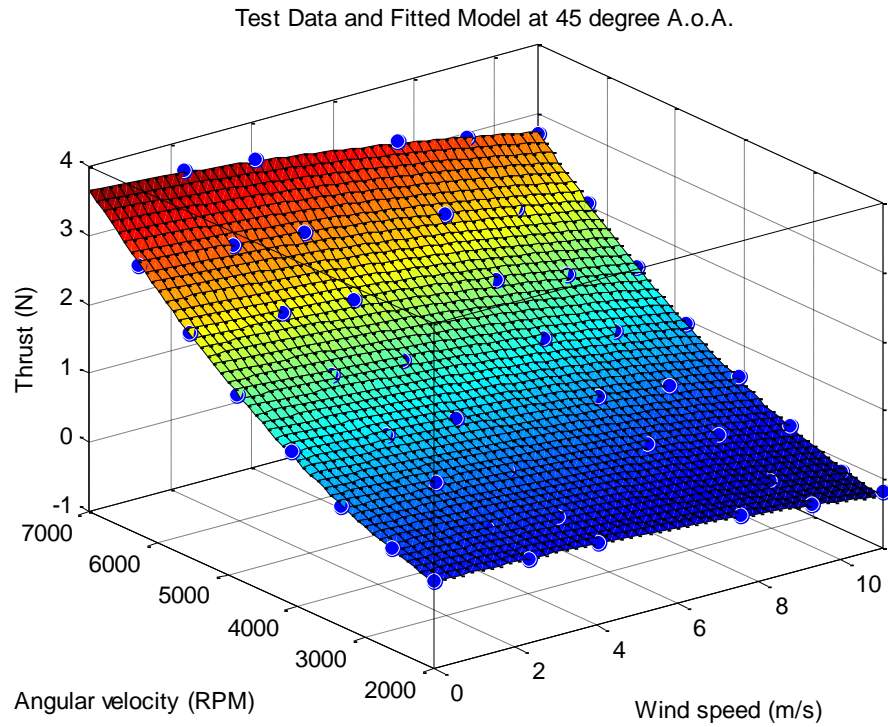


Figure 4.23: Surface fitting at 45 degree A.o.A. for thrust force

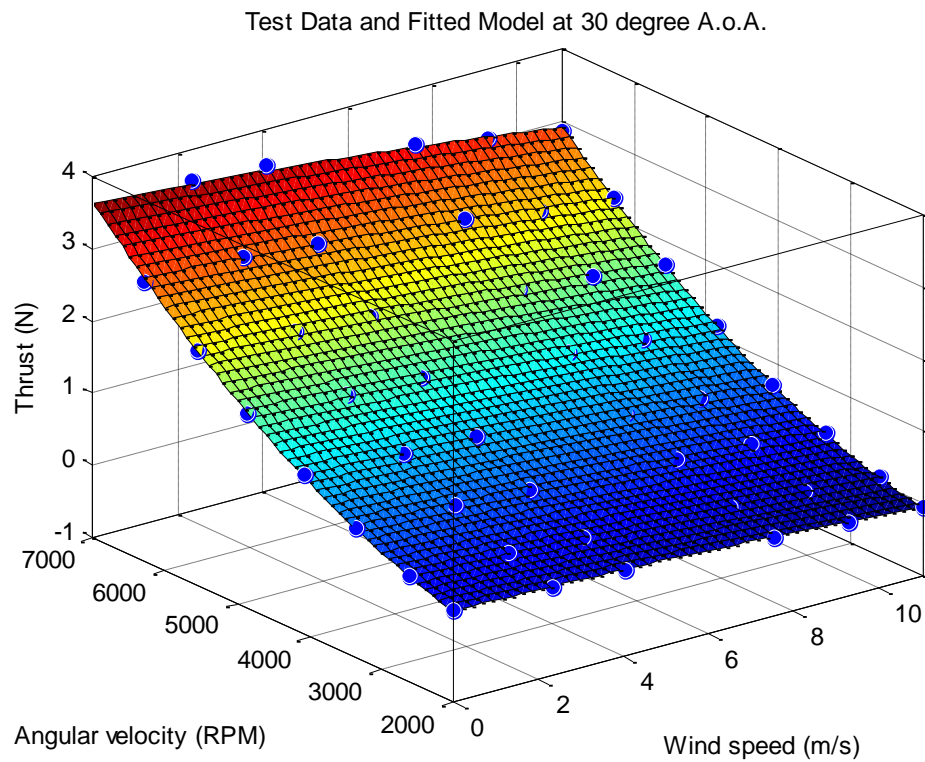


Figure 4.24: Surface fitting at 30 degree A.o.A. for thrust force

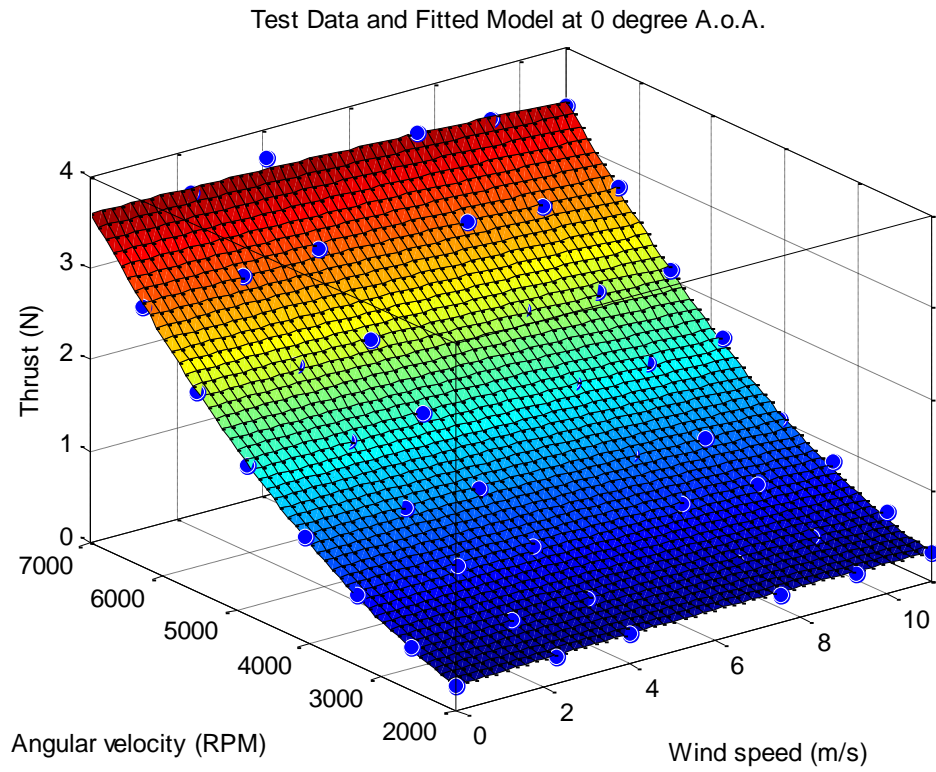


Figure 4.25: Surface fitting at 0 degree A.o.A. for thrust force

Test data and fitted thrust model w.r.t. angular velocity of the rotor at 0 degree A.o.A. at different wind tunnel speeds are as follows:

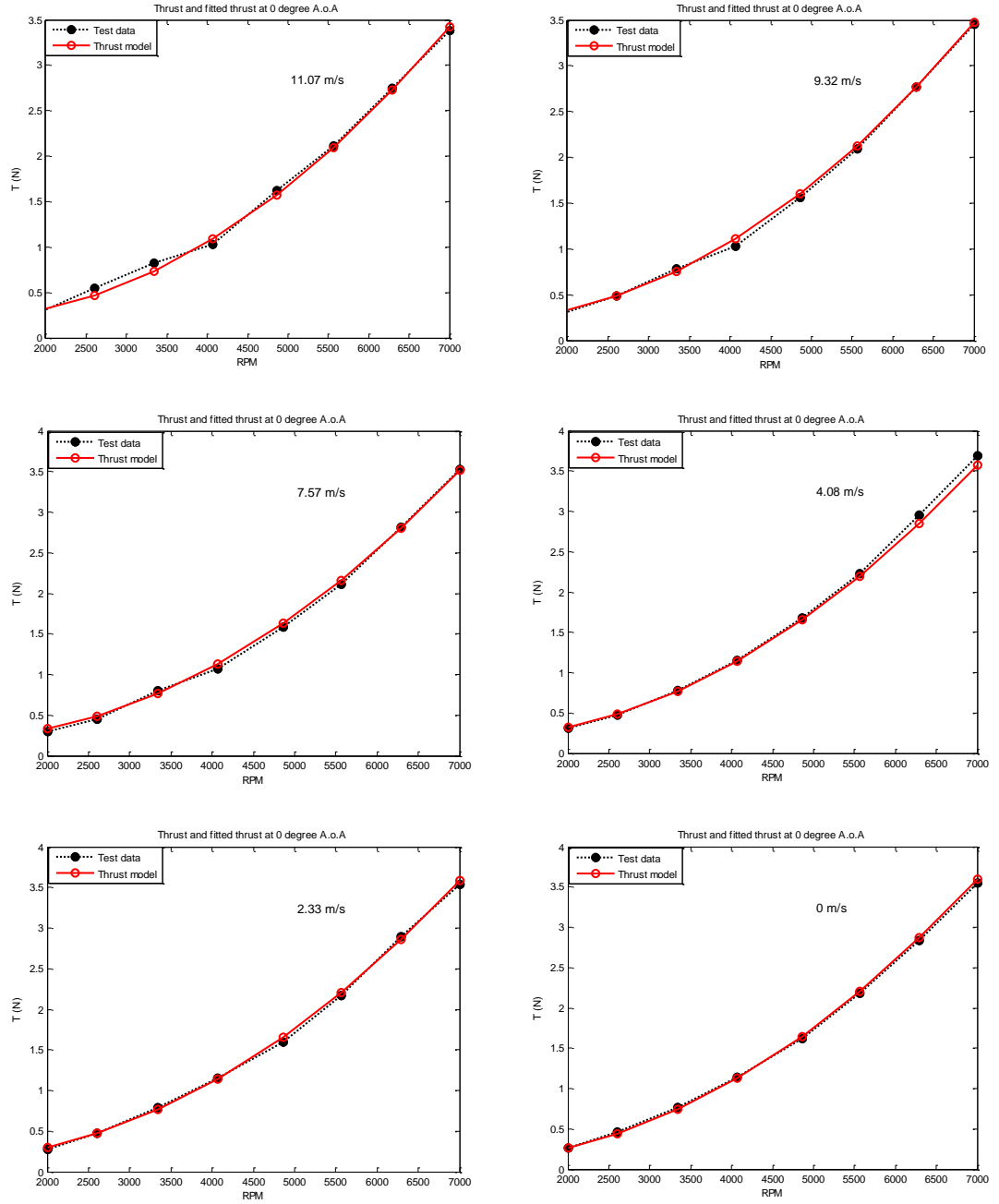


Figure 4.26: Test data and fitted thrust model at 0 degree A.o.A. w.r.t. the angular velocity of the rotor for different wind speeds

Test data and fitted thrust model w.r.t. angular velocity of the rotor at 30 degree A.o.A. at different wind tunnel speeds are as follows:

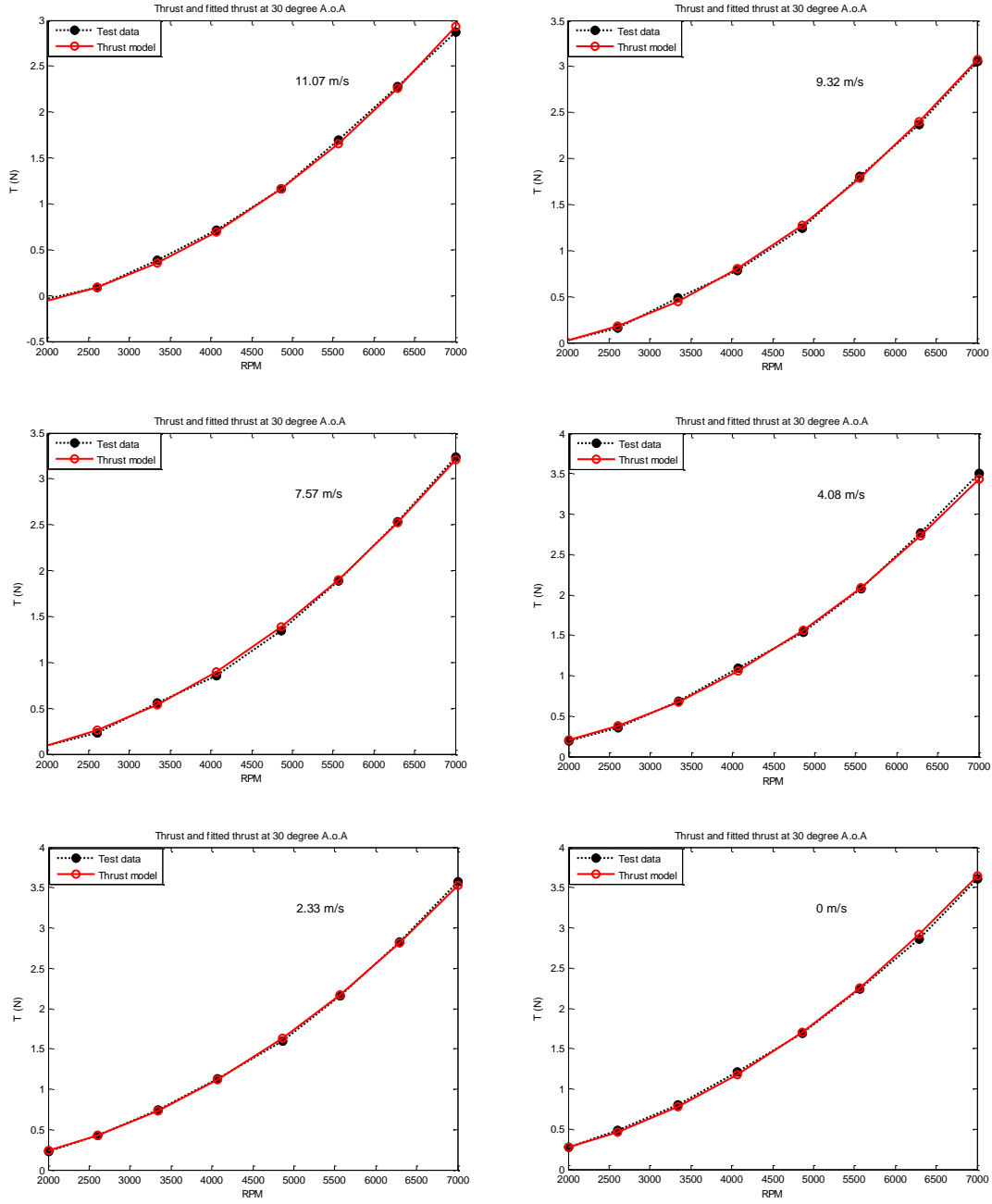


Figure 4.27: Test data and fitted thrust model at 30 degree A.o.A. w.r.t. the angular velocity of the rotor for different wind speeds

Test data and fitted thrust model w.r.t. angular velocity of the rotor at 45 degree A.o.A. at different wind tunnel speeds are as follows:

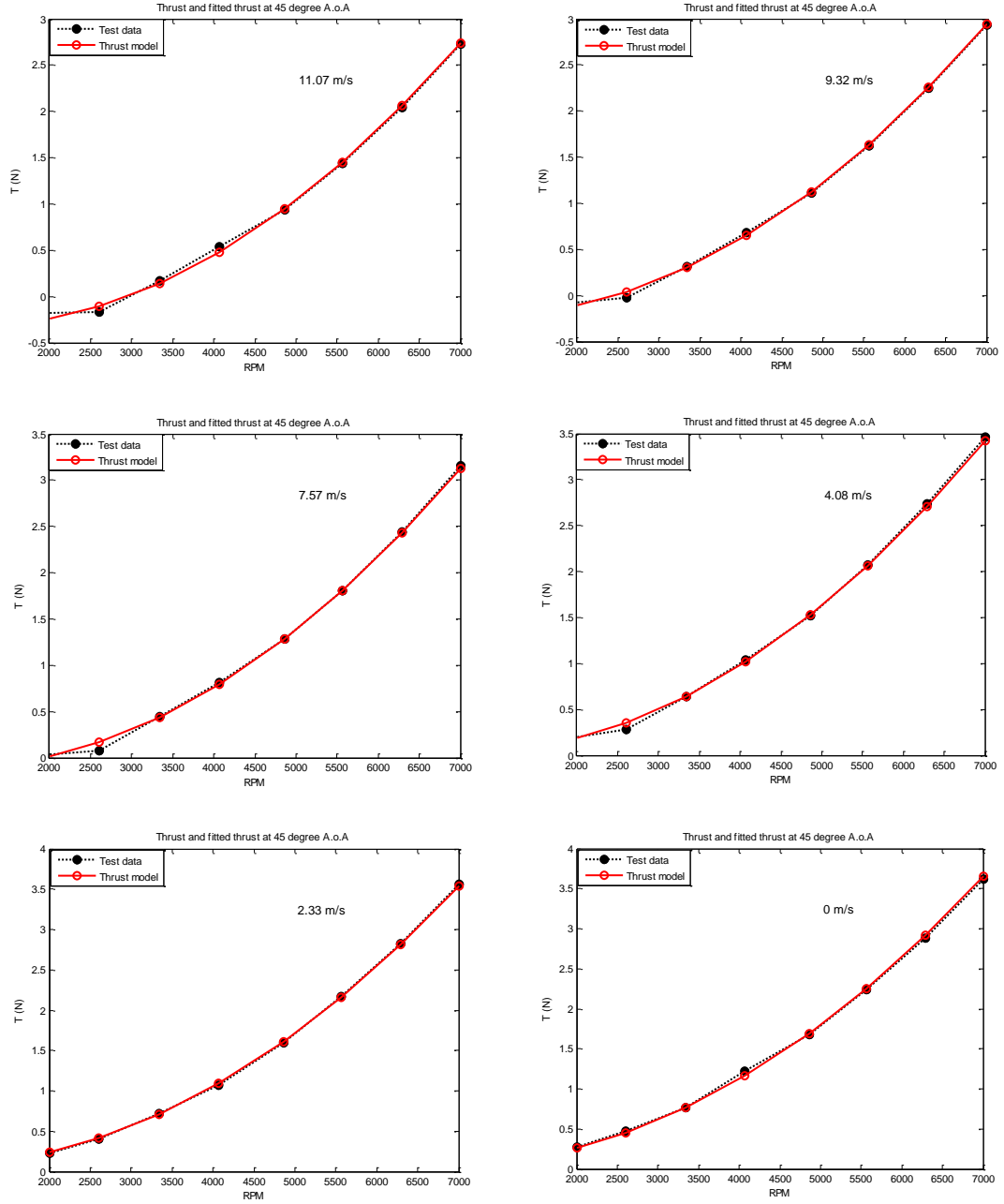


Figure 4.28: Test data and fitted thrust model at 45 degree A.o.A. w.r.t. the angular velocity of the rotor for different wind speeds

Test data and fitted thrust model w.r.t. angular velocity of the rotor at 60 degree A.o.A. at different wind tunnel speeds are as:

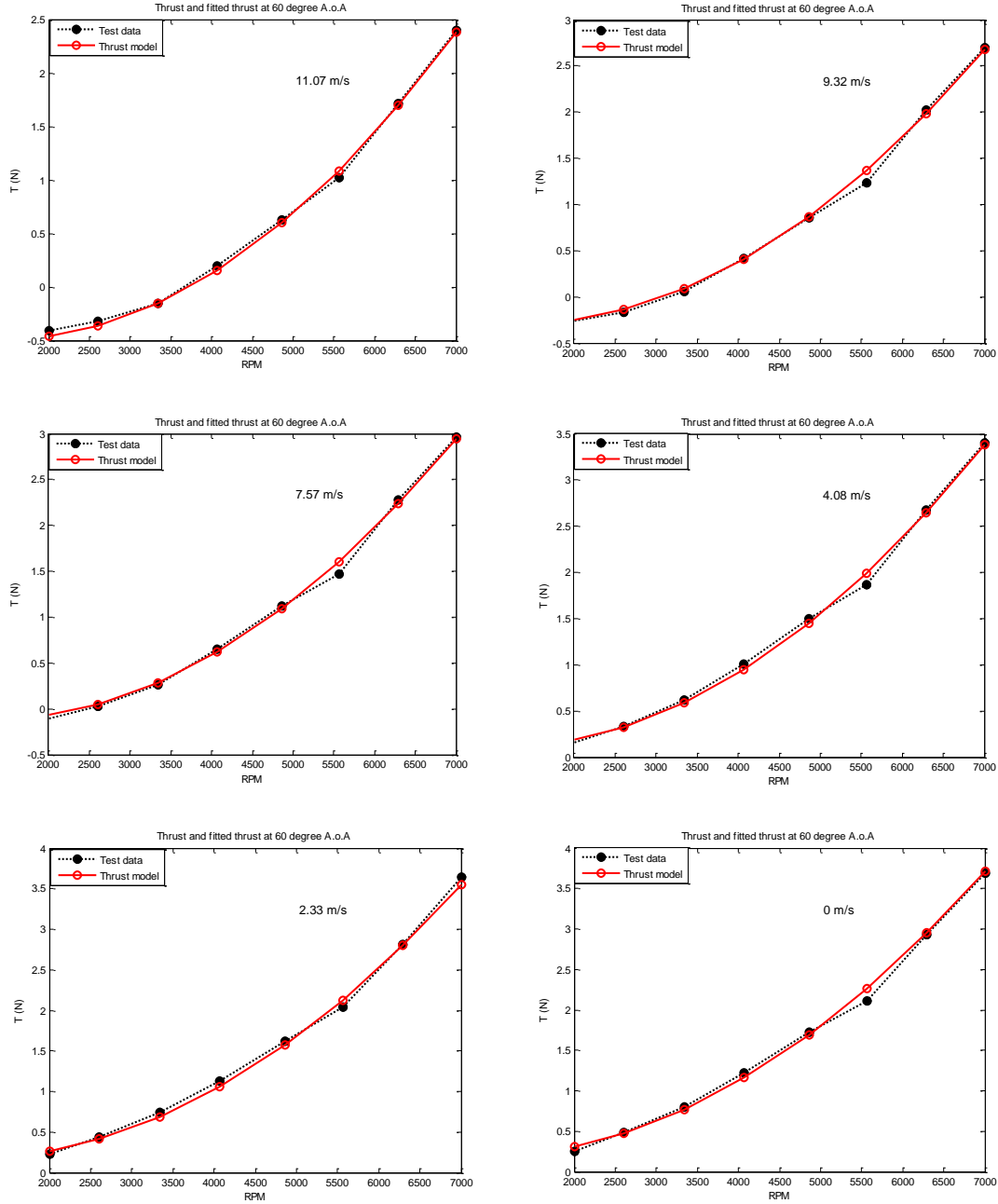


Figure 4.29: Test data and fitted thrust model at 60 degree A.o.A. w.r.t. the angular velocity of the rotor for different wind speeds

Test data and fitted thrust model w.r.t. free stream velocity at 30 degree A.o.A. at different rotor speeds are as follows:

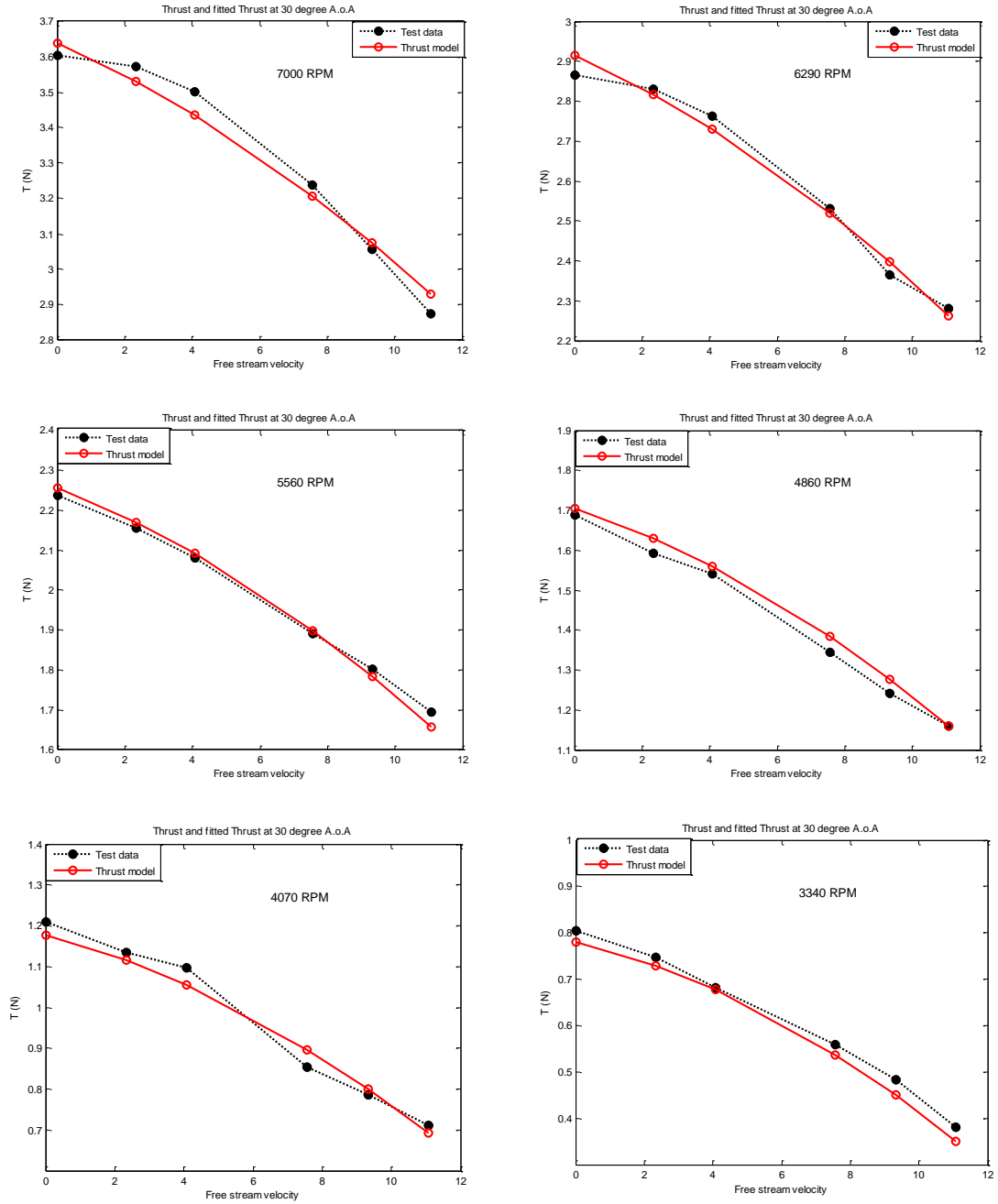
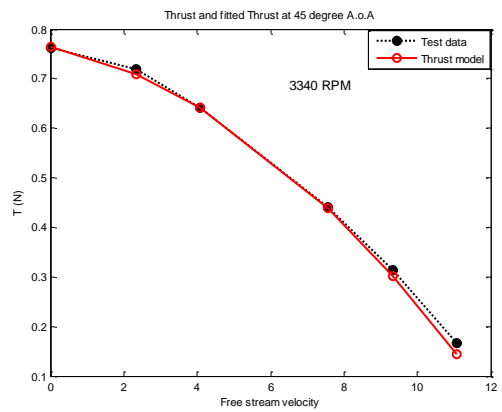
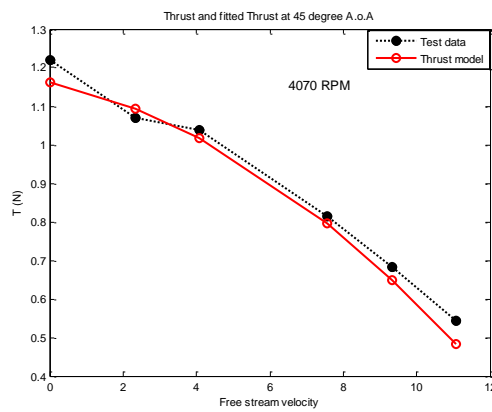
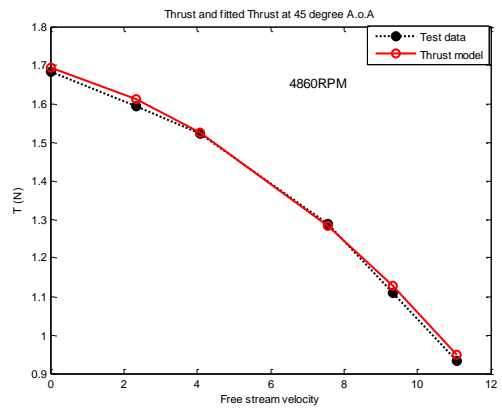
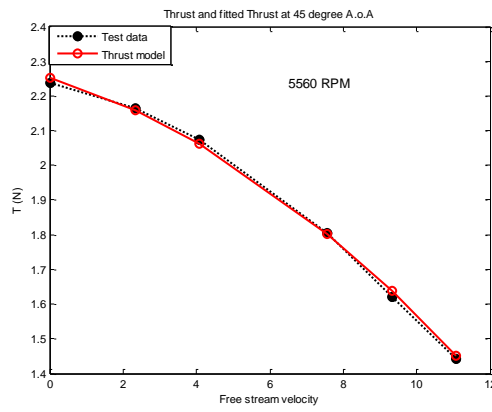
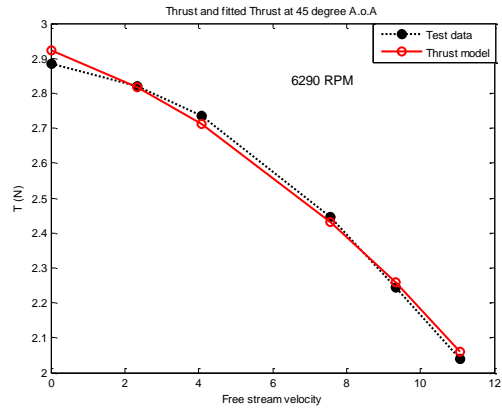
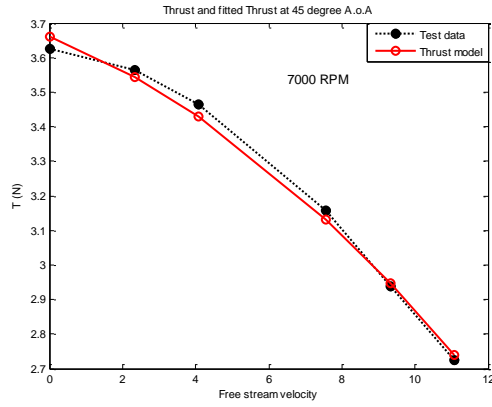


Figure 4.30: Test data and fitted thrust model at 30 degree A.o.A. w.r.t. free stream velocity for different rotor speeds

Test data and fitted thrust model w.r.t. free stream velocity at 45 degree A.o.A. at different rotor speeds are as:



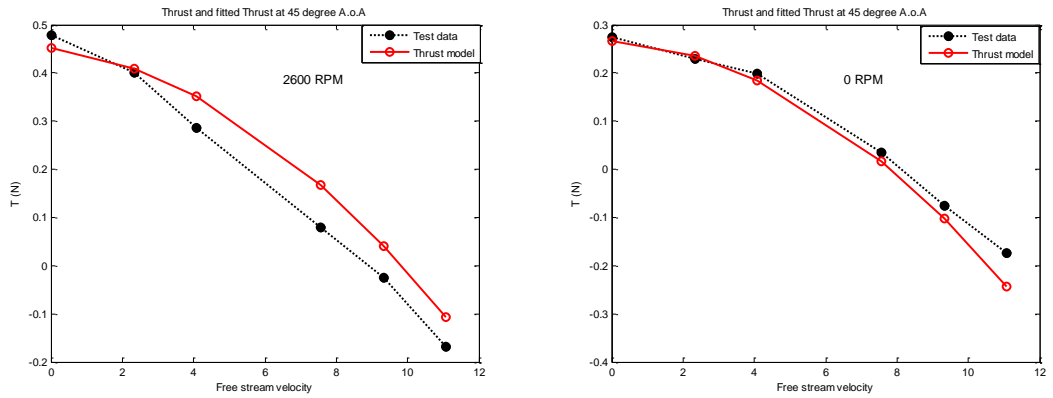
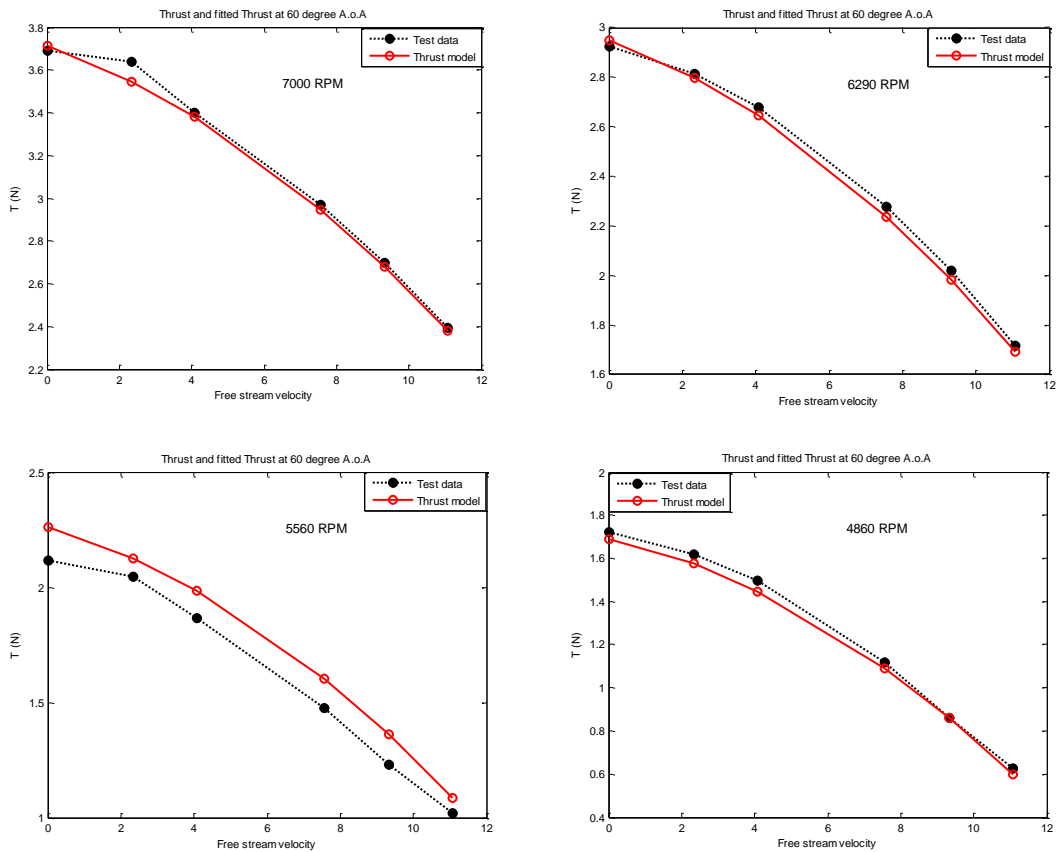


Figure 4.31: Test data and fitted thrust model at 45 degree A.o.A. w.r.t. free stream velocity for different rotor speeds

Test data and fitted thrust model w.r.t. free stream velocity at 60 degree A.o.A. at different rotor speeds are as follows:



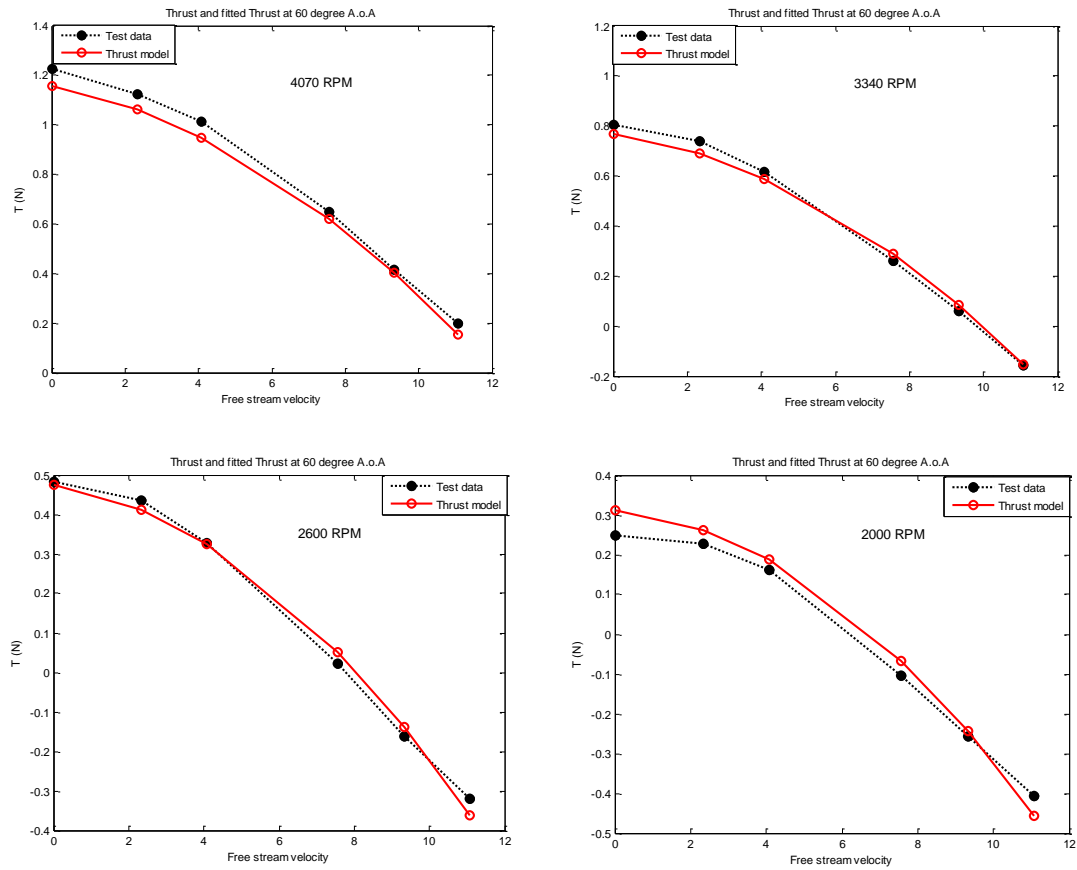


Figure 4.32: Test data and fitted thrust model at 60 degree A.o.A. w.r.t. free stream velocity for different rotor speeds

As it can be seen clearly in the following figures, as the wind tunnel speed increases thrust force decreases:

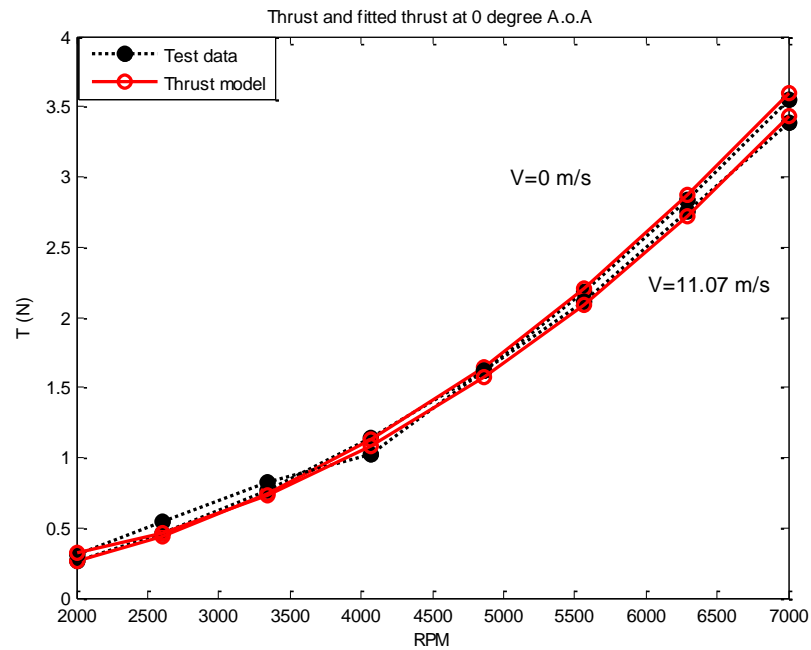


Figure 4.33: Test data and thrust model at 0 degree A.o.A. for different wind speeds

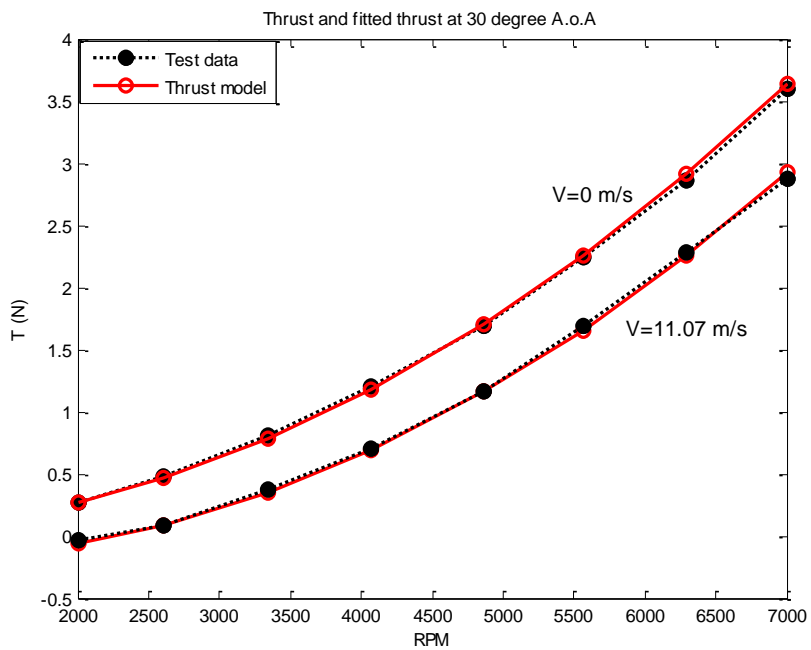


Figure 4.34: Test data and thrust model at 30 degree A.o.A. for different wind speeds

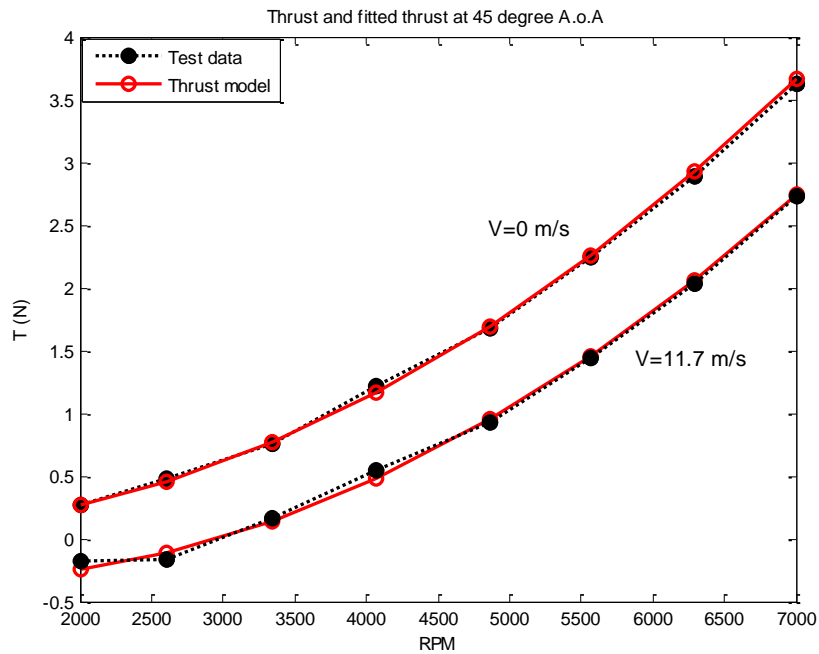


Figure 4.35: Test data and thrust model at 45 degree A.o.A. for different wind speeds

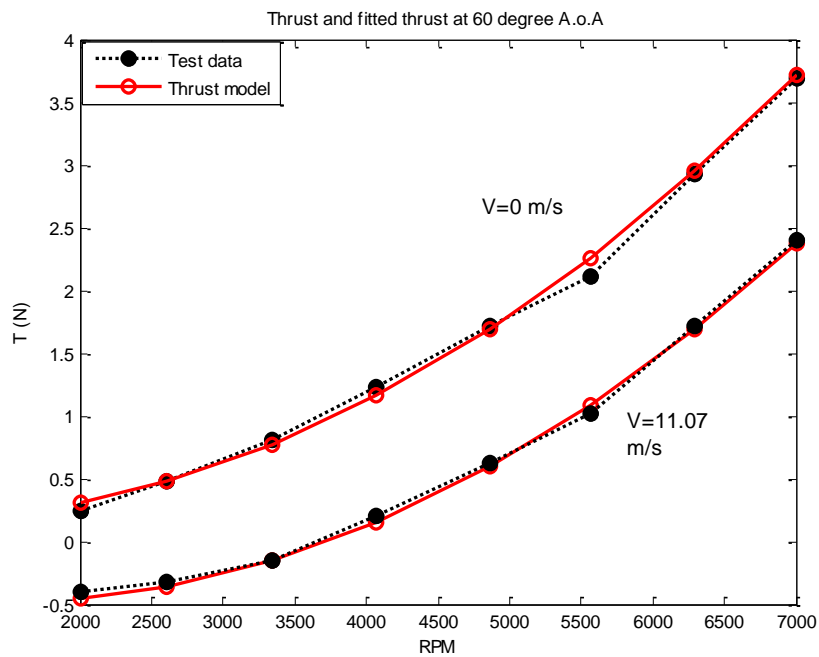


Figure 4.36: Test data and thrust model at 60 degree A.o.A. for different wind speeds

For parameter estimation of hub force, same relation is generated between hub force, free stream velocity, and angular velocity of the rotor at different angles of attack:

$$H(\alpha, V, \Omega) = p_{00}(\alpha) + p_{10}(\alpha)V + p_{01}(\alpha)\Omega + p_{20}(\alpha)V^2 + p_{11}(\alpha)\Omega V + p_{02}(\alpha)\Omega^2$$

Table 4.13: Coefficients of hub force at different angles of attack

	0°	30°	45°	60°
p_{00}	-0.0067	0.04094	-0.01909	0.01527
p_{10}	-0.0158	-0.006017	0.002209	0.001824
p_{01}	3.647e-06	-3.631e-05	-1.137e-05	-1.676e-05
p_{20}	0.0001847	0.001403	0.0006506	0.0004421
p_{11}	6.875e-06	4.322e-06	1.012e-06	-3.223e-07
p_{02}	3.883e-09	8.853e-09	6.718e-09	7.081e-09

Test data and fitted hub force model graphs in 3D using surface fitting at 60, 45, 30, and 0 degrees are as follows:

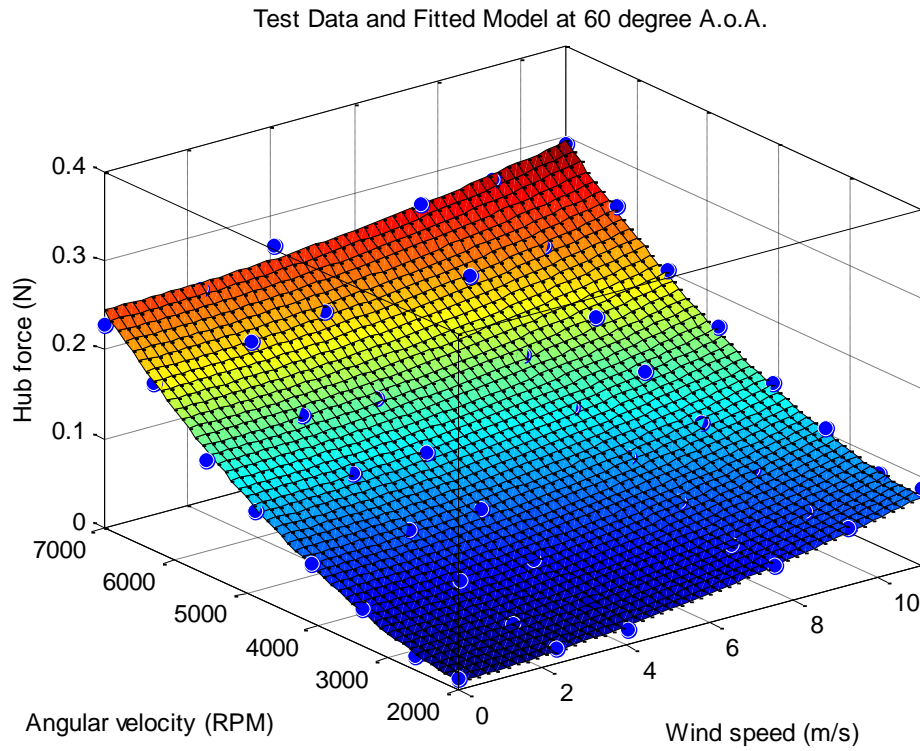


Figure 4.37: Surface fitting at 60 degree A.o.A. for hub force

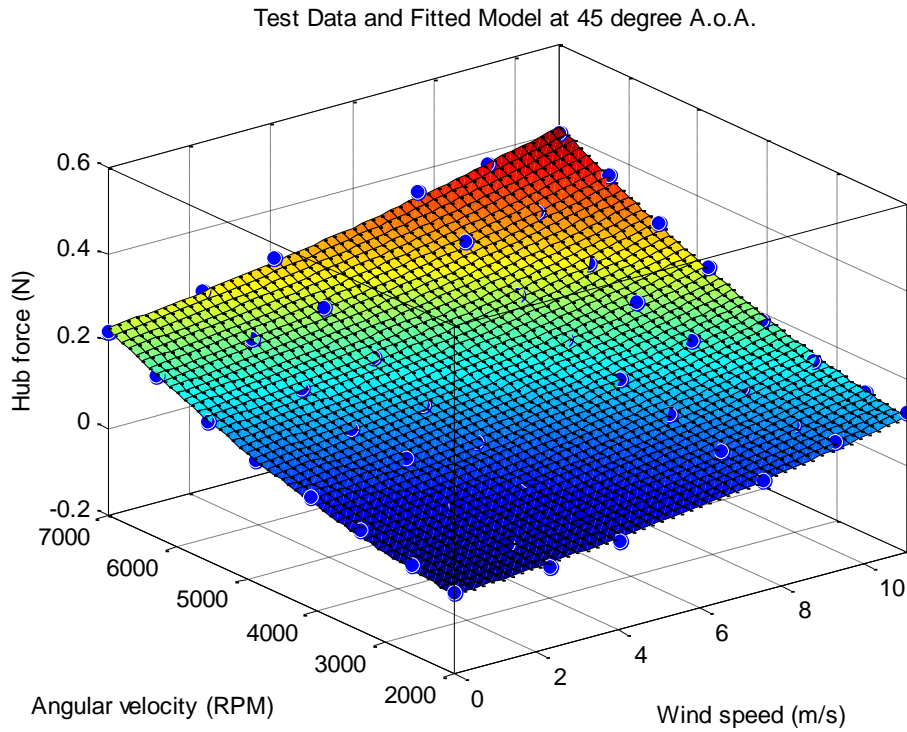


Figure 4.38: Surface fitting at 45 degree A.o.A. for hub force

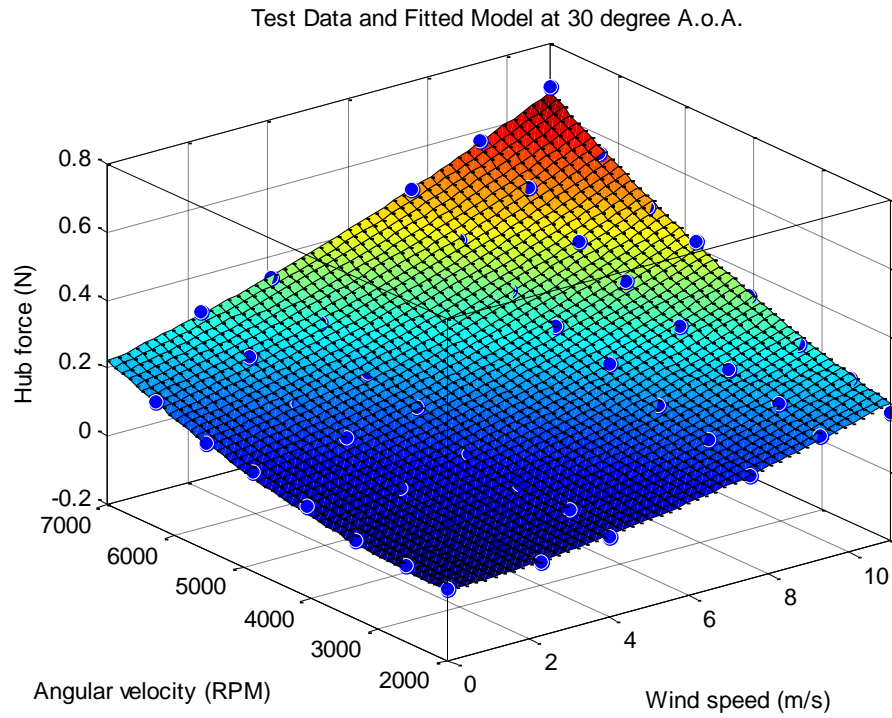


Figure 4.39: Surface fitting at 30 degree A.o.A. for hub force

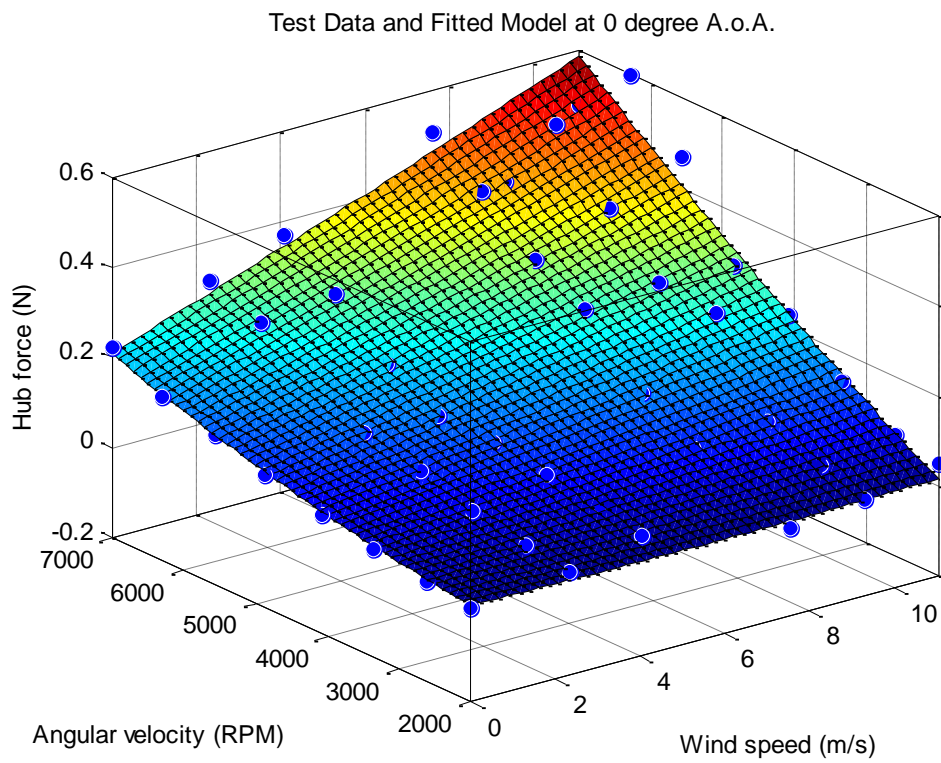


Figure 4.40: Surface fitting at 0 degree A.o.A. for hub force

Test data and fitted hub force model w.r.t. angular velocity of the rotor at 0 degree A.o.A. at different wind tunnel speeds are as follows:

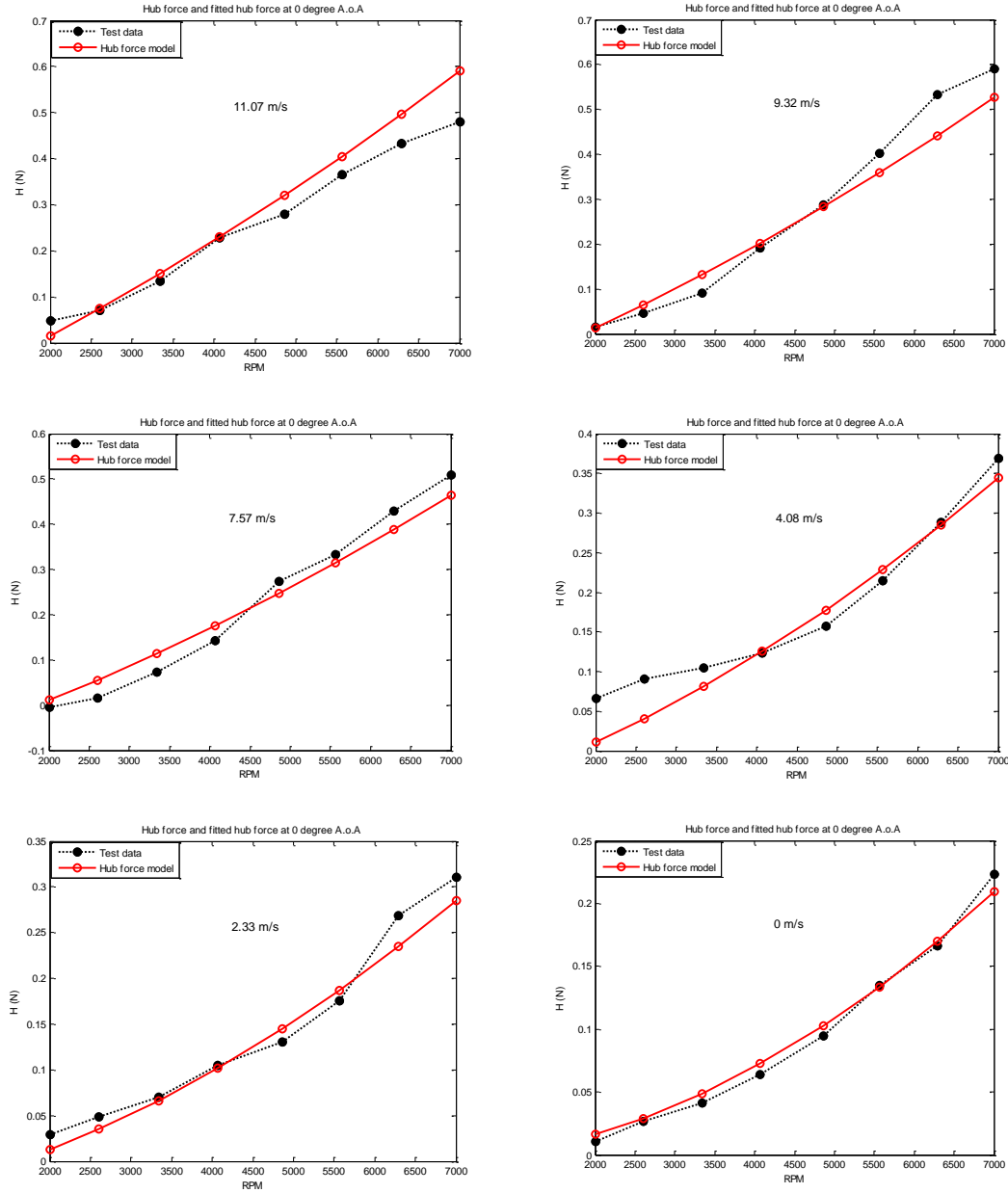


Figure 4.41: Test data and fitted hub force model at 0 degree A.o.A. w.r.t. the angular velocity of the rotor for different wind speeds

Test data and fitted hub force model w.r.t. angular velocity of the rotor at 30 degree A.o.A. at different wind tunnel speeds are as follows:

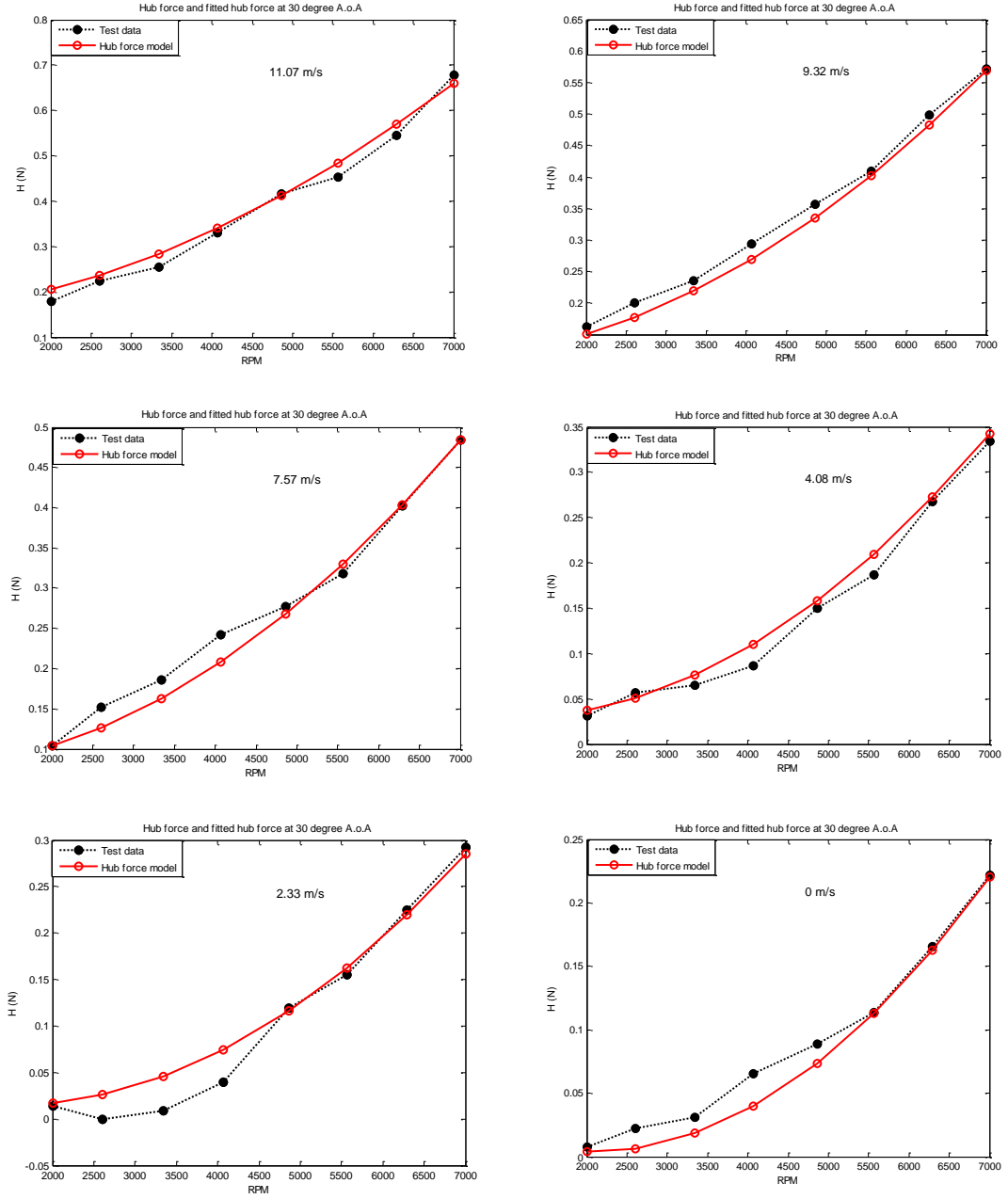


Figure 4.42: Test data and fitted hub force model at 30 degree A.o.A. w.r.t. the angular velocity of the rotor for different wind speeds

Test data and fitted hub force model w.r.t. angular velocity of the rotor at 45 degree A.o.A. at different wind tunnel speeds are as follows:

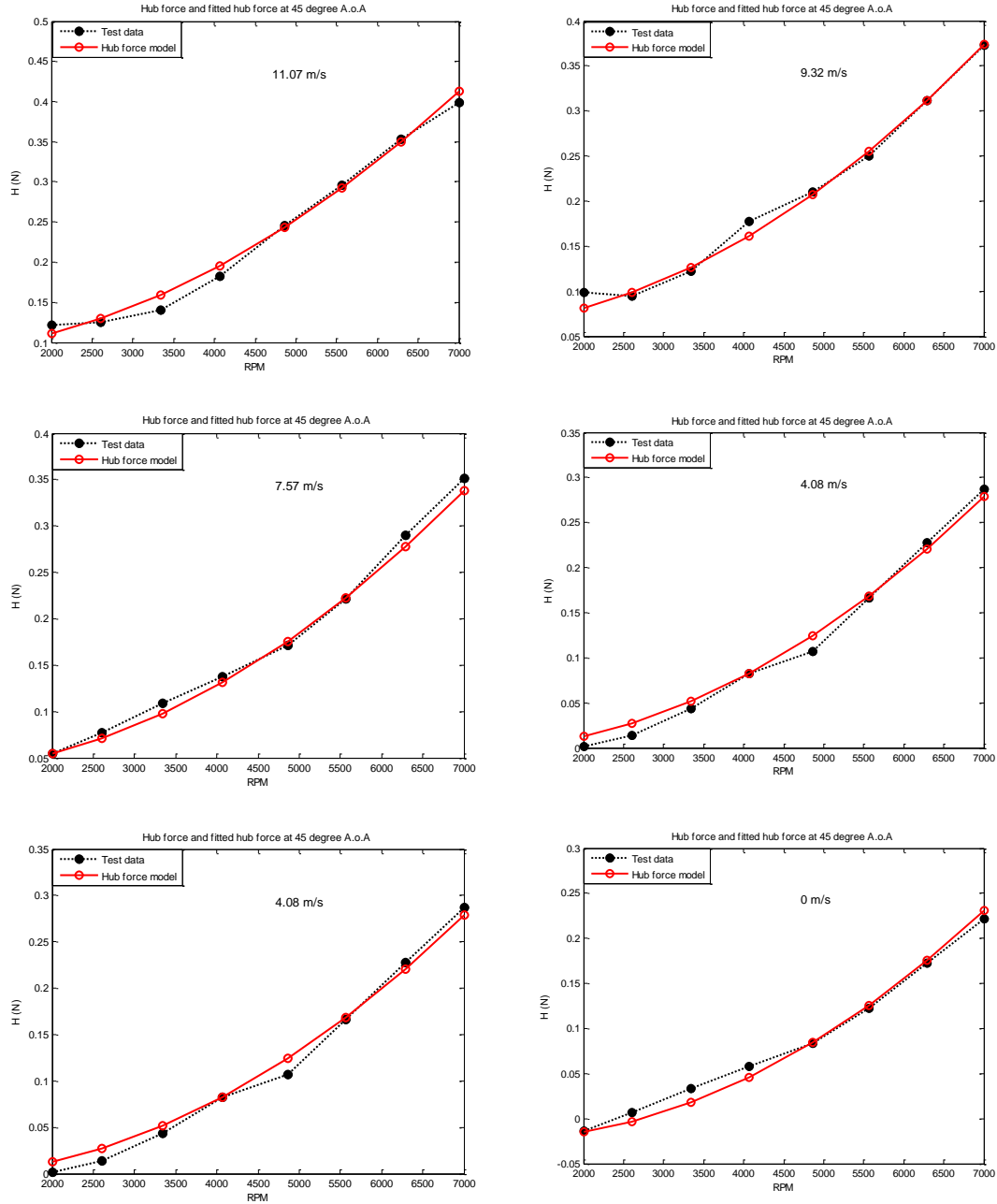


Figure 4.43: Test data and fitted hub force model at 45 degree A.o.A. w.r.t. the angular velocity of the rotor for different wind speeds

Test data and fitted hub force model w.r.t. angular velocity of the rotor at 60 degree A.o.A. at different wind tunnel speeds are as follows:

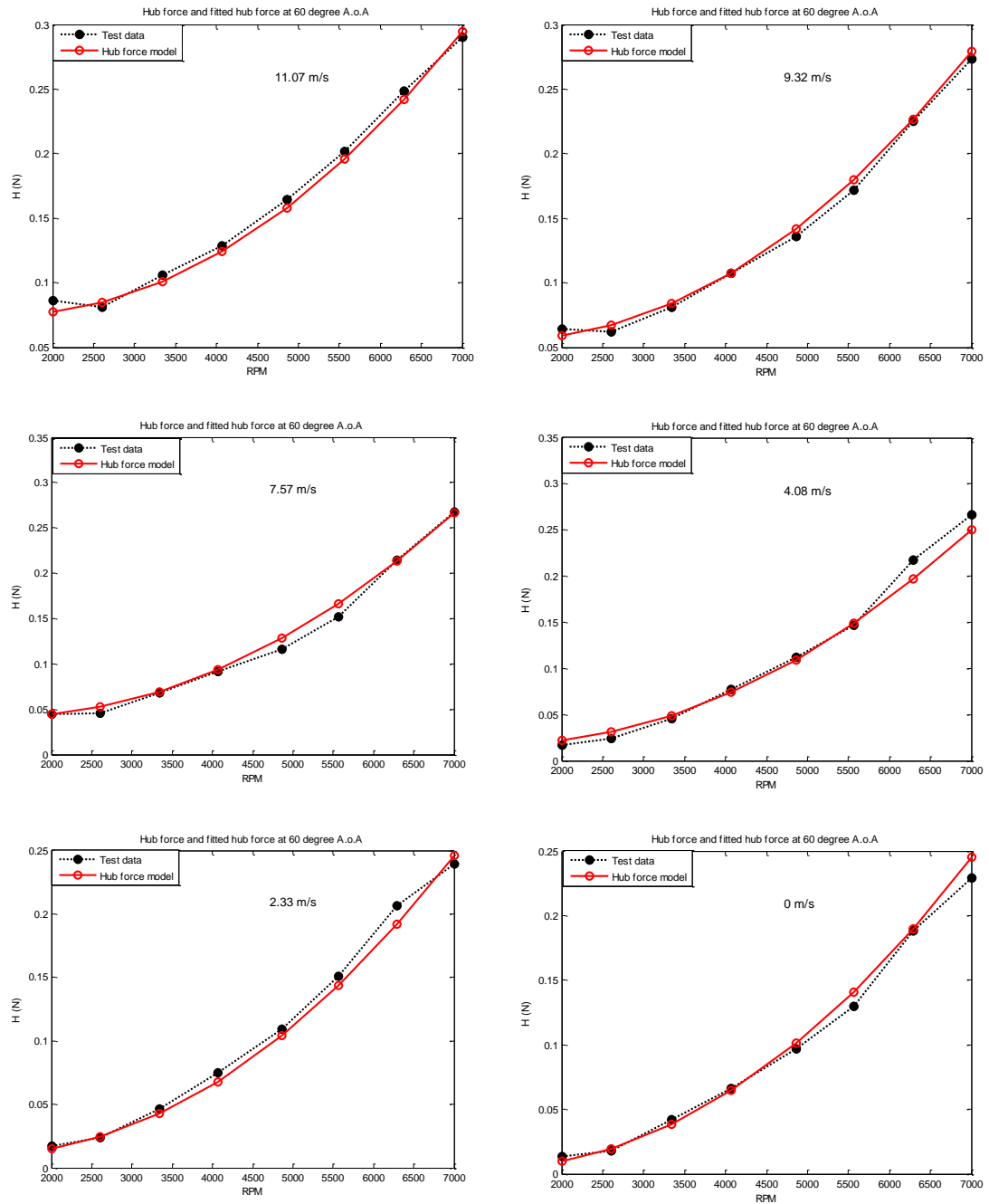
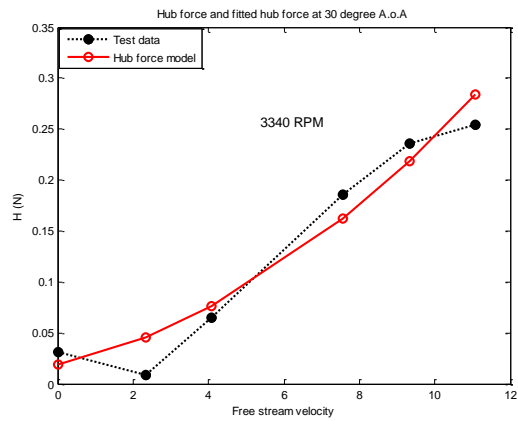
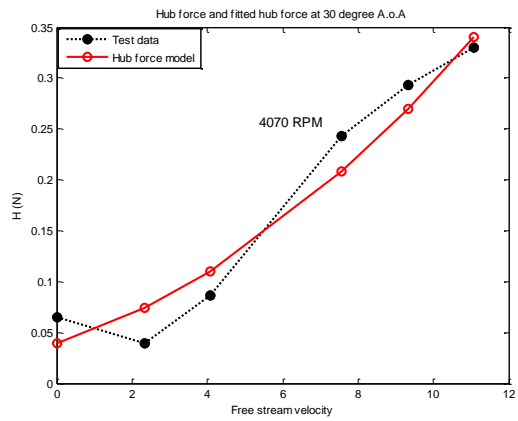
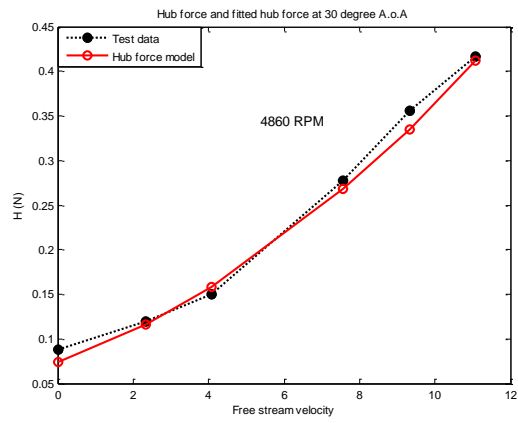
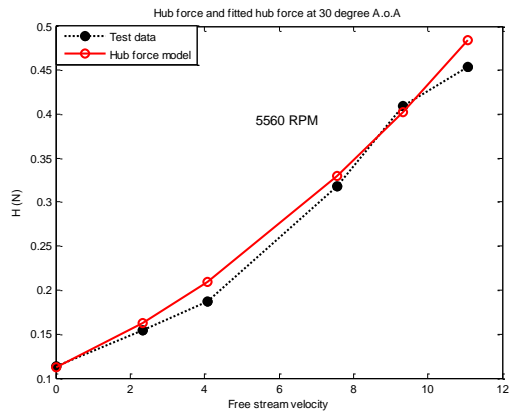
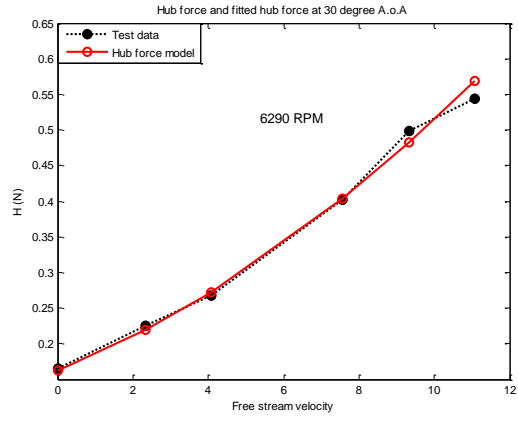
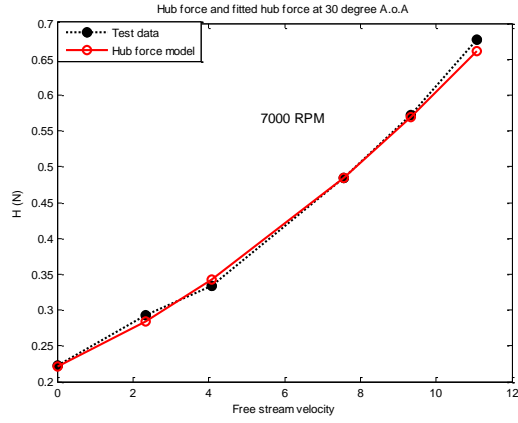


Figure 4.44: Test data and fitted hub force model at 60 degree A.o.A. w.r.t. the angular velocity of the rotor for different wind speeds

Test data and fitted hub force model w.r.t. free stream velocity at 30 degree A.o.A. at different rotor speeds are as follows:



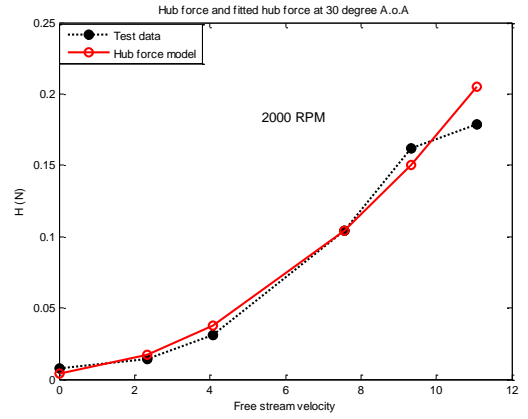
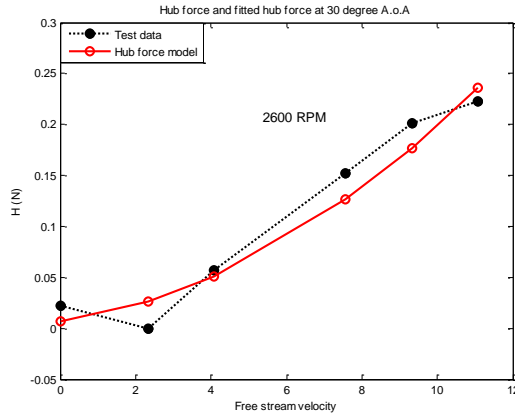
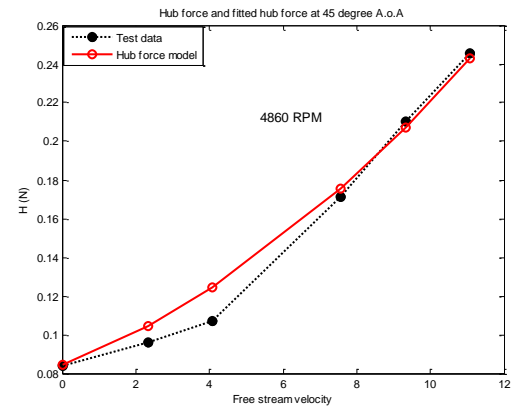
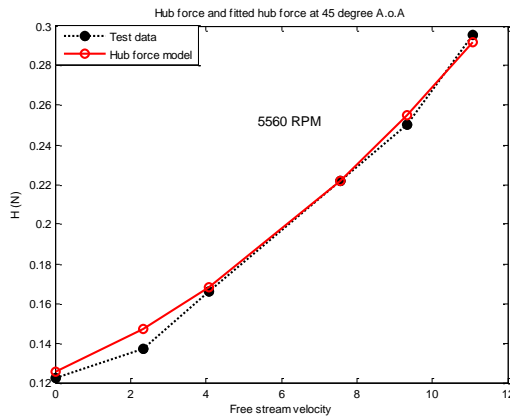
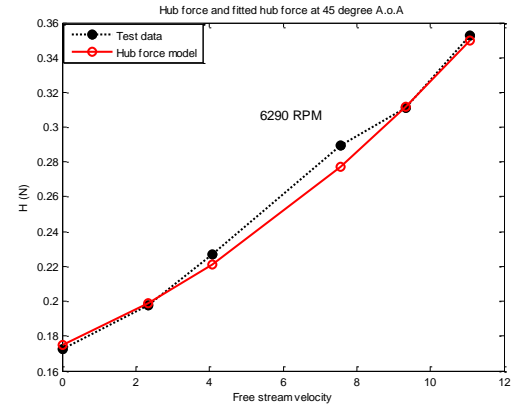
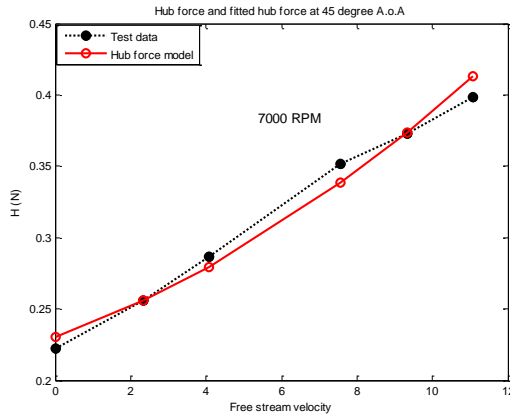


Figure 4.45: Test data and fitted hub force model at 30 degree A.o.A. w.r.t. free stream velocity for different rotor speeds

Test data and fitted hub force model w.r.t. free stream velocity at 45 degree A.o.A. at different rotor speeds are as follows:



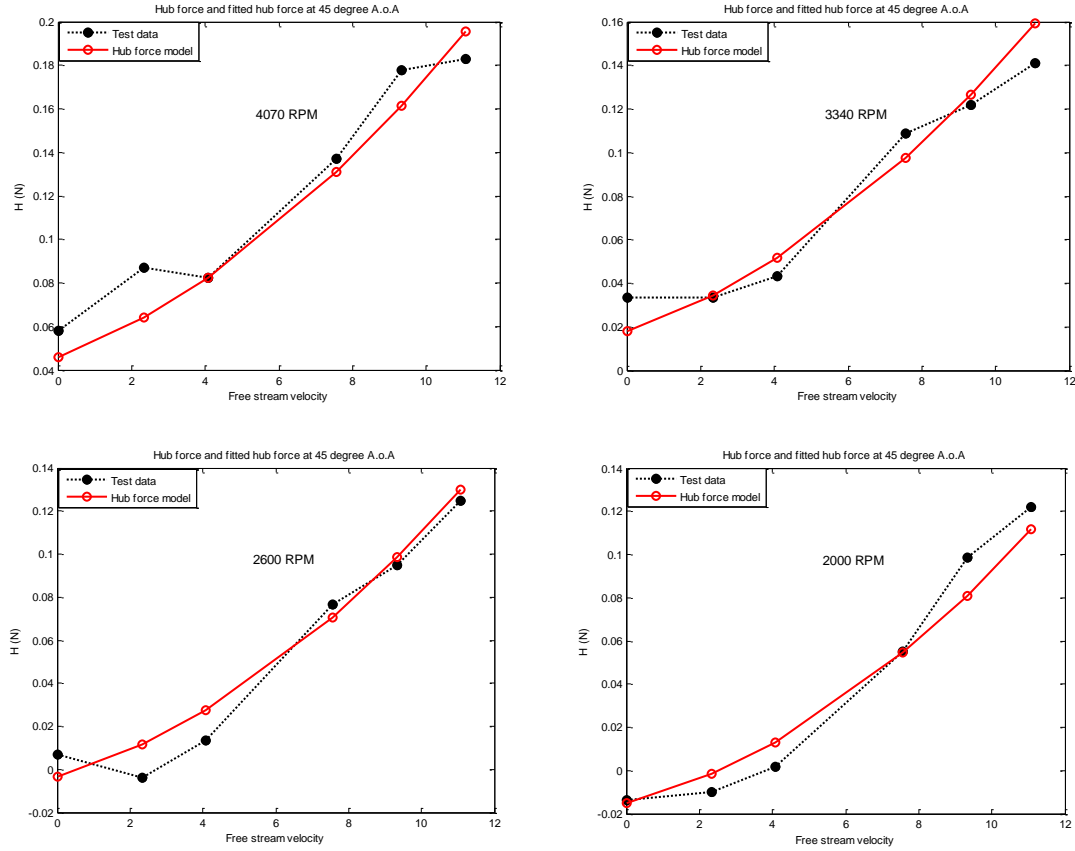


Figure 4.46: Test data and fitted hub force model at 45 degree A.o.A. w.r.t. free stream velocity for different rotor speeds

By using the surface fitting, the relation between rotor torque, free stream velocity, and angular velocity of the rotor is as follows:

$$Q(\alpha, V, \Omega) = p_{00}(\alpha) + p_{10}(\alpha)V + p_{01}(\alpha)\Omega + p_{20}(\alpha)V^2 + p_{11}(\alpha)\Omega V + p_{02}(\alpha)\Omega^2$$

Table 4.14: Coefficients of rotor torque at different angles of attack

	0°	30°	45°	60°	90°
p_{00}	0.002484	-0.009685	0.0008261	-0.01154	0.03847
p_{10}	0.001712	9.427e-06	-0.000215	-0.0006291	-0.0002151
p_{01}	-2.419e-06	5.836e-06	-8.572e-07	6.629e-06	-1.216e-05
p_{20}	-4.511e-05	-0.0001164	-1.717e-05	-8.159e-06	-3.516e-05
p_{11}	-5.299e-07	-1.091e-07	-1.057e-07	-7.361e-08	6.557e-08
p_{02}	2.219e-09	1.25e-09	1.958e-09	1.209e-09	2.215e-09

Test data and fitted rotor torque model using surface fitting at 60, 45, 30, and 0 degrees are as follows:

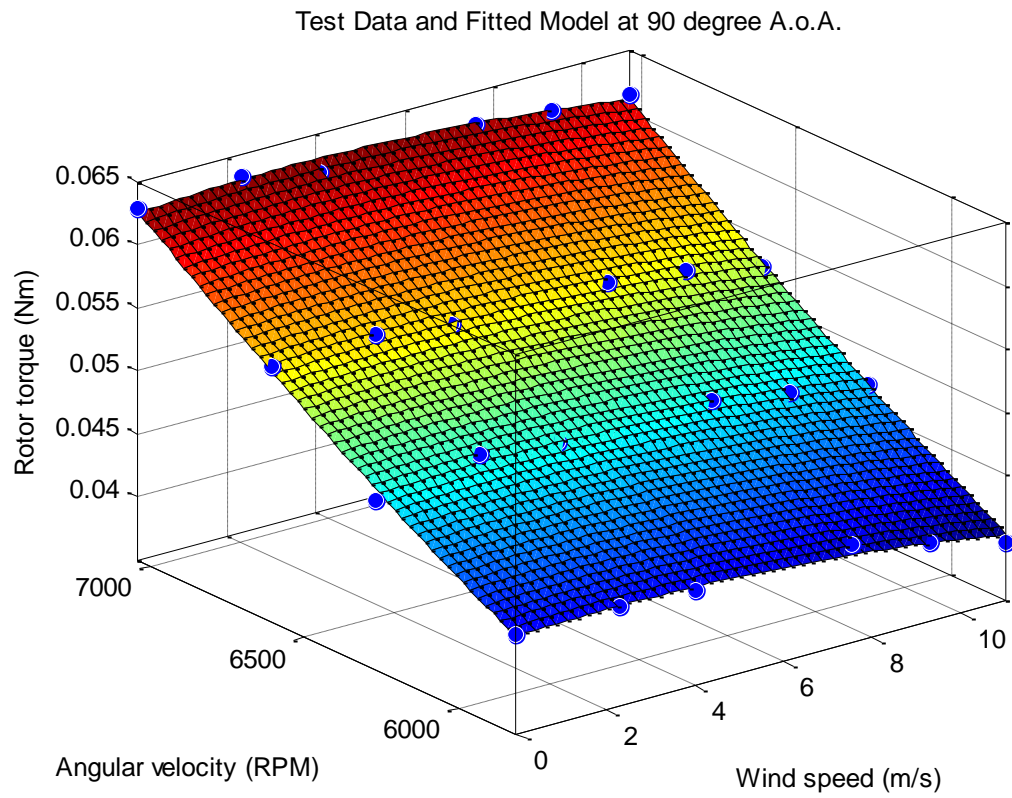


Figure 4.47: Surface fitting at 90 degree A.o.A. for rotor torque

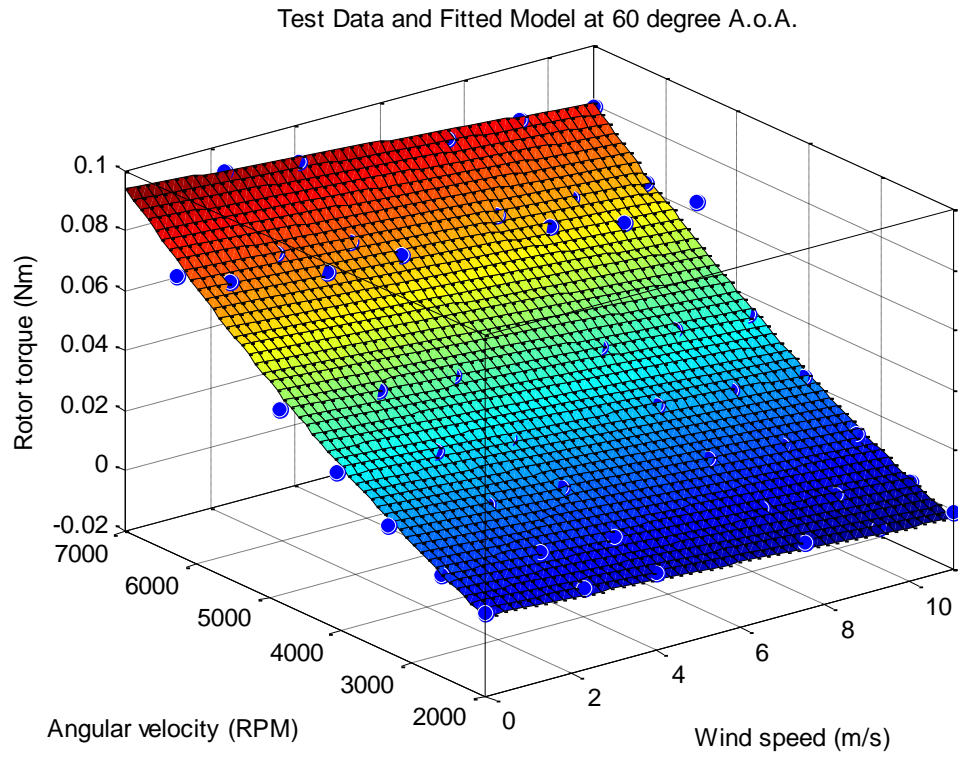


Figure 4.48: Surface fitting at 60 degree A.o.A. for rotor torque

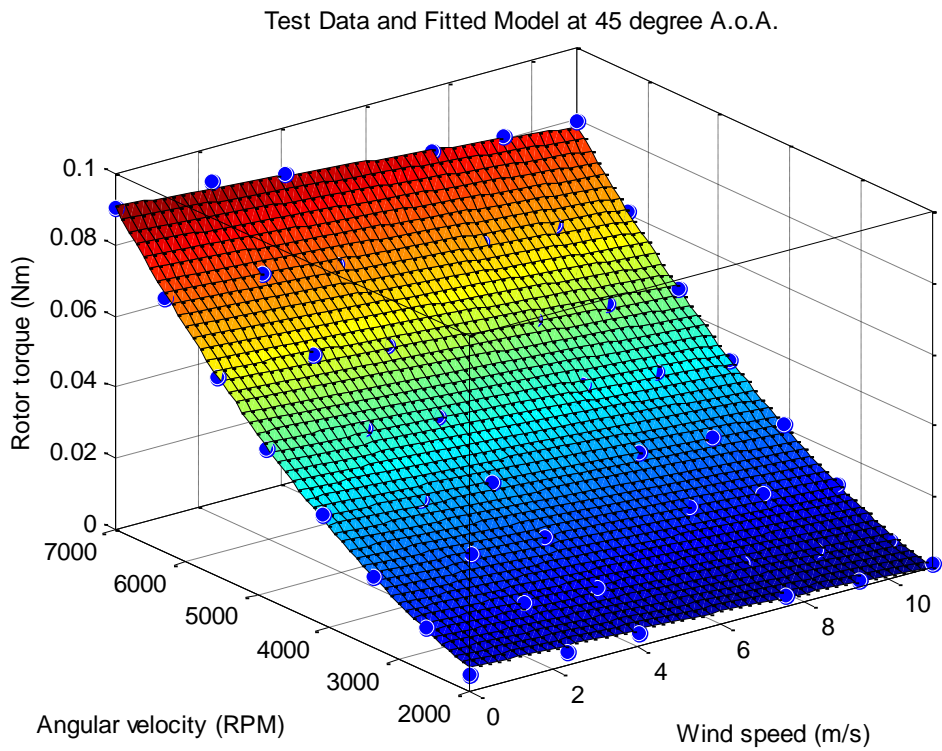


Figure 4.49: Surface fitting at 45 degree A.o.A. for rotor torque

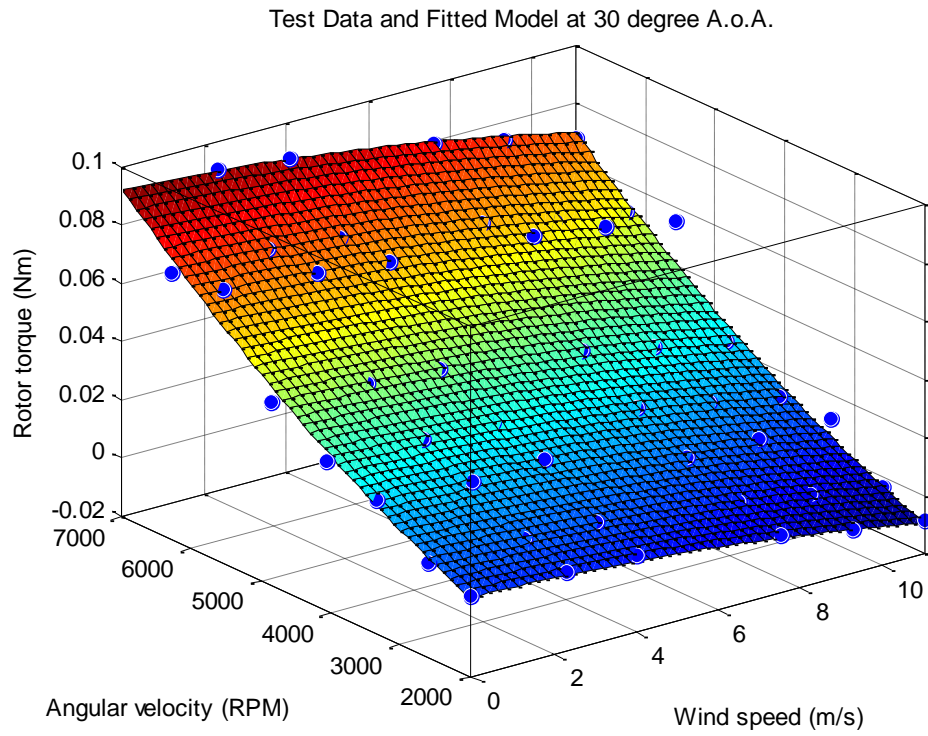


Figure 4.50: Surface fitting at 30 degree A.o.A. for rotor torque

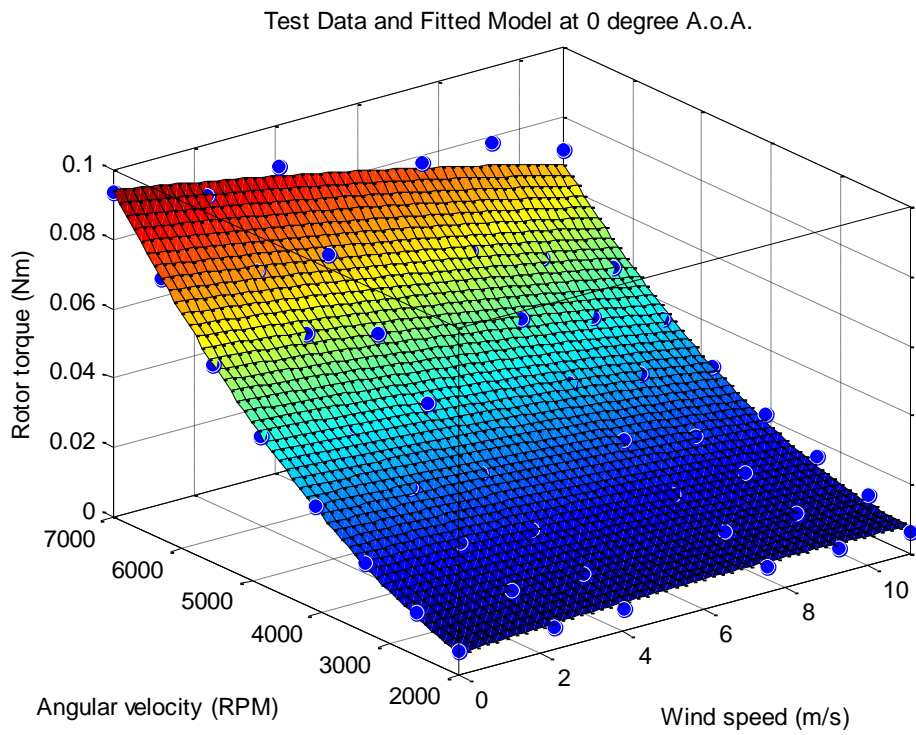


Figure 4.51: Surface fitting at 0 degree A.o.A. for rotor torque

Test data and fitted rotor torque model w.r.t. angular velocity of the rotor at 0 degree A.o.A. at different wind speeds are as follows:

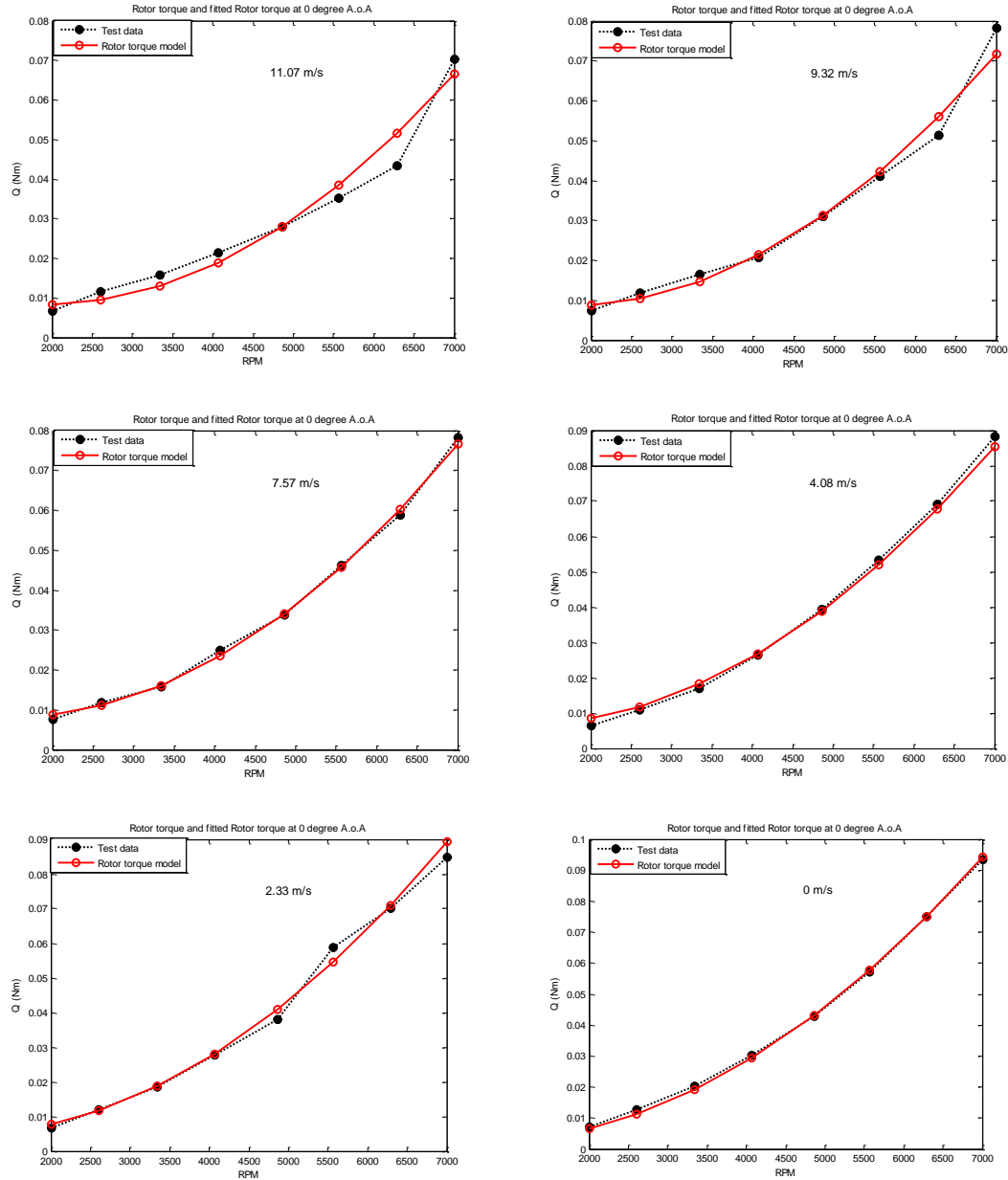


Figure 4.52: Test data and fitted rotor torque model at 0 degree A.o.A. w.r.t. the angular velocity of the rotor for different wind speeds

Test data and fitted rotor torque model w.r.t. angular velocity of the rotor at 30 degree A.o.A. at different wind speeds are as follows:

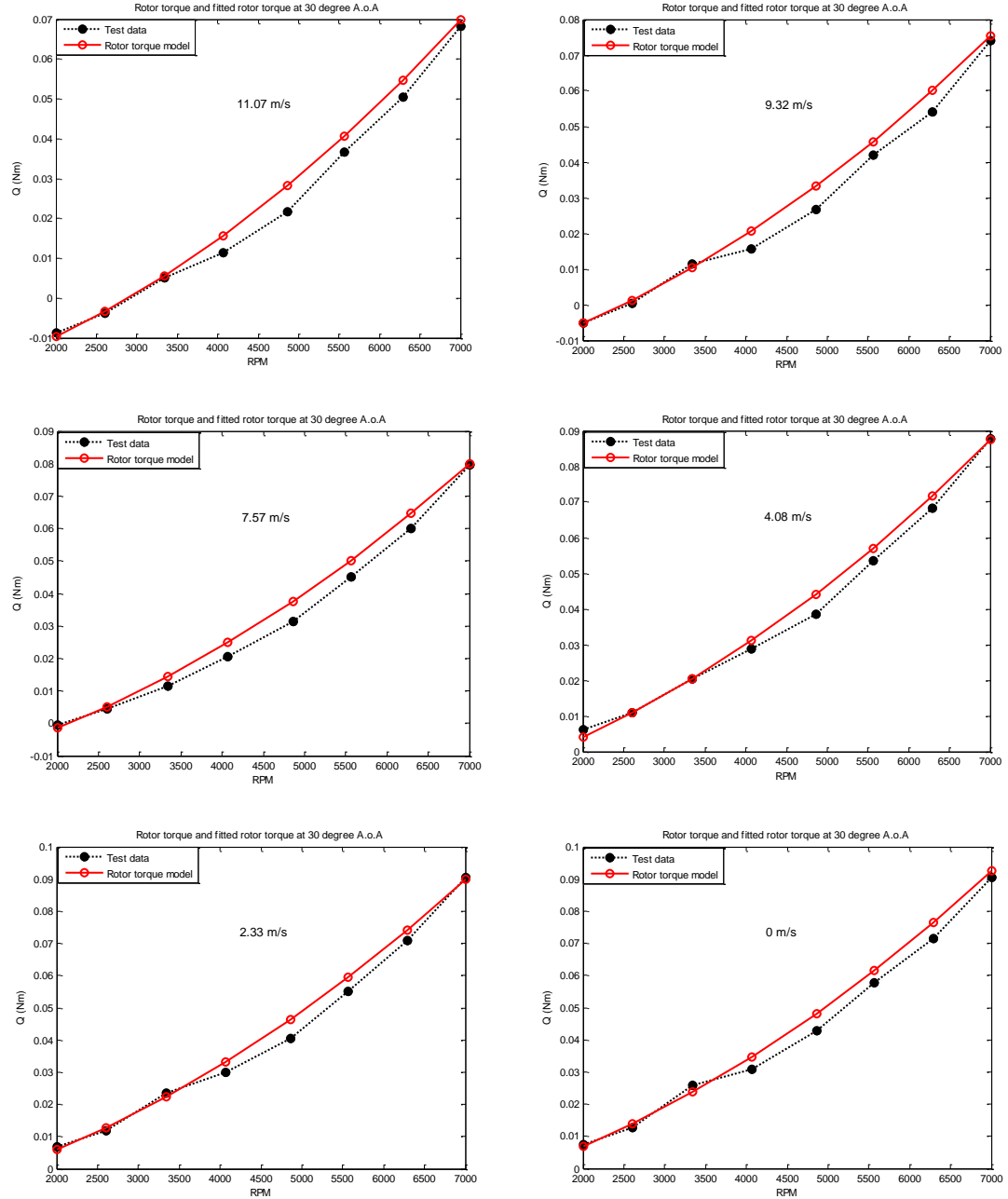


Figure 4.53: Test data and fitted rotor torque model at 30 degree A.o.A. w.r.t. the angular velocity of the rotor for different wind speeds

Test data and fitted rotor torque model w.r.t. angular velocity of the rotor at 45 degree A.o.A. at different wind speeds are as:

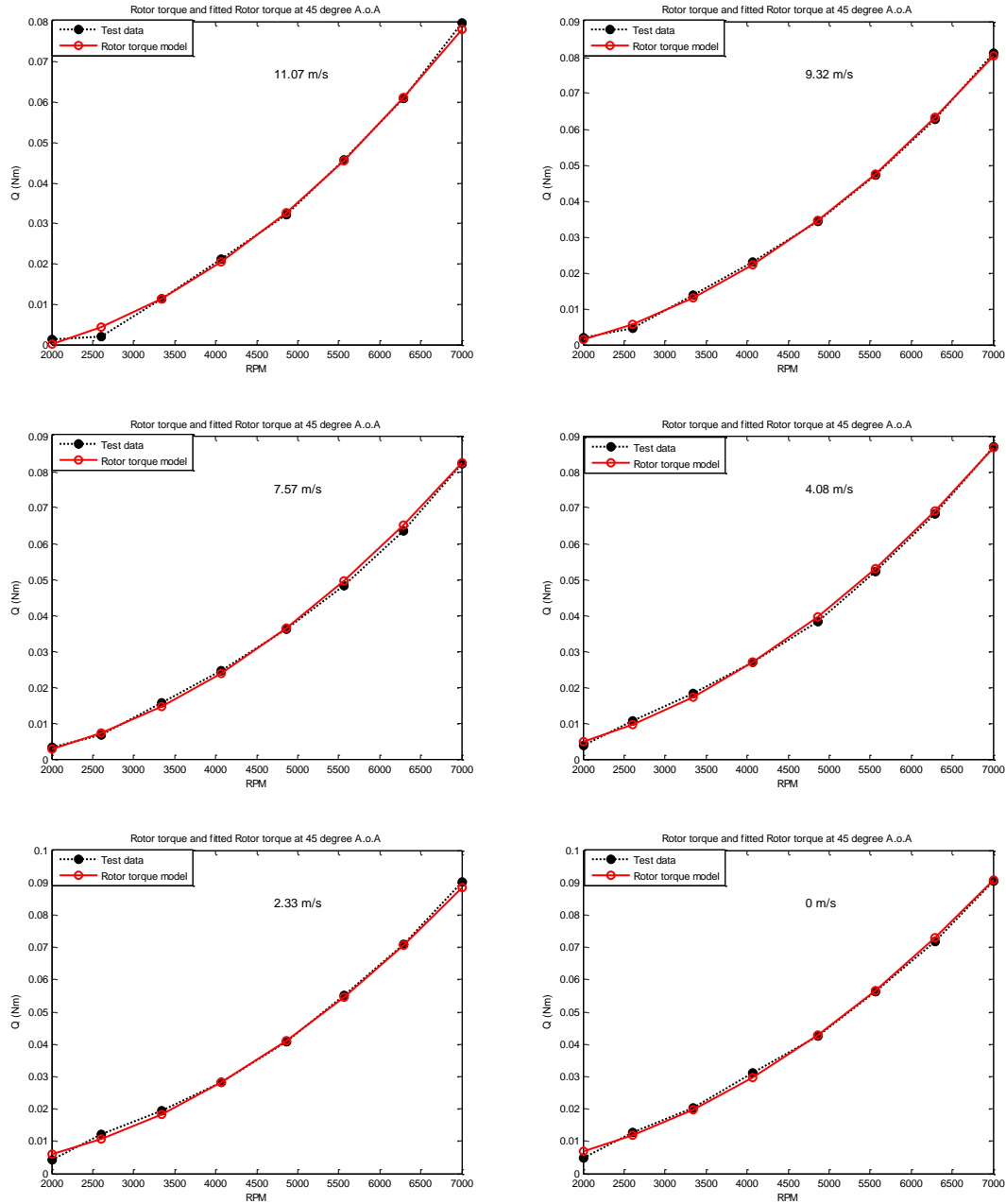


Figure 4.54: Test data and fitted rotor torque model at 45 degree A.o.A. w.r.t. the angular velocity of the rotor for different wind speeds

Test data and fitted rotor torque model w.r.t. angular velocity of the rotor at 60 degree A.o.A. at different wind speeds are as follows:

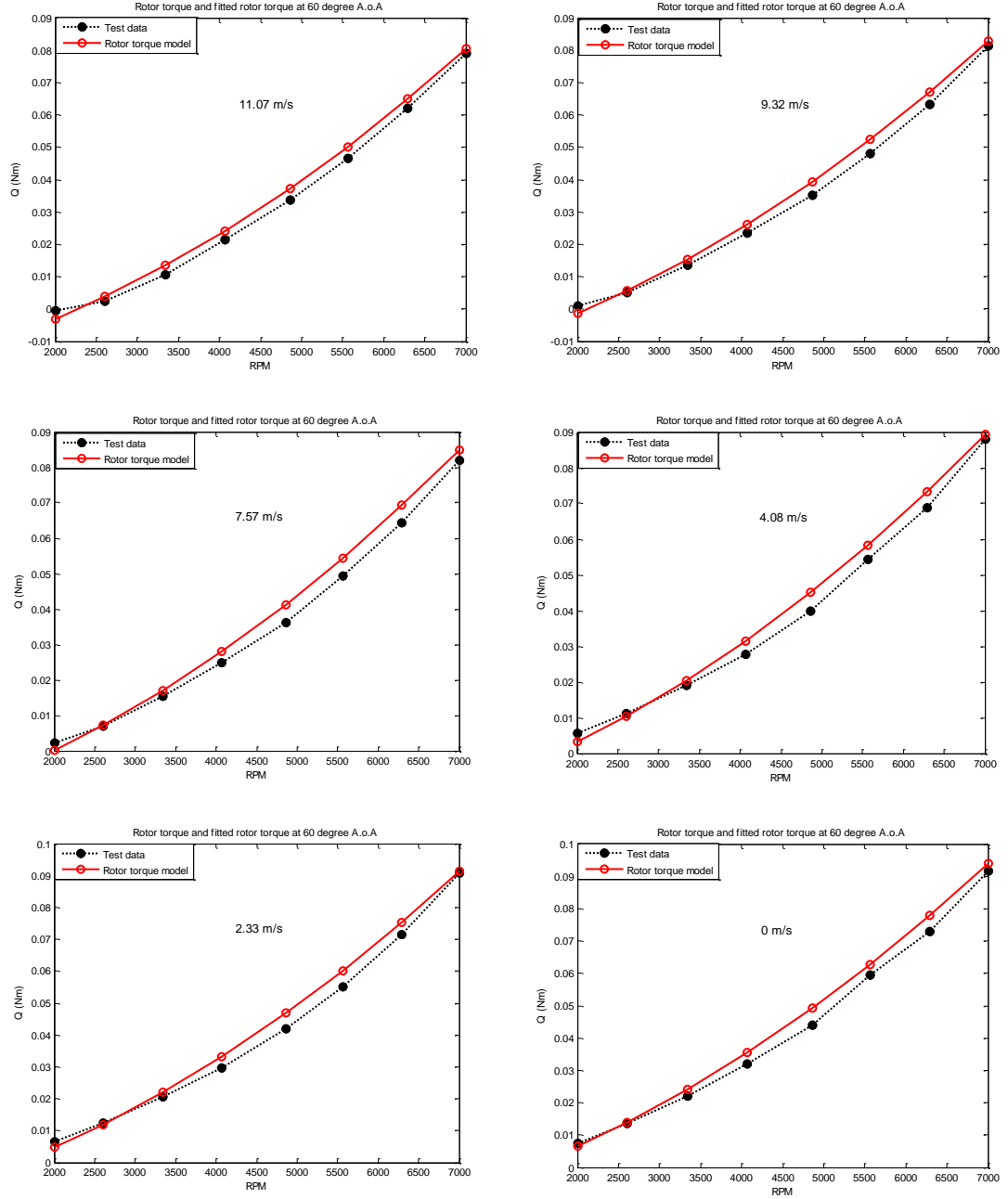


Figure 4.55: Test data and fitted rotor torque model at 60 degree A.o.A. w.r.t. the angular velocity of the rotor for different wind speeds

Rolling moment equation using surface fitting is as:

$$R(\alpha, V, \Omega) = p_{00}(\alpha) + p_{10}(\alpha)V + p_{01}(\alpha)\Omega + p_{20}(\alpha)V^2 + p_{11}(\alpha)\Omega V + p_{02}(\alpha)\Omega^2$$

Table 4.15: Coefficients of rolling moment at different angles of attack

	0°	30°	45°	60°
p_{00}	0.008072	0.01132	0.01441	0.0129
p_{10}	-0.001058	-0.0002215	-0.0007197	-0.0003859
p_{01}	-4.815e-06	-6.903e-06	-6.738e-06	-7.131e-06
p_{20}	0.000105	-1.772e-05	0.0001386	0.0001194
p_{11}	-4.16e-07	-2.139e-07	-2.156e-07	-3.077e-07
p_{02}	1.642e-09	1.784e-09	1.766e-09	1.836e-09

Test data and fitted rolling moment model using surface fitting at 60, 45, 30, and 0 degrees are as follows:

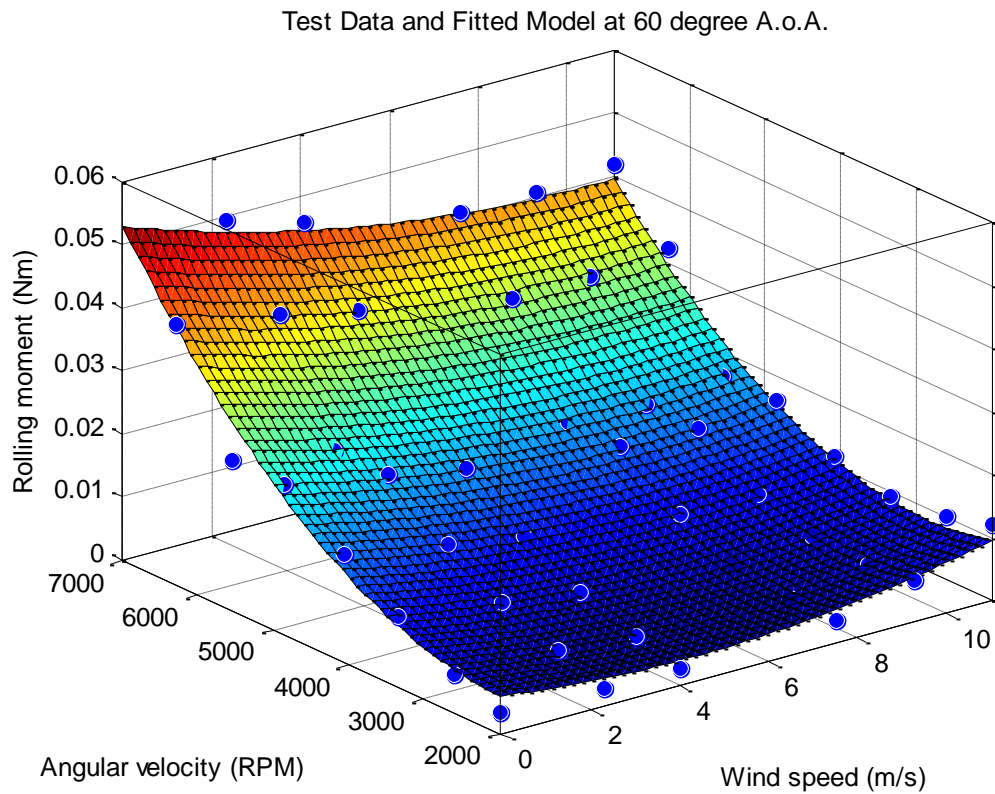


Figure 4.56: Surface fitting at 60 degree A.o.A. for rolling moment

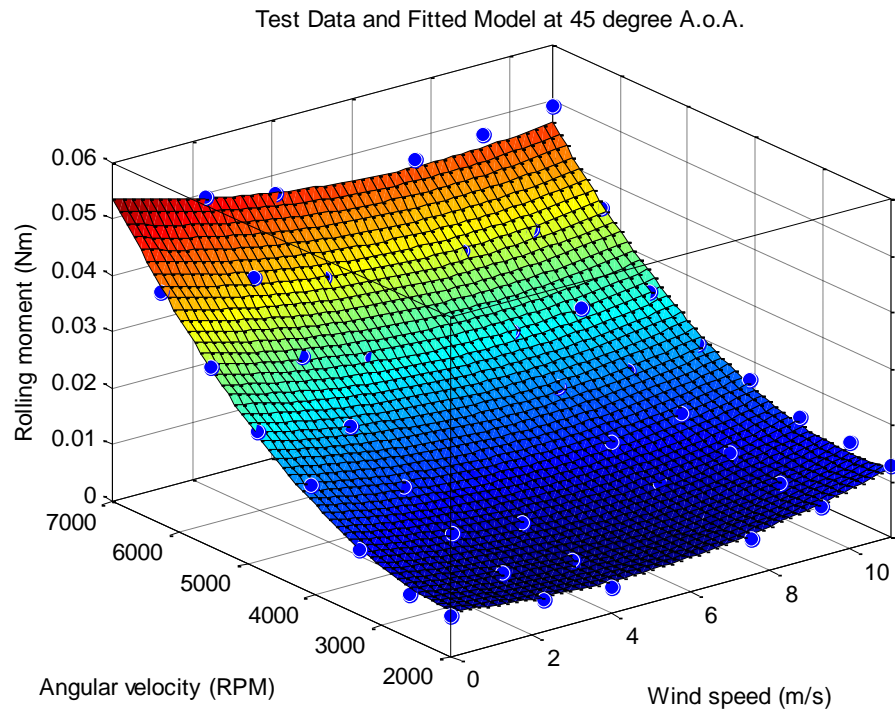


Figure 4.57: Surface fitting at 45 degree A.o.A. for rolling moment

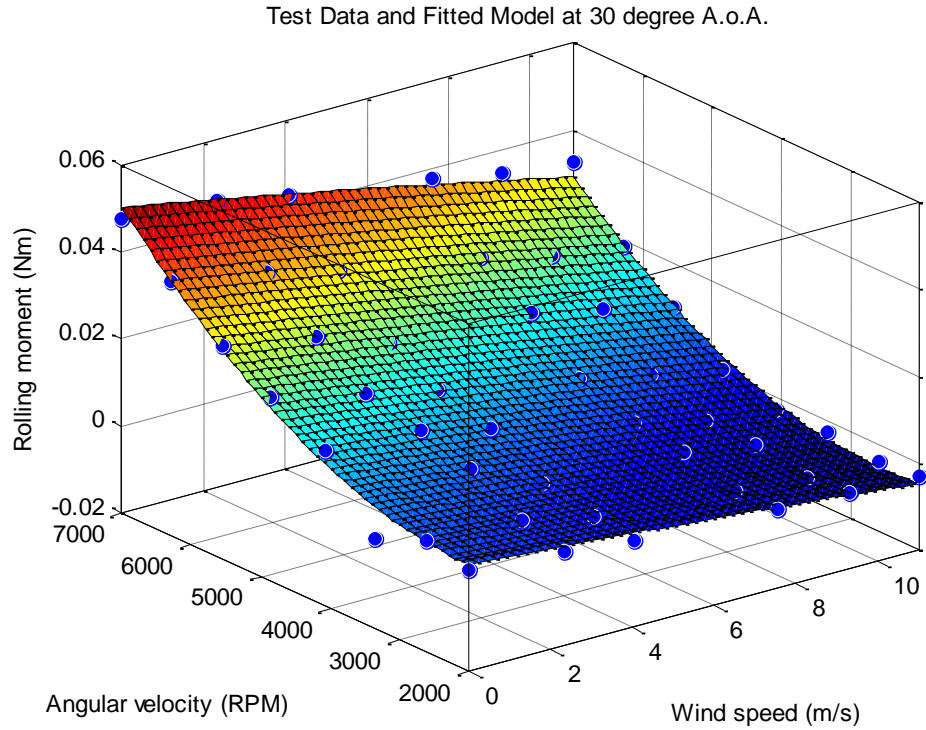


Figure 4.58: Surface fitting at 30 degree A.o.A. for rolling moment

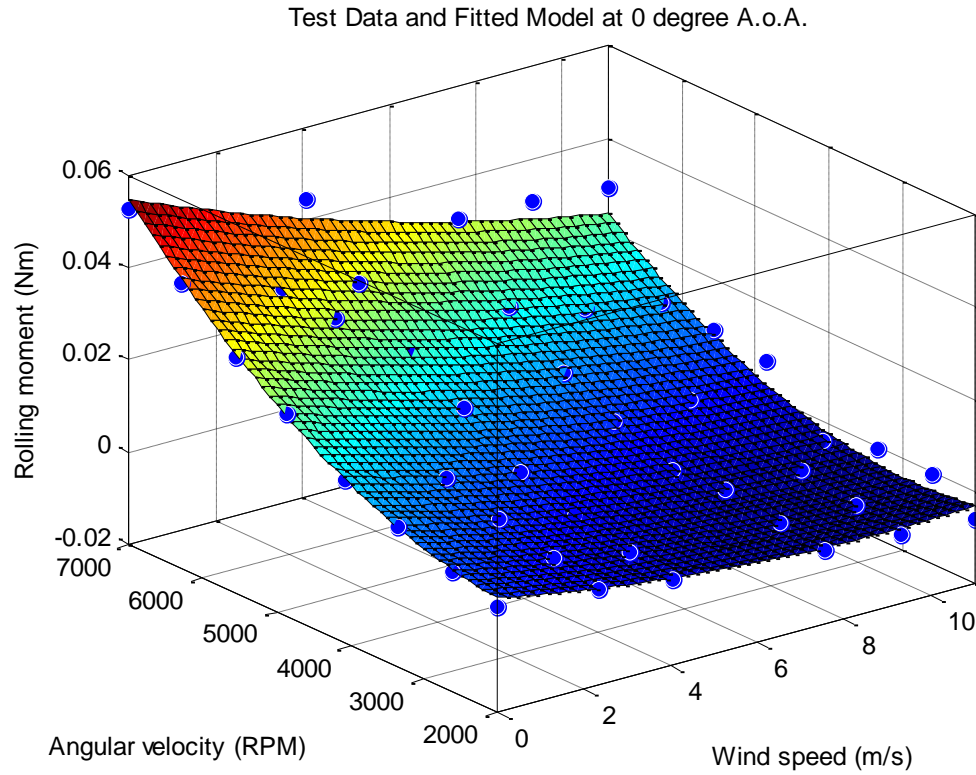
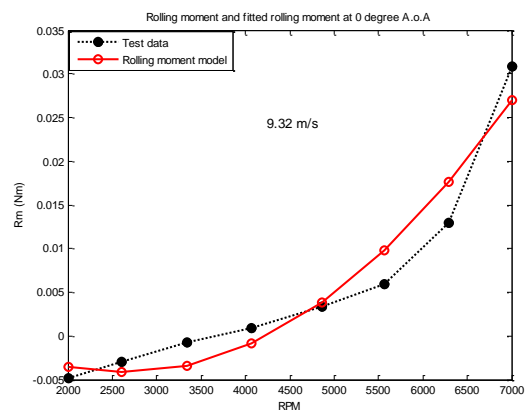
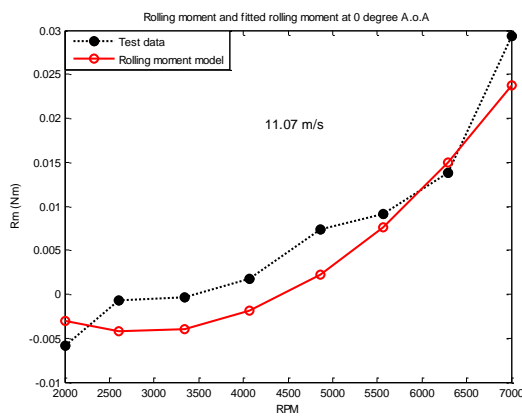


Figure 4.59: Surface fitting at 0 degree A.o.A. for rolling moment

Test data and fitted rolling moment w.r.t. angular velocity of the rotor at 0 degree A.o.A. at different wind tunnel speeds are as follows:



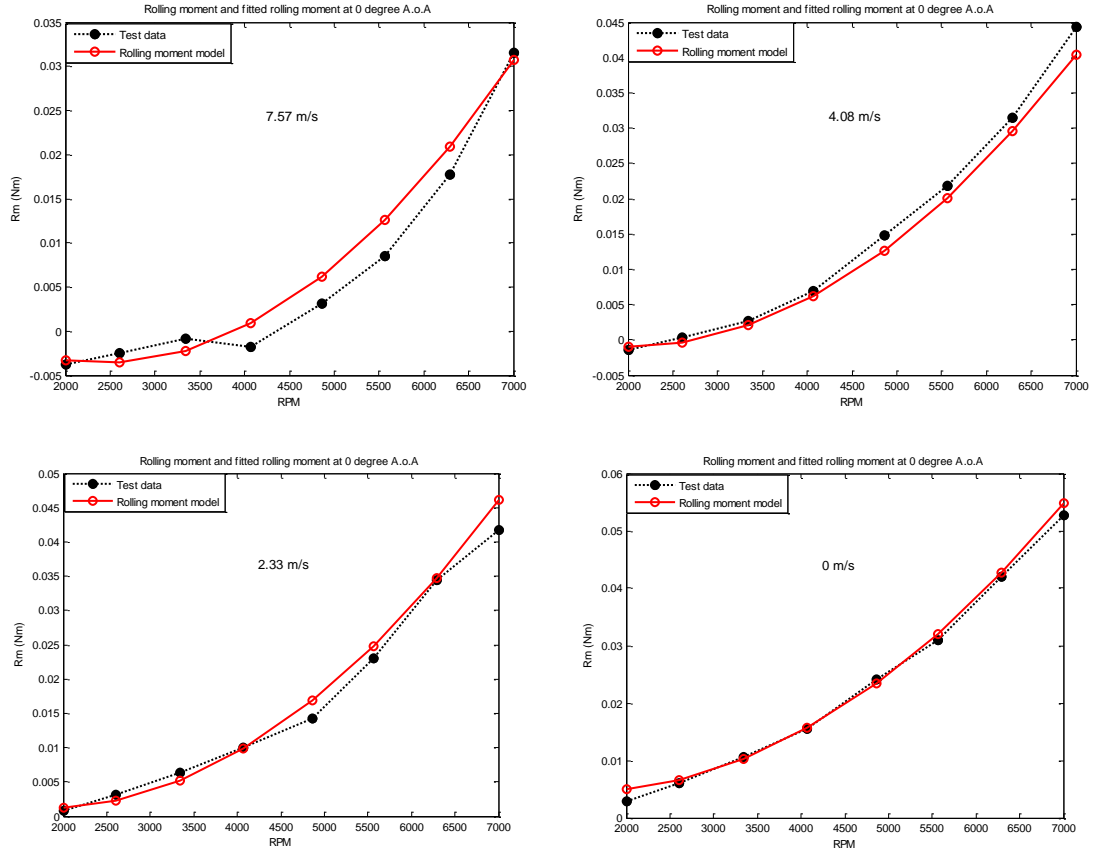
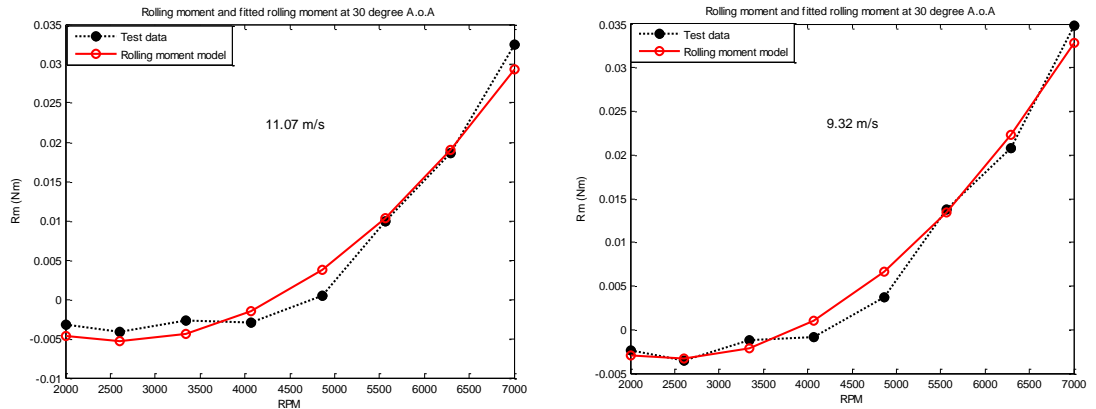


Figure 4.60: Test data and fitted rolling moment model at 0 degree A.o.A. w.r.t. the angular velocity of the rotor for different wind speeds

Test data and fitted rolling moment w.r.t. angular velocity of the rotor at 30 degree A.o.A. at different wind tunnel speeds are as:



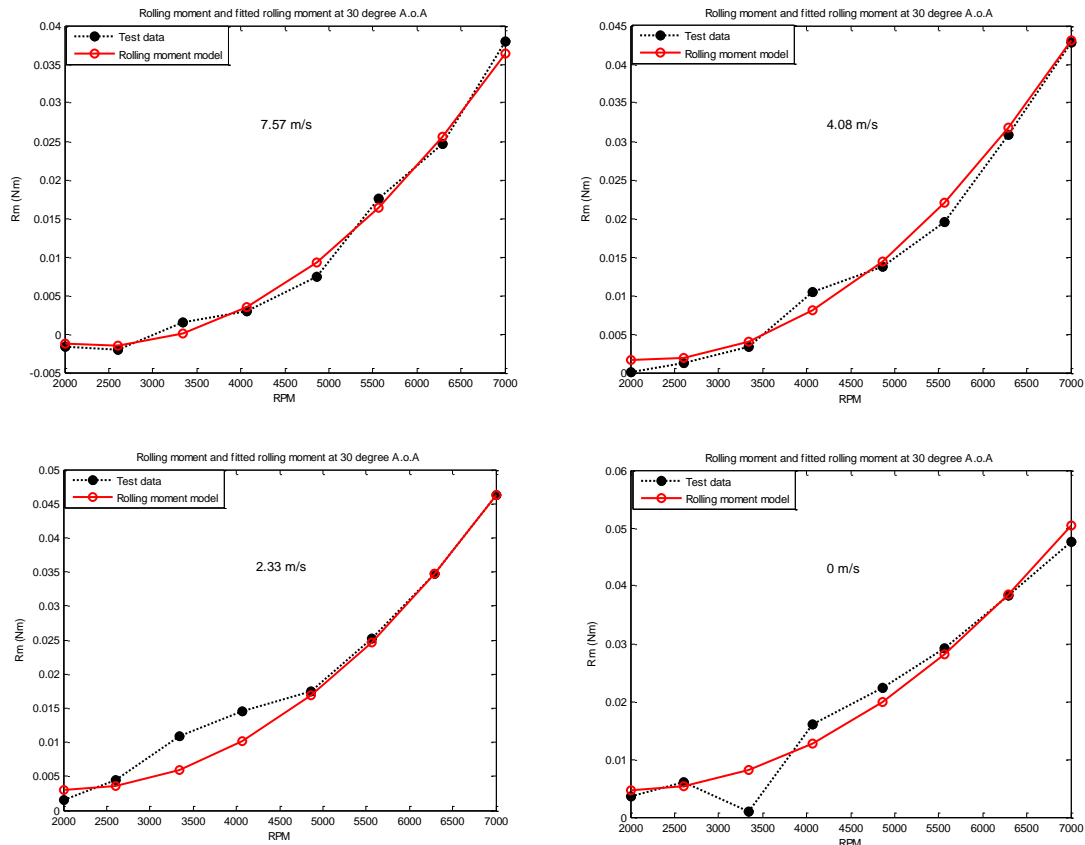
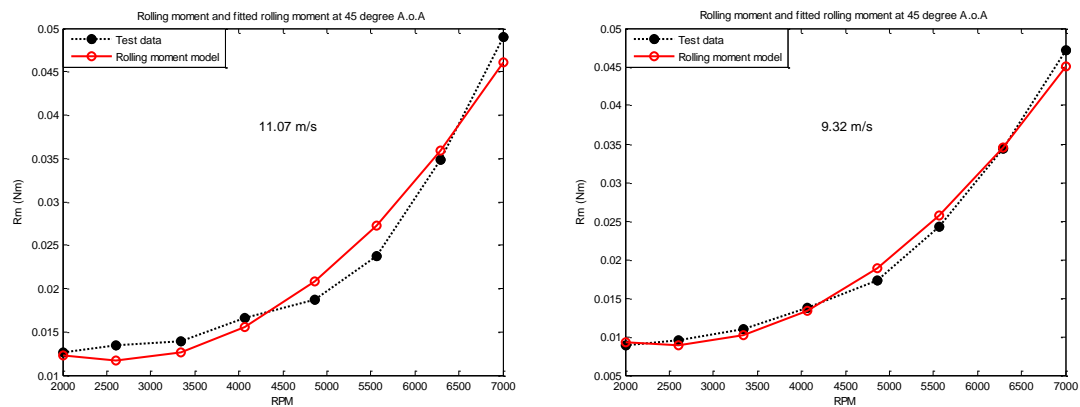


Figure 4.61: Test data and fitted rolling moment model at 30 degree A.o.A. w.r.t. the angular velocity of the rotor for different wind speeds

Test data and fitted rolling moment w.r.t. angular velocity of the rotor at 45 degree A.o.A. at different wind tunnel speeds are as follows:



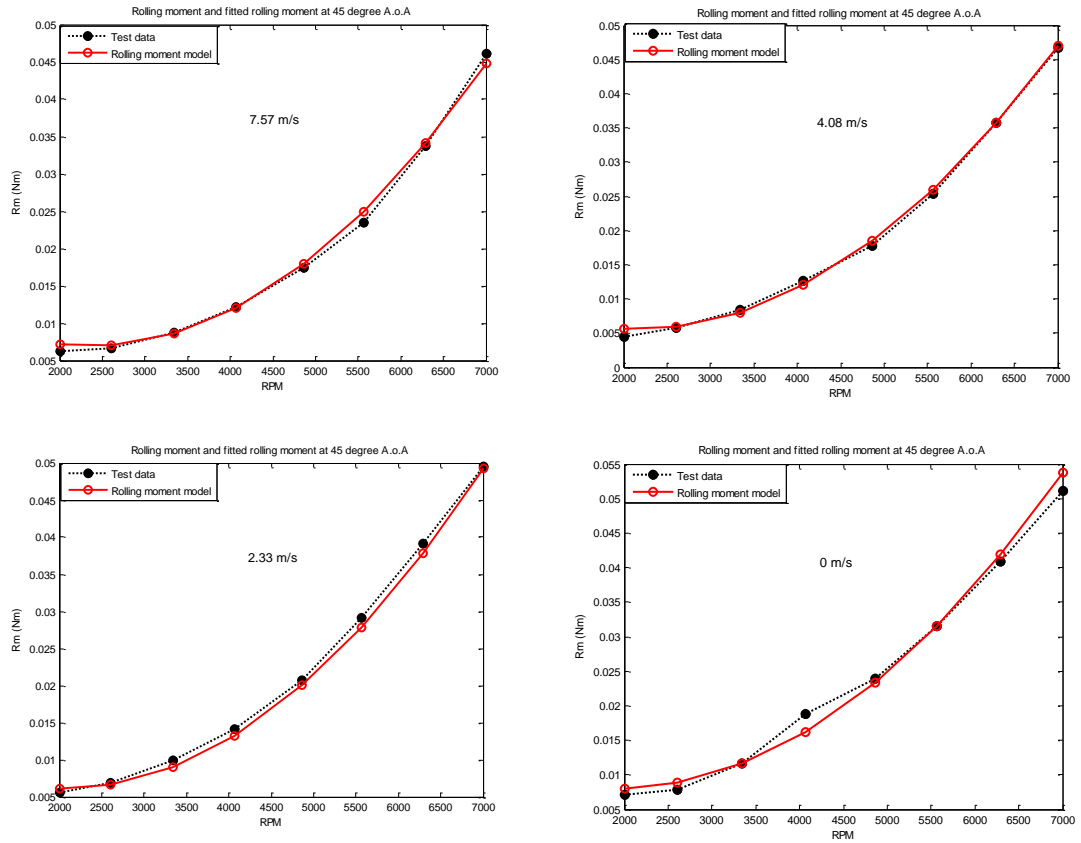
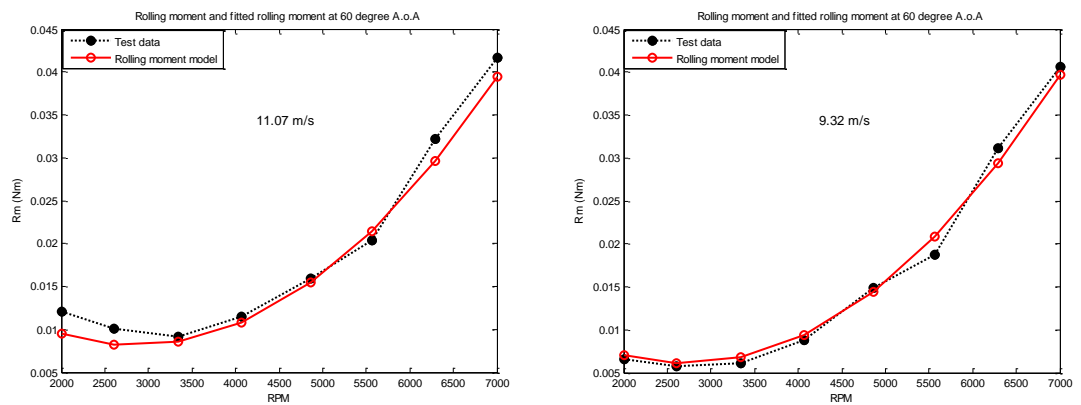


Figure 4.62: Test data and fitted rolling moment model at 45 degree A.o.A. w.r.t. the angular velocity of the rotor for different wind speeds

Test data and fitted rolling moment w.r.t. angular velocity of the rotor at 60 degree A.o.A. at different wind tunnel speeds are as:



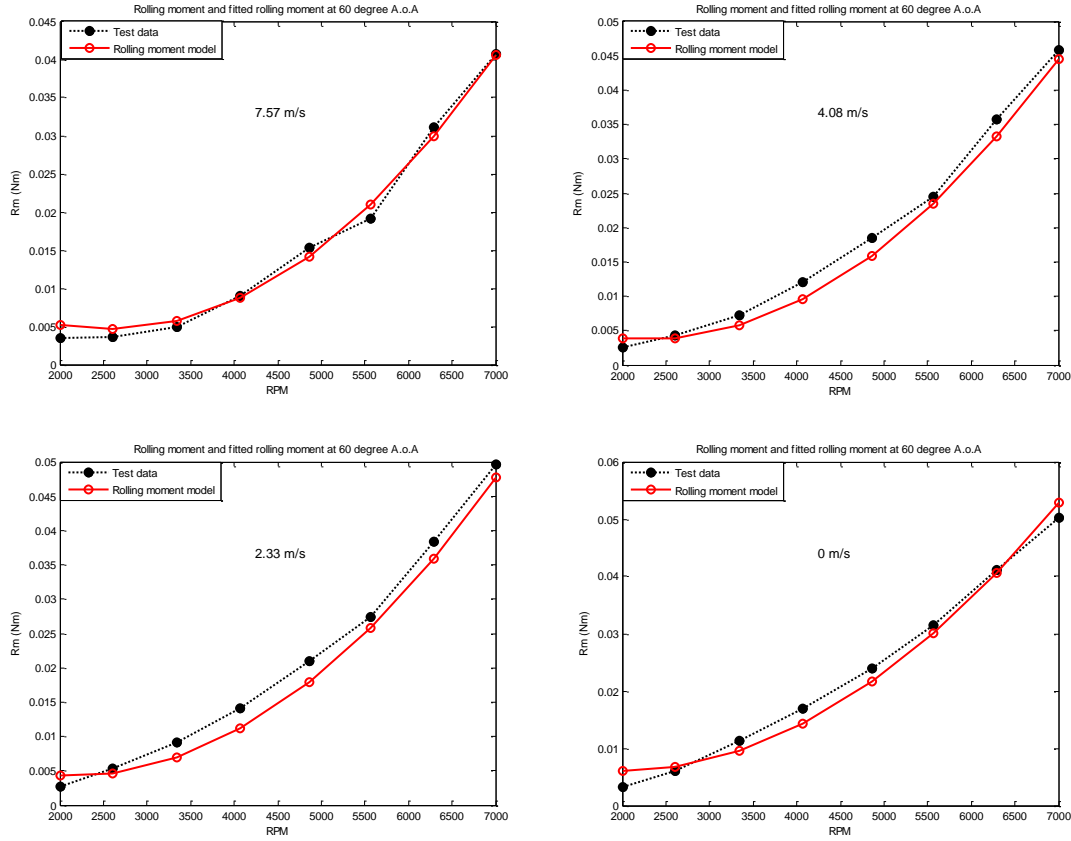


Figure 4.63: Test data and fitted rolling moment model at 45 degree A.o.A. w.r.t. the angular velocity of the rotor for different wind speeds

The reliability of the parameters using surface fitting algorithm is shown in Table 4.16:

Table 4.16: Goodness of fit in surface fitting

Thrust	Hub force	Rotor torque	Rolling moment
$R^2=0.9987$	$R^2=0.9630$	$R^2=0.9774$	$R^2=0.9768$
$R^2_{adj}=0.9986$	$R^2_{adj}=0.9620$	$R^2_{adj}=0.9768$	$R^2_{adj}=0.9761$

4.3. Rotor Interactions and Body Effect

Interactions of rotors are presented in Table 4.17, 4.18, and 4.19. Results show that when more than one rotor runs at the same time, the total thrust force obtained is less

than the total of the thrust forces of the individual rotors running separately. The reduction in the total thrust force is less than 5% when only two rotors run simultaneously. When all four rotors run at the same time interaction losses increase up to 8%.

Table 4.17: Thrust produced by each rotor of the quadrotor running separately

Angular velocity of the rotor (<i>RPM</i>)	Thrust produced by front rotor (N)	Thrust produced by right rotor (N)	Thrust produced by rear rotor (N)	Thrust produced by left rotor (N)	Total thrust produced by each rotor
2000	0.2570	0.2223	0.2490	0.2808	1.0091
2600	0.4844	0.4770	0.4746	0.5137	1.9497
3340	0.7907	0.7913	0.7902	0.8418	3.2140
4070	1.1744	1.2373	1.1646	1.2765	4.8528
4860	1.6370	1.7336	1.6383	1.6965	6.7054
5560	2.2236	2.2975	2.2452	2.2900	9.0563
6290	2.7276	3.0120	2.8253	2.9412	11.5061
7000	3.5916	3.7457	3.6017	3.7060	14.6450

Table 4.18: Thrust while two rotors are running

Angular velocity of the rotor (<i>RPM</i>)	Thrust produced by front and right rotor (N)	Thrust produced by right and rear rotor (N)	Thrust produced by rear and left rotor (N)	Thrust produced by front and left rotor (N)	Thrust produced by left and right rotor (N)	Thrust produced by front and rear rotor (N)
2000	0.4973	0.4783	0.5204	0.5550	0.4848	0.4929
2600	0.9566	0.9312	0.9844	1.0186	0.9905	0.9372
3340	1.5342	1.5558	1.6336	1.6504	1.5990	1.5164
4070	2.3533	2.3908	2.3690	2.4779	2.4018	2.3213
4860	3.2363	3.2392	3.3080	3.4367	3.3031	3.1960

5560	4.3992	4.3034	4.4492	4.6092	4.4536	4.3510
6290	5.6691	5.5434	5.6720	5.8676	5.6703	5.5723
7000	7.1680	6.9901	7.0394	7.3969	7.1094	6.9445

Table 4.19: Thrust while all rotors are running

Angular velocity of the rotor (<i>RPM</i>)	Thrust produced by front, right, rear, and left rotors (N)
2000	0.9305
2600	1.8204
3340	3.0267
4070	4.6207
4860	6.2946
5560	8.5599
6290	10.9914
7000	13.6335

Rotor interaction in hovering flight for thrust force is presented in Figure 4.64:

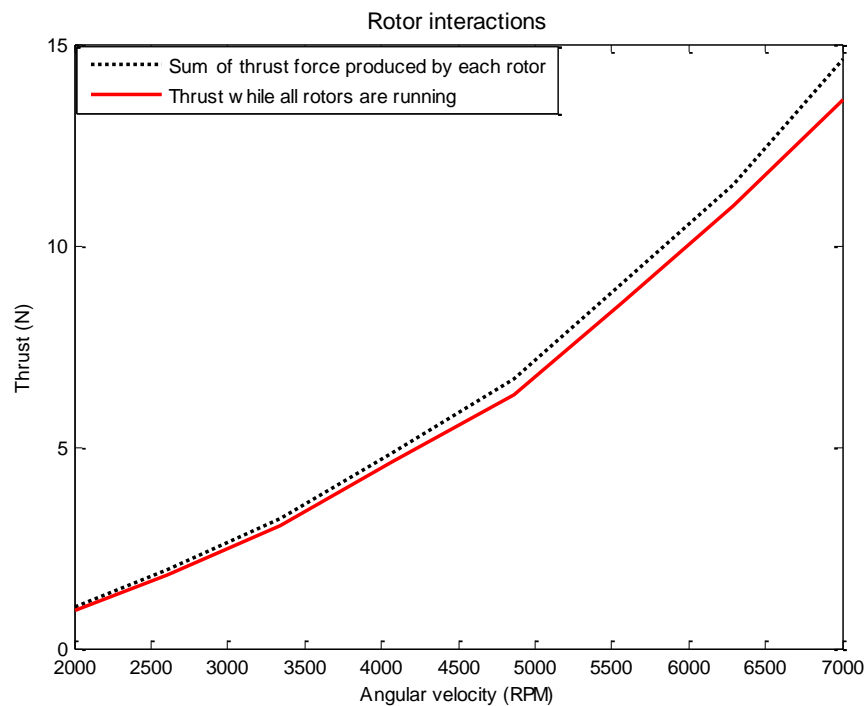


Figure 4.64: Rotor interactions for thrust force

In order to find the transfer function of the BLDC motor of the quadrotor, step input command is given to the motor and response is measured by using load cell. It is a second order transfer function which is found experimentally:

$$G_s = \frac{3.5}{0.0044s^2 + 0.08s + 1}$$

Step response of the BLDC motor is shown in Figure 4.65:

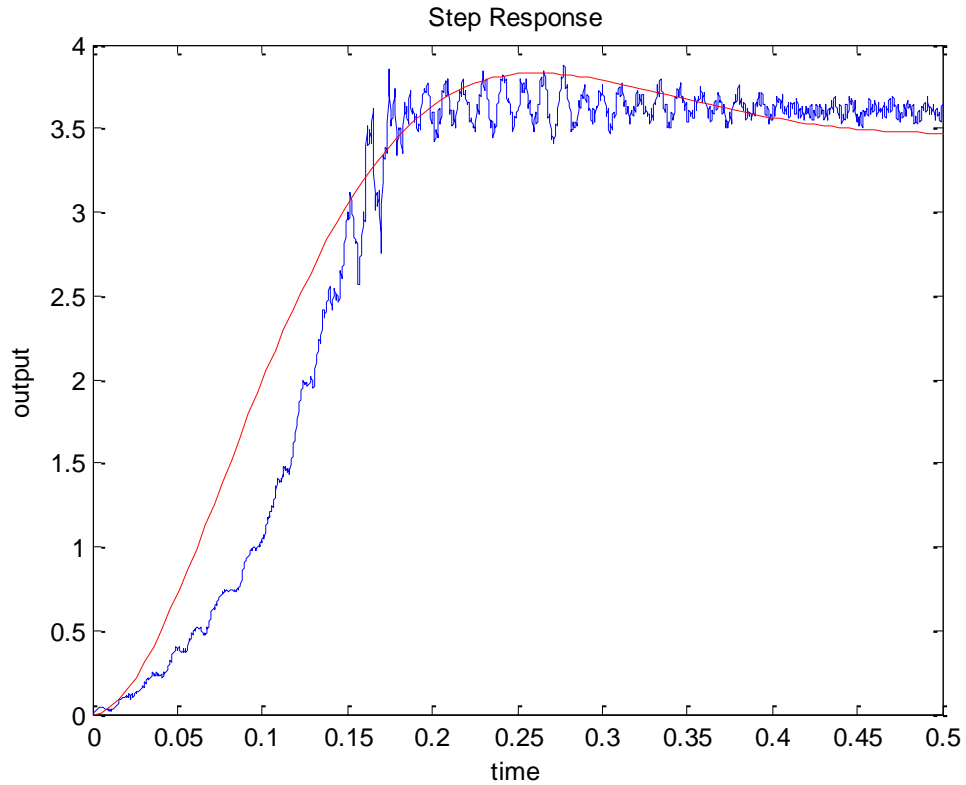


Figure 4.65: Step Response of BLDC Motor

Body effects of the quadrotor in the x and z directions are given in the following figure. Nondimensional body force coefficients are independent of the free stream velocity as expected.

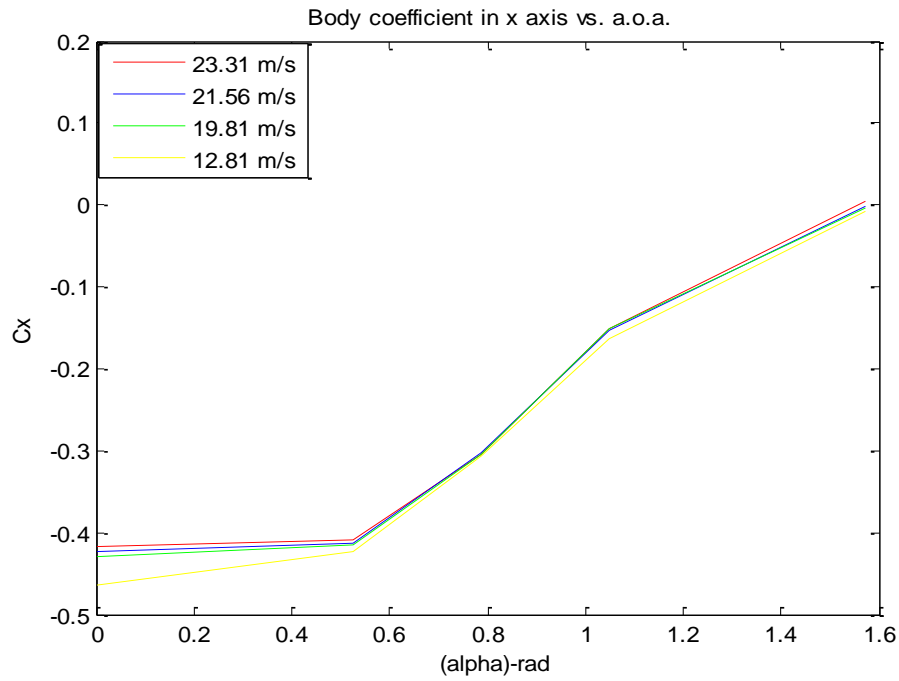


Figure 4.66: Body coefficient in x axis vs. A.o.A.

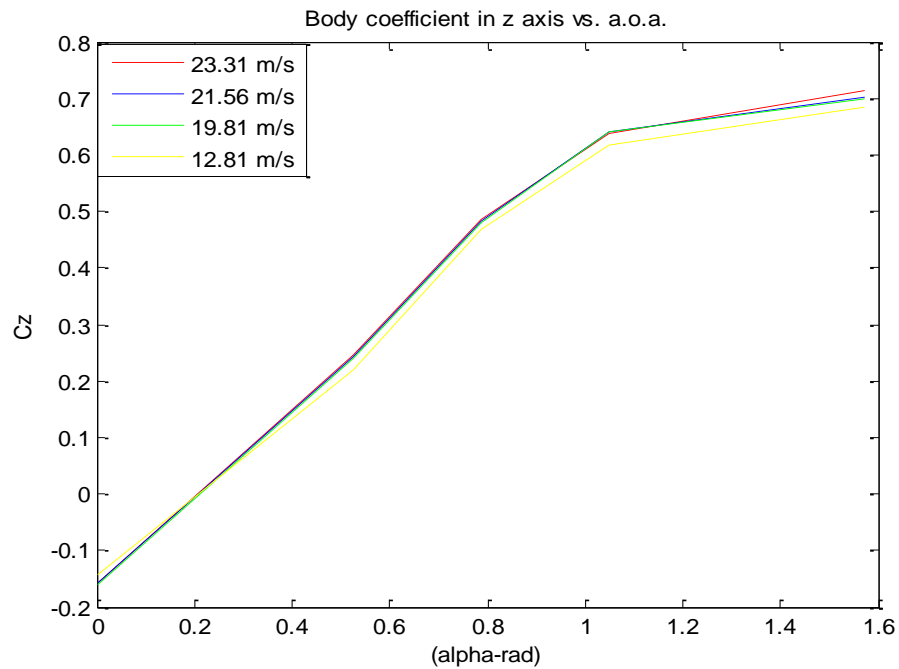


Figure 4.67: Body coefficient in z axis vs. A.o.A.

CHAPTER 5

CONCLUSION

5.1. Conclusion

In this study, aerodynamic forces and moments created by a fixed pitch rotor is studied. Firstly, a theoretical approach was conducted by using blade element theory and momentum theory. In this theoretical approach, thrust force, hub force, side force, rotor torque, rolling moment, and pitching moment were derived by using blade element theory, and by using momentum theory, induced velocity was found for hover, vertical flight, and forward flight. Secondly, an experimental identification study was carried out to estimate the parameters of the equations. The quadrotor UAV was placed in a wind tunnel and tested at various rotor speeds, flight speeds, and angles of attack. Free stream velocity, angular velocity of the rotor, forces and moments in three axes were measured by using a velocity sensor, an optical *RPM* sensor, and a six axes load cell. Parameters of the theoretical model were estimated by using the least squares method. *R* squared and adjusted *R* squared are used to evaluate the goodness of fit.

The evaluation of the results revealed that the blade element theory cannot capture certain trends between rotor loads and free stream velocity (vehicle speed). In order to utilize experimental results in simulations, empirical models have been developed. In these models, each rotor load is a second order polynomial function of rotor speed and free stream velocity. Several surface plots of measured rotor forces and moments have been prepared as functions of rotor and vehicle speeds for various angles of attack. Coefficients of the polynomial model are determined by using MATLAB surface fit function for every surface corresponding to different angles of attack. The model coefficients are then tabulated as functions of angle of attack. The empirical model fits experimental data better than the analytical model. Another benefit of the empirical model is that it eliminates the need for the induced velocity that the blade element theory requires. This allows the empirical model to be directly

used in simulations to estimate rotor loads for given rotor speed, vehicle speed, and angle of attack values. It does not require an iterative solution, unlike the analytical model, which requires an iterative approach to estimate induced velocity.

5.2. Discussion

Accuracy of the coefficients is very good for thrust and rotor torque, which are the two major loads on a rotor. However, it is not very good for rolling moment and hub force. This is because; rolling moment and hub force have very small values compared to thrust and rotor torque. They were affected by oscillations of *RPM* and mechanical problems. In vast majority of quadrotor related research rotors are assumed to produce thrust force only. While this assumption is acceptable in most cases as the thrust force is much larger than the off-axis forces and moments. For a very high fidelity simulation, modeling of secondary off-axis loads become important. The objective of this work is to develop a model that includes these effects for a more accurate simulation. Blade element and momentum theory based rotor aerodynamic model are used to predict these loads. Parameters of the model are identified through wind tunnel tests. The accuracy of the parameters are checked by R^2 and adjusted R^2 . At lower wind tunnel speeds, air flow around the quadrotor is cleaner and hence the forces and moments are closer to being steady. As a result, data collected from the load cell is more reliable. At higher wind tunnel speeds (between 12 and 23 *m/s*), flow gets more turbulent, and forces and moments fluctuate rapidly. Consequently, load cell measurements at higher tunnel speeds are corrupted by these fluctuations. Hence, the experiments are conducted between 0 and 11.0 *m/s* to get more reliable results. In addition electronic speed control unit used to regulate the angular speed of the rotors cannot keep the angular speed steady, which further degrades the quality of the measurements. Measurement errors are more pronounced on hub force and rolling moment measurements since they have lower magnitudes compared to thrust force and rotor torque, and hence have lower signal-to-noise ratios.

While the blade element theory can model rotor loads accurately in hover, it fails to capture high order effects observed in experiments when the rotor is placed in free

stream flow. More detailed theoretical models can be studied to model these effects. In this work, the model using BET and an empirical model are used to capture experimentally observed characteristics. The empirical model using MATLAB surface fitting algorithm is found satisfactory.

5.3. Future Works

To further enhance the rotor model developed here, following topics can be studied:

- Increase the quality of the measurements by reducing both electrical and aerodynamic noise in the environment, and improve electrical and mechanical components used in the test setup,
- Integrate the rotor model into simulation of the vehicle,
- Verify the simulation model with flight tests,
- Use more reliable estimation algorithms to estimate the parameters,
- Investigate more detailed rotor aerodynamic models to better match experimentally observed characteristics.

CHAPTER 6

APPENDIX

A. Properties of the Quadrotor and rotor used in the Study

Table 6.1: Constants of the quadrotor [18]

Name	Symbol	Value	Unit
Horizontal distance between the rotor axis and C.o.G	l	0.17	m
Vertical distance between the rotor axis and C.o.G.	h	0.04	m
Mass of the quadrotor	m	0.48	kg
Radius of the rotor	R	0.10	m
Inertia moment x axis	I_{xx}	5.6×10^{-3}	$kg \times m^2$
Inertia moment in y axis	I_{yy}	5.6×10^{-3}	$kg \times m^2$
Thrust per motor	T	0.5 – 3.7	N
Area of the quadrotor's body	S	0.0199	m^2

Table A.6.2: Properties of the quadrotor used in the study [18]

Manufacturer	Ascending Technologies GmbH
Model	Asc Tec Hummingbird
Motor type	Asc Tec X-BL 52s
Motor controller	AscTec X-BLDC
Flight control and IMU board	AscTec AutoPilot
Battery	2100 mAh Tp Battery

Table A.6.3: Properties of the rotor used in the experiments

θ_{tw}	0.0785 rad
θ_0	0.4712 rad
σ	0.11
a	π
\bar{c}	0.21 cm
\bar{C}_d	0.3

REFERENCES

- [1] Bouabdallah, S. and R. Siegwart. "Full Control of a Quadrotor." *International Conference on Intelligent Robots and Systems, Proc. of The IEEE International Conference on Intelligent Robots (IROS)*. (2007). 153-158.
- [2] Bouabdallah, S. "Design and control of quadrotors with application to autonomous flying." *PhD Thesis, Graduate School, EPFL, Lausanne*, (2007).
- [3] Fay, G. "Derivation of the Aerodynamic Forces for the Mesicopter Simulation." 2001.
- [4] Powers, C., et al. "Influence of Aerodynamics and Proximity Effects in Quadrotor Flight ." *Int. Symposium on Experimental Robotics*. 2012 .
- [5] Hoffmann, G. M., et al. "Quadrotor Helicopter Flight Dynamics and Control: Theory and Experiment." *American Institute of Aeronautics and Astronautics Guidance, Navigation and Control Conference and Exhibit, AIAA 2007-6461*. 2007.
- [6] Huang, H., et al. "Aerodynamics and Control of Autonomous Quadrotor Helicopters in Aggressive Maneuvering." *IEEE International Conference on Robotics and Automation, ICRA '09. IEEE International Conference*. (2009). 3277 –3282.
- [7] Belatti, T., C. Powers and V. Kumar. *Quadrotor Flight in Constrained Environments*. Villanova University.
- [8] Orsag, M. and S. Bogdan. "Influence of Forward and Descent Flight on Quadrotor Dynamics." Agarwal, R. K. *Recent Advances in Aircraft Technology*. Zagreb, Croatia: InTech, 2012. 141-156.
- [9] Mellinger, D., N. Michael and V. Kumar. "Trajectory Generation and Control for Precise Aggressive Maneuvers with Quadrotors." *International Journal of Robotics Research* 31.5 (2012): 664-674.
- [10] Kushleyev, A., et al. "Towards a swarm of agile micro quadrotors." *Autonomous Robots* 35.4, 287-300, 2013.
- [11] Naidoo, Y., Stopforth, R., and Bright, G. *Rotor Aerodynamic Analysis of a Qudrotor for Thrust Critical Applications*. 4th Robotics and Mechatronics

- Conference of South Africa (ROBMECH 2011), 23-25 November 2011, CSIR Pretoria South Africa.
- [12] Bristeau, P. – J., Martin, P., Salaün, E., Petit, N. *The Role of Propeller Aerodynamics in the Model of a Quadrotor UAV*. Proceedings of the European Control Conference 2009, Budapest, Hungary, August 23-26, 2009.
 - [13] *Helicopters built between 1907 and 1935*. n.d. 14 01 2014. <http://www.aviastar.org/helicopters_eng/breguet_gyro.php>.
 - [14] *Helicopters built between 1907 and 1935*. n.d. 14 01 2014. <http://www.aviastar.org/helicopters_eng/oemichen.php>.
 - [15] *Helicopters built between 1907 and 1935*. n.d. 14 01 2014. <http://www.aviastar.org/helicopters_eng/bothezat.php>.
 - [16] *Helicopters built between 1907 and 1935*. n.d. 14 01 2014. <http://www.aviastar.org/helicopters_eng/convertawings.php>.
 - [17] *Helicopters built between 1907 and 1935*. n.d. 14 01 2014. <http://www.aviastar.org/helicopters_eng/curtiss_vz-7.php>.
 - [18] Achtelik, M. "Nonlinear and Adaptive Control of a Quadcopter" *PhD Thesis*, TUM (2010).
 - [19] Seddon, J. M. *Basic Helicopter Aerodynamics*. Kent, Great Britain: BSP Professional Books, 1990.
 - [20] Johnson, W. *Helicopter Theory*. Princeton, NJ: Princeton University Press, 1980.
 - [21] Massachusetts Institute of Technology. *Aerospace Controls Laboratory*. n.d. 22 8 2014 <http://acl.mit.edu/projects/vpitch_quad.html>.
 - [22] Montgomery, D.C., Runger G.C. *Applied Statistics and Probability for Engineers*. Arizona State University, 5th Ed.:401-420 W. *Helicopter Theory*. Princeton, NJ: Princeton University Press, 1980.
 - [23] Pounds, P., Mahony, R., Corke, P., *Modelling and Control of a Quad-Rotor Robot*. Australian National University, Canberra, Australia, CSIRO ICT Centre, Brisbane, Australia.

- [24] Kaya, D., Kutay, T., “Aerodynamic Modeling and Parameter Estimation of a Quadrotor Helicopter.” *American Institute of Aeronautics and Astronautics, Atmospheric Flight Mechanics*, Atlanta , 2558 (2014).
- [25] Mangler K., W., Squire H., B., “The Induced Velocity Field of a Rotor”, *Aeronautical Research Council Reports and Memoranda*, London, 1953.
- [26] Stepniewski W., Z., “Rotary Wing Aerodynamics”, Ames Research Center, NASA Contractor Report, 1979.
- [27] Mathworks. *Chapter 5 Least Squares*. n.d. 15 1 2014.
<<http://www.mathworks.com/moler/least-squares.pdf>>.
- [28] Mathworks. *Documentation Center Least Square Fitting* . n.d. 15 1 2014
<<http://www.mathworks.com/help/curvefit/least-squares-fitting.html>>.
- [29] Penn Engineering GRASP Laboratory. 2009. 20 8 14 "Aggressive Maneuvers For Autonomous Quadrotor Flight". <
https://www.grasp.upenn.edu/success_story/aggressive_maneuvers_autonomous_quadrotor_flight>.
- [30] ETHZ Institute for Dynamic Systems and Control. n. d. 25 8 2014
<http://www.idsc.ethz.ch/Research_DAndrea/Flying_Machine_Arena>.